Reconstruction of charged particles in the LHCb experiment

Edwin Bos

Front cover: The sculpture "La Porte de l'Enfer" by Auguste Rodin.
Back cover: The author being glad to have made it down in one piece.

This work is part of the research programme of the 'Stichting voor Fundamenteel Onderzoek der Materie (FOM)', which is financially supported by the 'Nederlandse Organisatie voor Wetenschappelijk Onderzoek (NWO)'.

VRIJE UNIVERSITEIT

Reconstruction of charged particles in the LHCb experiment

ACADEMISCH PROEFSCHRIFT

ter verkrijging van de graad Doctor aan
de Vrije Universiteit Amsterdam,
op gezag van de rector magnificus
prof.dr. L.M. Bouter,
in het openbaar te verdedigen
ten overstaan van de promotiecommissie
van de faculteit der Exacte Wetenschappen
op woensdag 10 februari 2010 om 15.45 uur
in de aula van de universiteit,
De Boelelaan 1105

door

Edwin Bos

geboren te Haarlem

promotor:	prof.dr. M.H.M. Merk
copromotor:	dr. H.G. Raven

Contents

Chapter 1

Introduction

History shows that people are interested in the workings of the world around them. Ancient Greek philosophers are known to have contemplated on the nature of matter which we are made of. Anaxagoras for instance speculated that matter changes by the re-ordering of indivisible particles, which Democritus named atoms. Gathering and formulating proof for such hypotheses was formalised by Aristotle. This was extended by Roger Bacon to the scientific method of empirically observing nature to scrutinise hypotheses. It was not until 1897 that the field of elementary particle physics was born. Joseph J. Thompson discovered the first elementary particle in that year; the electron. Ernest Rutherford inferred the existence of the atomic nucleus from the results of scattering experiments. For the lightest atom, he named the nucleus 'proton'. Protons are found to only form a part of nuclei, as they are combined with neutrons, which were later discovered by Chadwick.

The electron, proton and neutron all form matter. Antimatter was discovered by Anderson in the form of the positron. Matter is what the observed universe from stars to interstellar dust is found to be made of. This matter is expected to have been created in equal amounts to antimatter during the Big Bang. So why don't we see antimatter in the world around us? Annihilation reduces the amount of matter and antimatter equally and therefore cannot explain the absence of antimatter. An imbalance in the presence of matter and antimatter can be created when the famous Sakharov conditions are met. One of these is the violation of *CP* symmetry. The *C* and *P* operations together change particles and antiparticles into each-other and reverse all spatial coordinate signs. If nature is not invariant under the *CP* operation, then particles behave differently from antiparticles, leading to the matter-antimatter imbalance. The study of *CP* violation is part of the motivation for conducting the LHCb experiment.

Elementary particle physics has grown to an understanding of elementary matter on the level of quarks and leptons. The mechanisms behind their strong and electroweak interactions are formulated in a theory known as the Standard Model. The electromagnetic and weak interactions were combined by Glashow, Weinberg and Salam, for which they received the Nobel prize in 1979. Chapter 2 introduces the Standard Model, the known elementary particles and gives a description of how *CP* violation is implemented in this theory.

Study of *CP* violation began in 1964, when it was observed in the decay of neutral kaons. This was expanded on by observing *B* hadrons as created in particle accelerators like PEP-II at SLAC and Tevatron at Fermilab. In order to improve on those observations, the LHC machine will offer higher centre-of-mass energy and luminosity. The LHC is build at CERN, offering collisions at a centre-of-mass energy $\sqrt{14}$ TeV to four main experiments. One of these is LHCb, which is described in chapter 3. The unprecedented amount of produced *B* hadrons will be used by LHCb to study *CP* violation as well as rare decays in the *B* meson system.

Designing a detector like LHCb offers experimental challenges, for which suitable solutions must be found. The design process benefits from existing knowledge of particle interactions and the performance of detector hardware. This understanding is used to predict the properties of the collisions and the response of the detector to the ensuing particles and radiation. Monte-Carlo software, as introduced in chapter 4, offers the possibility to simulate a working experiment and quantify the impact of design choices on the performance of the detector.

The simulated detector response is used in the development of software strategies, which aim at reconstructing the particles that traverse the detector from measured data. A particle can move through the entire detector or only part of it and be detected by all traversed sensitive layers or move undetected through for instance a structural support section of a layer. These aspects are taken into account when identifying hits in sensitive layers as being due to a single particle. The identification process is split into several pattern recognition strategies, which are described in chapter 5.

Given the hits that the pattern recognition ascribes to an individual particle, the path of that particle through the detector is determined by fitting a track model to those hits. The fitting process takes the impact of the traversed material and the magnetic field into account and results in a track. This reconstructed track offers the optimal estimate of the position and momentum of a particle, as well as their covariances, throughout the detector. In chapter 6 the fitting process and its tuning are detailed. The performance of the track fit is evaluated in chapter 7.

The reconstructed tracks are used in a multitude of physics analyses. There, a track is combined with the energy and type of the corresponding particle, as provided by the calorimeter system, particle identification detectors, and muon chambers. From this information the event can be reconstructed. In the final chapter, the impact of the track parameter resolution on the reconstructed invariant mass, and on the proper time is illustrated. This shows the importance of high quality track reconstruction.

Chapter 2

Theory

The established particle physics theory is summarised in the Standard Model of elementary particles and interactions. An introduction to the Standard Model is given in section 2.1. The description of *CP* violation is included in the Standard Model, where it appears in weak charged-current interactions, and is discussed in section 2.2. The mixing and decay of *B* mesons and all three types of *CP* violation are detailed in section 2.3. More comprehensive descriptions of the Standard Model, *CP* violation and the decay modes of interest to LHCb can be found in the literature [1, 2].

2.1 The Standard Model

The field of particle physics is defined by the study of elementary particles and their interactions. Experimental and theoretical efforts to study these subjects have culminated in a theory known as the Standard Model. It describes elementary particles interacting through the electromagnetic, weak and strong forces. The descriptions and predictions of the Standard Model are compatible with experimental results. One open issue is the predicted existence of the Higgs boson(s) [3], which is expected to be verified at the LHC. A shortcoming of the Standard Model is formed by the fact that the values of 18 of its parameters must be determined by experiments, rather than by fundamental considerations. Finally, the Standard Model describes three out of the four fundamental forces of nature. The exclusion of gravity from this theory prevents it to be a complete theory of (astro-)particle physics.

Elementary particles are sorted into fermions and bosons. They are distinguished from each other by the value of their spin. Fermions have a half-integer spin and bosons have an integer spin. Fermions interact through the electromagnetic and weak forces, as detailed in the Glashow-Salam-Weinberg (GSW) model, and through the strong force as described by Quantum Chromodynamics (QCD). In both models, the origin of interactions is related to symmetries of the physics under gauge transformations. These invariances predict the existence of mediating force carriers, which are exchanged between fermions. The fundamental forces, their relative strengths and mediating gauge bosons are listed in table 2.1.

Table 2.1: *The fundamental forces of the Standard Model, their relative strengths and mediating gauge bosons [4].*

force	relative strength	gauge bosons
strong	$\mathcal{O}(1)$	8 gluons (g_i)
electromagnetic	$\mathcal{O}(10^{-2})$	photon (γ)
weak	$\mathcal{O}(10^{-6})$	weak bosons ($W^{\pm}$, Z^0)

The elementary fermions are separated into quarks and leptons, which have some of their properties stated in table 2.2. They exist in particle and antiparticle variants, which have identical masses and lifetimes, while all internal quantum numbers are of the opposite sign. A splitting into three generations of fermions is made. Each generation consists of two quarks and two leptons, whose masses increase from the first to the third generation. The six quarks interact through all fundamental forces, having mass, electric charge, weak isospin and colour charge. Left-handed quarks and leptons are separated into up-type and down-type by the third component of their weak isospin (T_z). The up, charm and top quarks and neutral leptons have T_z one-half and the down, strange and bottom quarks and charged leptons have T_z minus one-half. Right-handed quarks and leptons have zero weak isospin and do not interact weakly. Leptons partake in all but strong interactions, as they have no colour charge. The electron, muon and tau leptons have integer electric charges and are paired with neutral leptons called neutrinos.

Table 2.2: *Properties of the elementary fermions of the Standard Model [4]. The (anti-)quarks exist in three (anti-)colours and antiparticles have the opposite electric charge.*

type	generation	name	elec. charge	mass
lepton	1	electron(e)	-1	0.511 MeV
		electron neutrino(ν_e)	0	< 3 eV
	2	muon(μ)	-1	106 MeV
		muon neutrino(ν_μ)	0	< 0.19 MeV
	3	tau(τ)	-1	1.78 GeV
		tau neutrino(ν_τ)	0	< 18.2 MeV
quark	1	up(u)	2/3	1.5-4 MeV
		down(d)	-1/3	4-8 MeV
	2	charm(c)	2/3	1.15-1.35 GeV
		strange(s)	-1/3	80-130 MeV
	3	top(t)	2/3	174.3 GeV
		bottom(b)	-1/3	4.1-4.4 GeV

Another difference between quarks and leptons became apparent by the observation that quarks do not exist as free particles in nature. All quarks but the top are combined into composite particles called hadrons. The top quark decays before hadronisation can take place. The restriction to hadrons is known as confinement, and is due to the strong force between quarks. This strong interaction is described by QCD, which is based on the $SU(3)_C$ gauge symmetry group. It dictates the existence of eight gauge bosons, known as gluons. These gluons are massless vector bosons, which couple to colour charge, and themselves also have colour charges. Hadrons are colour-neutral pairs (mesons) or triplets (hadrons) of red, green, and blue quarks and anti-red, anti-green, and anti-blue antiquarks, bound together by gluon exchanges. At distances smaller than the size of a hadron, the strength of the strong force decreases towards zero with the distance between the component quarks. This phenomenon of asymptotic freedom enables the quarks in high-energy collisions to be considered as free particles, simplifying their theoretical treatment.

In the Standard Model, the electromagnetic and weak forces are treated as a single electroweak interaction, which is described by the GSW model. This theory is based on the $SU(2)_L \times U(1)_Y$ symmetry group. Given the fact that the W and Z bosons have masses, this is not an exact symmetry. Their non-zero masses imply breaking of the gauge invariance of the electroweak theory, leading to non-renormalisability, if it was not for the Higgs mechanism [3, 5]. In that scheme, the theory itself is gauge invariant, but the ground state does not exhibit the symmetry, a feature known as spontaneous symmetry breaking. Spontaneous symmetry breaking allows fermions to acquire mass from the Yukawa coupling to the Higgs field. Quark mass eigenstates are not weak eigenstates, those are given by superpositions of the quark mass eigenstates. These superpositions are described by the Cabibbo-Kobayashi-Maskawa [6, 7] (CKM) quark mixing matrix.

The electromagnetic force is mediated by a massless gauge boson called the photon. It is exchanged by particles with an electric charge. The weak force has two charged gauge bosons ($W^{\pm}$) with a mass of 80.40±0.03 GeV [4] and one neutral gauge boson (Z^0) of 91.188±0.002 GeV [4]. In a weak interaction, the $W^{\pm}$ and Z^0 bosons are virtual particles, which limits the effective range of the weak force to around 10^{-20} m. The photon on the other hand is massless, offering infinite range to the electromagnetic force. Comparing the two forces within the effective range of the weak force reveals that their strengths are of the same order of magnitude.

2.2 *CP* violation in the Standard Model

Neither charge conjugation C, nor parity P nor their combined operation CP are conserved symmetries in weak decays. Particles are not eigenstates of C, unless they are their own antiparticle. Parity violation was first observed in the β decay of ^{60}Co in 1957 [8]. The violation of CP symmetry was discovered through the study of $K_L \to \pi\pi$ decays in 1964 [9]. CP violation has also been observed in decays of neutral B_d mesons in 2001 [10, 11]. The origin of CP violation in the Standard Model is embedded in the flavour structure of weak charged-current interactions. These interactions convert up-type quarks into a superposition of down-type quarks, through the emission or absorption of a $W^{\pm}$, and similarly down-type quarks into a superposition of up-type quarks. Quark mixing is not achieved through the Z^0 boson, the absence of such flavour changing neutral currents at tree level is explained by the Glashow-Iliopoulos-Maiani (GIM) mechanism [12].

The charged-current weak interaction Lagrangian describing quark mixing is formulated in terms of the left-handed components of the quark mass eigenstates as:

$$\mathcal{L}_{CC} = -\frac{g}{\sqrt{2}} \begin{pmatrix} \bar{u} & \bar{c} & \bar{t} \end{pmatrix}_L \gamma^\mu V_{CKM} \begin{pmatrix} d \\ s \\ b \end{pmatrix}_L W_\mu + h.c.. \tag{2.1}$$

In this equation, the interaction strength is given by the gauge coupling g of $\mathrm{SU(2)_L}$, γ^μ are the Dirac matrices, V_{CKM} is the CKM quark mixing matrix and the charged $W^\pm$ bosons are described by the fields W_μ. The electroweak eigenstates of the down-type quarks can be obtained from their mass eigenstates through multiplication with the CKM matrix:

$$\begin{pmatrix} d' \\ s' \\ b' \end{pmatrix} = \begin{pmatrix} V_{ud} & V_{us} & V_{ub} \\ V_{cd} & V_{cs} & V_{cb} \\ V_{td} & V_{ts} & V_{tb} \end{pmatrix} \begin{pmatrix} d \\ s \\ b \end{pmatrix}. \tag{2.2}$$

This 3×3 complex, unitary matrix was in part introduced by Cabibbo [6] in 1963 and extended to include the third quark generation by Kobayashi and Maskawa [7] in 1973. The unitarity of the CKM matrix excludes elementary flavour-changing neutral currents, which forms the basis of the GIM mechanism. Each of the individual elements squared are proportional to the charged-current transition probability from one quark to another. Their values are not predicted by the Standard Model and therefore need to be determined experimentally by observing weak decays or mixing of the relevant quarks. The present Particle Data Group [4] world-averaged values for the CKM matrix elements are given in table 2.3.

Table 2.3: *World-averaged values of the absolute magnitudes of the CMK matrix elements [4].*

matrix element
$\|V_{ud}\| = 0.97418 \pm 0.00027$
$\|V_{us}\| = 0.2255 \pm 0.0019$
$\|V_{ub}\| = (3.93 \pm 0.36) \times 10^{-3}$
$\|V_{cd}\| = 0.230 \pm 0.011$
$\|V_{cs}\| = 1.04 \pm 0.06$
$\|V_{cb}\| = (41.2 \pm 1.1) \times 10^{-3}$
$\|V_{td}\| = (8.1 \pm 0.6) \times 10^{-3}$
$\|V_{ts}\| = (38.7 \pm 2.3) \times 10^{-3}$
$\|V_{tb}\| > 0.74$

In general, a $n \times n$ complex matrix consists of $2n^2$ independent parameters. Unitarity of a matrix results in n^2 constraints, leaving n^2 free parameters. As the CKM matrix deals with six quarks, six arbitrary phases can be absorbed by redefining the quark fields, keeping one overall phase. This leaves four parameters which need to be determined experimentally, being three rotation angles and one complex phase. This complex phase is the source of *CP* violation in the Standard Model weak interactions [7]. In case a pair of up-type or down-type quarks from two generations have equal mass, the complex phase can be eliminated through a unitary transformation of the quark fields [13].

The CKM matrix can also be written in the Wolfenstein expansion [14] of four free parameters. It is based on the observation that the diagonal elements are close to unity and the off-diagonal elements are progressively smaller. Transitions between the first and second generations are suppressed by CKM factors of first order, suppression increases by an order for transitions between the second and third generations and between the first and third generations the suppression is of $O(10^{-3})$. The matrix elements are expanded up to third order around the sine of the Cabibbo angle $\lambda = \sin\theta_C$ [15] as follows:

$$V_{\mathrm{CKM}} = \begin{pmatrix} 1-\frac{1}{2}\lambda^2 & \lambda & A\lambda^3(\rho - i\eta) \\ -\lambda & 1-\frac{1}{2}\lambda^2 & A\lambda^2 \\ A\lambda^3(1-\rho-i\eta) & -A\lambda^2 & 1 \end{pmatrix} + O(\lambda^4)\,. \tag{2.3}$$

In this expansion, the parameters A, ρ and η are real numbers. As the complex phase is the source of observed *CP* violation, the parameter η is expected to be non-zero. Terms up to $O(\lambda^5)$ in the Wolfenstein expansion are required for the study of physics channels in for instance the B_s sector. The additional terms are [14]:

$$\begin{pmatrix} -\frac{1}{8}\lambda^4 & 0 & 0 \\ A^2\lambda^5(\frac{1}{2}-\rho-i\eta) & -\frac{1}{8}\lambda^4(1+4A^2) & 0 \\ \frac{1}{2}A\lambda^5(\rho+i\eta) & A\lambda^4(\frac{1}{2}-\rho-i\eta) & -\frac{1}{2}A^2\lambda^4 \end{pmatrix} + O(\lambda^6)\,. \tag{2.4}$$

The unitarity of the CKM matrix provides nine constraining relations between the matrix elements. Three of these constraints can be formulated as $\Sigma_j|V_{ij}|^2 = 1$ for each generation i. This states that the sum of all couplings of an up-type quark to each of the down-type quarks is identical for each of the generations and is known as weak universality. The other six relations are orthogonality conditions and can be written as $\Sigma_k V_{ik}V^*_{jk} = 0$ $(i \neq j)$. Three relations define the orthogonality of the columns and the remaining three that of the rows of the CKM matrix. They are given as follows:

$$V_{ud}V^*_{us} + V_{cd}V^*_{cs} + V_{td}V^*_{ts} = 0\,, \tag{2.5}$$
$$V_{us}V^*_{ub} + V_{cs}V^*_{cb} + V_{ts}V^*_{tb} = 0\,, \tag{2.6}$$
$$V_{ud}V^*_{ub} + V_{cd}V^*_{cb} + V_{td}V^*_{tb} = 0\,, \tag{2.7}$$
$$V_{ud}V^*_{cd} + V_{us}V^*_{cs} + V_{ub}V^*_{cb} = 0\,, \tag{2.8}$$
$$V_{cd}V^*_{td} + V_{cs}V^*_{ts} + V_{cb}V^*_{tb} = 0\,, \tag{2.9}$$
$$V_{ud}V^*_{td} + V_{us}V^*_{ts} + V_{ub}V^*_{tb} = 0\,. \tag{2.10}$$

Each of these relations can be represented by a triangle in the complex plane [16]. All six triangles have different shapes, but equal surfaces. Their surface is equal to half the amount given by the Jarlskog parameter [17, 18]:

$$J_{CP} = A^2\lambda^6\eta = \left(2.92^{+0.15}_{-0.15}\right) \times 10^{-5}\,. \tag{2.11}$$

Dividing all terms of the orthogonality relation (2.7) by $V_{cd}V^*_{cb}$ results in the unitarity triangle, which is depicted in figure 2.1. Its apex in the complex plane is located at $(\eta(1-\frac{1}{2}\lambda^2)\,,\,\rho(1-\frac{1}{2}\lambda^2))$. For notational convenience, the Wolfenstein parameters have a generalised form, in which η and ρ are absorbed in $\bar{\eta}$ and $\bar{\rho}$:

$$\begin{aligned} \bar{\eta} &\equiv \eta(1-\frac{1}{2}\lambda^2)\,, \\ \bar{\rho} &\equiv \rho(1-\frac{1}{2}\lambda^2)\,. \end{aligned} \tag{2.12}$$

The world-averaged values of the generalised Wolfenstein parameters are given in table 2.4

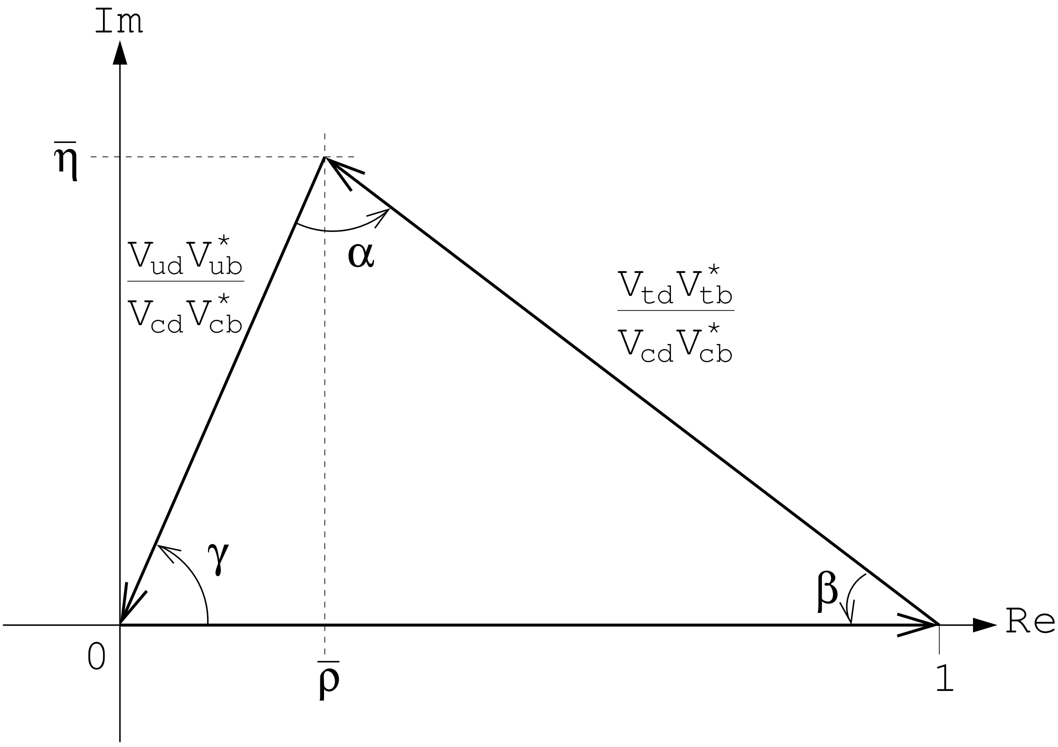

Figure 2.1: *The unitarity triangle, showing the angles α, β and γ.*

Table 2.4: *World-averaged values of the generalised Wolfenstein parameters [17].*

parameter	value ± 1σ [°]	parameter	value ± 1σ [°]
λ	$0.22521^{+0.00082}_{-0.00082}$	$\bar{\rho}$	$0.139^{+0.025}_{-0.027}$
A	$0.8116^{+0.0097}_{-0.0241}$	$\bar{\eta}$	$0.341^{+0.016}_{-0.015}$

The three internal angles α, β and γ are re-phasing invariant observables. They are specified in terms of CKM matrix elements as:

$$\begin{aligned} \alpha &= \arg\left(-\frac{V_{td}V_{tb}^*}{V_{ud}V_{ub}^*}\right), \\ \beta &= \arg\left(-\frac{V_{cd}V_{cb}^*}{V_{td}V_{tb}^*}\right), \\ \gamma &= \arg\left(-\frac{V_{ud}V_{ub}^*}{V_{cd}V_{cb}^*}\right), \end{aligned} \tag{2.13}$$

with world-averaged values [17] as stated in table 2.5.

Table 2.5: *World-averaged values of the unitarity triangle angles α, β and γ.*

observable	value $\pm$ 3σ [°]
α	$89.0^{+4.4}_{-4.2}$
β	$21.07^{+0.90}_{-0.88}$
γ	70^{+27}_{-30}

The Standard Model description of *CP* violation can be tested by determining the elements of the CKM matrix. Measuring the angles and lengths of the sides of all of the triangles over-constrains the CKM matrix. This offers the possibility to find hints of new physics if inconsistency is observed between the constraints. The existing measurements relating to the angles α, β and γ, predominantly made by the BaBar, Belle, CDF and D0 experiments, have been translated into contour constraints in the $\bar{\rho}$, $\bar{\eta}$ plane, as shown in figure 2.2. They include direct measurements of the *CP* phases α, β, and γ by the B-factory experiments, as for instance $\sin 2\beta$ in the $B_d^0 \to J/\psi K_s$ channel [19, 20]. The circle contours around (1,0) originate from the measured oscillation frequencies of the B_d (BaBar and Belle) and B_s (CDF and D0) mesons. Circle contours around (0,0) represent $|V_{\mathrm{ub}}|$, and the hyperbole comes from ϵ in the kaon system.

2.3 The *B* meson system

B mesons are composed of a $\bar{b}$ antiquark and a u, d, s or c quark, forming a B_u^+, B_d^0, B_s^0 or B_c^+. Together with the anti-B mesons, there are four neutral and four charged mesons making up the B meson system. According to the CPT theorem, each meson and corresponding anti-meson have the same mass and lifetime. The first discovered B meson is the B_d^0, which was observed by the CLEO [21] and CUSB [22] collaborations in 1981. In 1983, the MAC [23] and MARK-II [24] collaborations were the first to measure B meson lifetimes. The mean lifetime of B_d^0 and B_s^0 mesons is 1.5 ps, allowing for a fraction of their decay vertices to be observed separately from the primary interaction vertex.

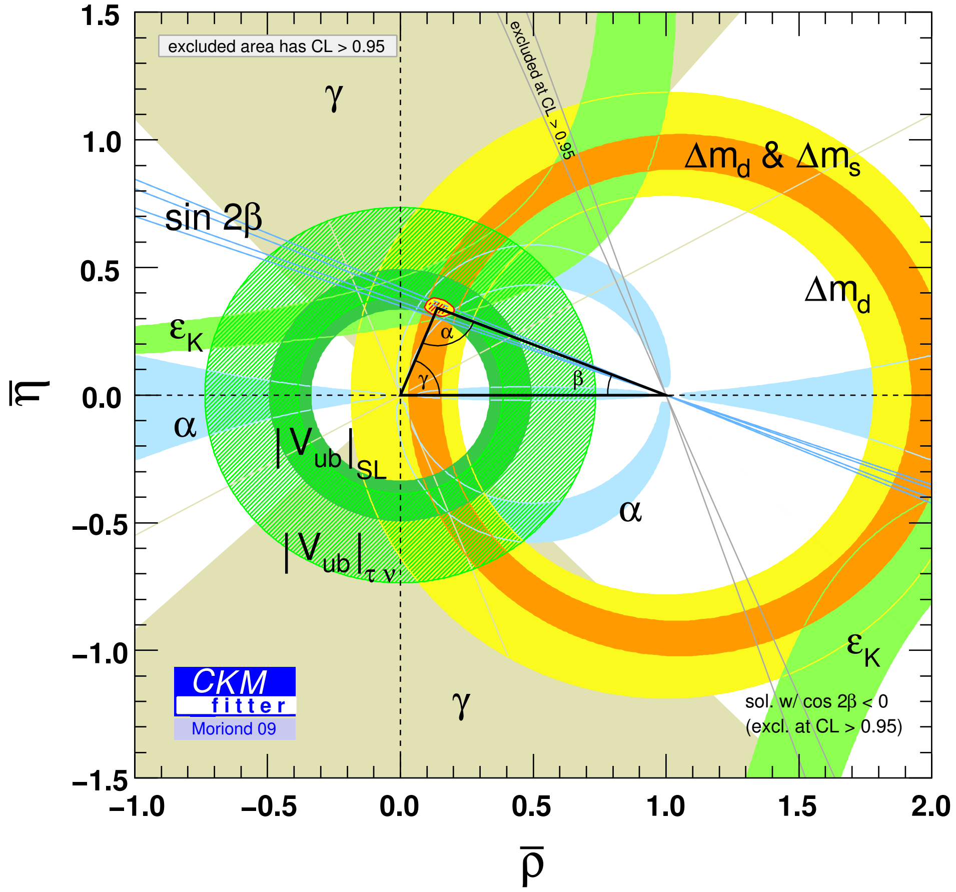

Figure 2.2: *Global CKM fit in the $(\bar{\eta}, \bar{\rho})$ plane by the CKM fitter group, showing the current status on constraining the unitarity triangle [17].*

2.3.1 Neutral B meson mixing

The four neutral B mesons are combinations of $b(\bar{b})$ and $d(\bar{d})$ or $s(\bar{s})$ type quarks and antiquarks and are generalized as B^0. Their quark content is specified as follows:

$$\begin{aligned} |B_d^0\rangle &= |\bar{b}d\rangle \quad , \quad |\overline{B}_d^0\rangle = |b\bar{d}\rangle \quad , \\ |B_s^0\rangle &= |\bar{b}s\rangle \quad , \quad |\overline{B}_s^0\rangle = |b\bar{s}\rangle \quad . \end{aligned} \tag{2.14}$$

It has been discovered in 1987 by the ARGUS collaboration [25] that a B^0 can oscillate into a $\overline{B}^0$ and back. This phenomenon is called mixing of neutral B mesons and was first observed for B_d^0 mesons. Mixing between meson and anti-meson occurs through the weak interaction.

The state of a neutral B meson at time t can be described by a superposition of the two flavour states B^0 and $\overline{B}^0$:

$$|B(t)\rangle = a(t)|B^0\rangle + b(t)|\overline{B}^0\rangle\,. \tag{2.15}$$

This state evolves in time as described by the time-dependent Schrödinger equation:

$$i\frac{d}{dt}\begin{pmatrix} a(t) \\ b(t) \end{pmatrix} = \begin{pmatrix} H_{11} & H_{12} \\ H_{21} & H_{22} \end{pmatrix}\begin{pmatrix} a(t) \\ b(t) \end{pmatrix}. \tag{2.16}$$

An effective, non-hermitian Hamiltonian is used to account for losses due to B meson decay. The Hamiltonian can be re-written as a linear combination of hermitian mass M and lifetime Γ matrices:

$$H = M - \frac{i}{2}\Gamma = \begin{pmatrix} M_{11} & M_{12} \\ M_{21} & M_{22} \end{pmatrix} - \frac{i}{2}\begin{pmatrix} \Gamma_{11} & \Gamma_{12} \\ \Gamma_{21} & \Gamma_{22} \end{pmatrix}. \tag{2.17}$$

CPT symmetry dictates that B^0 and $\overline{B}^0$ have equal masses, $M_{11} = M_{22}$, and equal lifetimes, $\Gamma_{11} = \Gamma_{22}$. As M and Γ are hermitian matrices, the off-diagonal matrix elements satisfy $M_{12} = M_{21}^*$ and $\Gamma_{12} = \Gamma_{21}^*$. Those terms represent flavour-changing transitions with virtual (M_{12}) or on-shell (Γ_{12}) intermediate states. The box diagrams containing a top quark as shown in figure 2.3 dominate the amplitude M_{12}. The associated CP-odd phases of the $B-\overline{B}$ mixing are called ϕ_d (B_d mesons) and ϕ_s (B_s mesons).

The eigenstates of the effective Hamiltonian are the mass eigenstates of the neutral B mesons. These mass eigenstates can be represented as linear combinations of the two flavour eigenstates B^0 and $\overline{B}^0$:

$$|B_{L,H}(t)\rangle = p|B^0\rangle \pm q|\overline{B}^0\rangle\,, \tag{2.18}$$

where L and H label the lighter and heavier mass eigenstates. The complex parameters p and q satisfy the normalisation condition $|p^2| + |q^2| = 1$. Their ratio can be obtained by solving the effective Schrödinger equation, which leads to:

$$\frac{q}{p} = -\sqrt{\frac{H_{21}}{H_{12}}}\,. \tag{2.19}$$

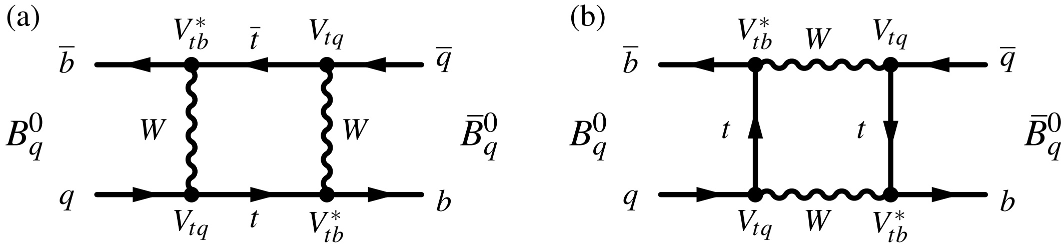

Figure 2.3: *Feynman box diagrams of contributions to M_{12}, illustrating the transformation from B^0 to $\overline{B}^0$, with the quark q being either a bottom or a strange quark and the top quark can alternatively be a u or c quark. The reverse process requires (anti)quarks to be replaced by their antiparticles and taking the complex-conjugates of the CKM matrix elements.*

The time dependence of the light and heavy mass eigenstates can be expressed as a function of the mass eigenstate at time of creation:

$$|B_{L,H}(t)\rangle = e^{-(iM_{L,H}+\Gamma_{L,H}/2)t}|B_{L,H}(0)\rangle\,. \tag{2.20}$$

In the exponent, $M_{L,H}$ and $\Gamma_{L,H}$ are the physical masses and lifetimes of the mass eigenstates. The differences in and averages of the mass and lifetime are defined as:

$$\begin{array}{lclcl} \Delta M = M_H - M_L & , & M = (M_H + M_L)/2 & , \\ \Delta\Gamma = \Gamma_H - \Gamma_L & , & \Gamma = (\Gamma_H + \Gamma_L)/2 & . \end{array} \tag{2.21}$$

It is the difference in mass which determines the frequency of the neutral B meson oscillations, as can be seen from formula (2.25). The phenomenon of oscillation in the neutral B meson system has mainly been studied for B_d^0 mesons. Oscillations between B_s^0 and $\overline{B}_s^0$ mesons have been observed more recently by the CDF [26] and D0 [27] collaborations. The mass differences which dictate the oscillation frequencies are determined to be $\Delta M_d = 0.507 \pm 0.005$ ps^{-1} [28] and $\Delta M_s = 17.77 \pm 0.10 \pm 0.07$ ps^{-1} [26]. A larger mass difference for the B_s^0 implies a more rapid oscillation than for the B_d. This is illustrated in figure 2.4, which shows the probability as a function of time for a B^0 to decay as a B^0 or $\overline{B}^0$, under the assumption that $|q/p| = 1$. Measurements of the decay width difference $\Delta\Gamma_s$ in the $B_s^0 \to J/\psi\phi$ channel have been made by D0 [29] and CDF [30], resulting in $0.17 \pm 0.09 \pm 0.02$ ps^{-1} and $0.076^{+0.059}_{-0.063} \pm 0.006$ ps^{-1}.

Hadrons are created in processes which involve the strong interaction. For neutral B mesons this implies that they are created as pure flavour eigenstates. Their time evolution can be expressed by combining equations (2.18) and (2.20):

$$\begin{aligned} |B^0(t)\rangle &= g_+(t)|B^0\rangle + \frac{q}{p}g_-(t)|\overline{B}^0\rangle\,, \\ |\overline{B}^0(t)\rangle &= g_+(t)|\overline{B}^0\rangle + \frac{p}{q}g_-(t)|B^0\rangle\,. \end{aligned} \tag{2.22}$$

Here the first term leaves the flavour state unchanged, whilst the second term lets it oscillate. The parameters $g_\pm$, representing the decay time dependency, are given

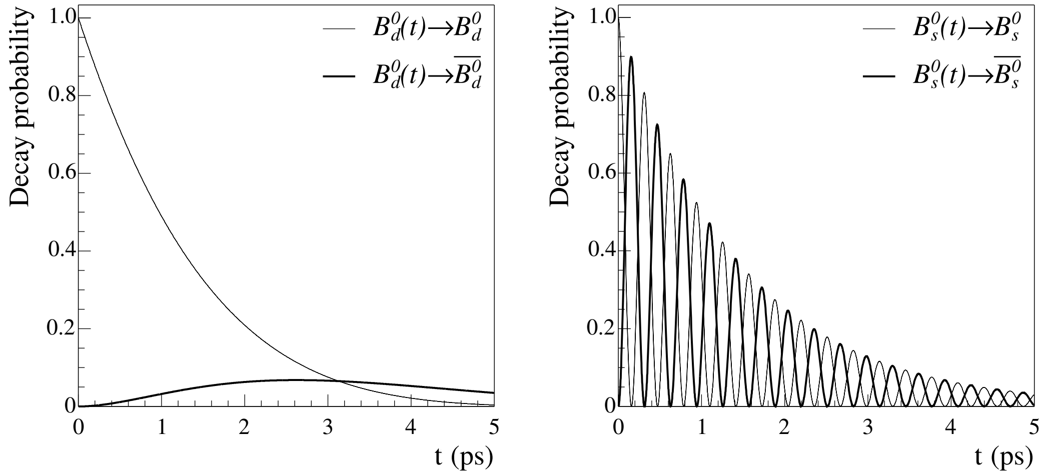

Figure 2.4: *Probability of a neutral B meson produced as a B^0 to decay as a B^0 or as a $\overline{B}^0$, shown for B_d^0 (left) and B_s^0 (right).*

by:

$$g_\pm(t) = (e^{-(iM_L+\Gamma_L/2)t} \pm e^{-(iM_H+\Gamma_H/2)t})/2\,. \tag{2.23}$$

From these evolution equations, the probabilities for observing a B^0 or $\overline{B}^0$ can be obtained:

$$\begin{aligned} |\langle B^0|B^0(t)\rangle|^2 &= |g_+(t)|^2 \quad , \quad |\langle B^0|\overline{B}^0(t)\rangle|^2 = \left|\tfrac{p}{q}\right|^2 |g_-(t)|^2 \quad , \\ |\langle \overline{B}^0|\overline{B}^0(t)\rangle|^2 &= |g_+(t)|^2 \quad , \quad |\langle \overline{B}^0|B^0(t)\rangle|^2 = \left|\tfrac{q}{p}\right|^2 |g_-(t)|^2 \quad , \end{aligned} \tag{2.24}$$

with

$$|g_\pm(t)|^2 = (e^{-\Gamma_L t} + e^{-\Gamma_H t} \pm 2e^{-\Gamma t}\cos\Delta M t)/4\,. \tag{2.25}$$

2.3.2 *B* meson decays

B mesons can decay through over 200 known modes, with branching fractions in the range $\mathcal{O}(10^{-3} - 10^{-12})$ [4]. Most of these decay modes are not common to B^0 and $\overline{B}^0$, which leads to $\Delta\Gamma$ being small compared to ΔM, as $\Delta\Gamma$ originates from real intermediate states to which both states can decay. The final states can contain leptons as well as hadrons and are classified as leptonic, semileptonic and hadronic.

The time-dependent decay amplitudes (A_f) of the flavour eigenstates to a final state f are specified using the effective Hamiltonian:

$$A_f = \langle f|H_{\text{eff}}|B^0\rangle \quad , \quad \bar{A}_f = \langle f|H_{\text{eff}}|\overline{B}^0\rangle \quad . \tag{2.26}$$

Both these and the decay amplitudes for the charge-conjugate final states can be written as sums of the contributing amplitudes, split into their magnitudes and pairs of phase terms:

$$A_f = \sum_k A_k e^{i\delta_k} e^{i\phi_k} \quad , \quad \bar{A}_{\bar{f}} = \sum_k A_k e^{i\delta_k} e^{-i\phi_k} \quad , \tag{2.27}$$

with A_k being the same real number for both B^0 and $\overline{B}^0$ initial states. A complex parameter from the Standard Model Lagrangian (2.1) will appear in complex conjugate form in the *CP* conjugate amplitude. As the phase ϕ appears with opposite sign in A_f and $\bar{A}_{\bar{f}}$, it therefore derives from such a complex parameter. In the Standard Model such a phase only occurs in the CKM matrix and hence ϕ is called the weak phase. The δ phase has the same sign in A_f and $\bar{A}_{\bar{f}}$ and can thus arise from a real Lagrangian parameter. It originates from the final state interactions which are dominated by strong interactions and is therefore named the strong phase.

Using these decay amplitudes, the decay rates can be expressed as follows:

$$\begin{aligned}
\Gamma_{B^0\to f}(t) &= |A_f|^2 \left(|g_+(t)|^2 + |\lambda_f|^2|g_-(t)|^2 + 2\Re[\lambda_f g_+^*(t)g_-(t)]\right) , \\
\Gamma_{B^0\to \bar{f}}(t) &= |\bar{A}_{\bar{f}}|^2 \left|\tfrac{q}{p}\right|^2 \left(|g_-(t)|^2 + |\bar{\lambda}_{\bar{f}}|^2|g_+(t)|^2 + 2\Re[\bar{\lambda}_{\bar{f}} g_+(t)g_-^*(t)]\right) , \\
\Gamma_{\overline{B}^0\to f}(t) &= |A_f|^2 \left|\tfrac{p}{q}\right|^2 \left(|g_-(t)|^2 + |\lambda_f|^2|g_+(t)|^2 + 2\Re[\lambda_f g_+(t)g_-^*(t)]\right) , \\
\Gamma_{\overline{B}^0\to \bar{f}}(t) &= |\bar{A}_{\bar{f}}|^2 \left(|g_+(t)|^2 + |\bar{\lambda}_{\bar{f}}|^2|g_-(t)|^2 + 2\Re[\bar{\lambda}_{\bar{f}} g_+^*(t)g_-(t)]\right) ,
\end{aligned} \tag{2.28}$$

with the λ parameters defined as:

$$\begin{aligned}
\lambda_f &\equiv q\bar{A}_f/pA_f \quad , \quad \bar{\lambda}_f \equiv 1/\lambda_f \quad , \\
\lambda_{\bar{f}} &\equiv q\bar{A}_{\bar{f}}/pA_{\bar{f}} \quad , \quad \bar{\lambda}_{\bar{f}} \equiv 1/\lambda_{\bar{f}} \quad .
\end{aligned} \tag{2.29}$$

Using the definition of $g_\pm(t)$ (2.23), the decay rates can be formulated as the master equations:

$$\begin{aligned}
\Gamma_{B^0\to f}(t) =&|A_f|^2(1+|\lambda_f|^2)\frac{e^{-\Gamma t}}{2}\cdot \\
&\left(\cosh\frac{\Delta\Gamma t}{2} + D_f \sinh\frac{\Delta\Gamma t}{2} + C_f\cos(\Delta M t) - S_f\sin(\Delta M t)\right) , \\
\Gamma_{\overline{B}^0\to f}(t) =&|A_f|^2 \left|\tfrac{p}{q}\right|^2 (1+|\lambda_f|^2)\frac{e^{-\Gamma t}}{2}\cdot \\
&\left(\cosh\frac{\Delta\Gamma t}{2} + D_f \sinh\frac{\Delta\Gamma t}{2} - C_f\cos(\Delta M t) + S_f\sin(\Delta M t)\right) .
\end{aligned} \tag{2.30}$$

The decay rates into the charge-conjugate final states are obtained by replacing f by $\bar{f}$ and A by $\bar{A}$. The factors D_f, C_f and S_f are defined as:

$$\begin{aligned}
D_f &= \frac{2\Re\lambda_f}{1+|\lambda_f|^2} , \\
C_f &= \frac{1-|\lambda_f|^2}{1+|\lambda_f|^2} , \\
S_f &= \frac{2\Im\lambda_f}{1+|\lambda_f|^2} ,
\end{aligned} \tag{2.31}$$

and respect the normalisation relation:

$$|D_f|^2 + |C_f|^2 + |S_f|^2 = 1 . \tag{2.32}$$

From the decay rates specified by the master equations (2.30), two time-dependent decay-rate asymmetries are constructed as:

$$\begin{aligned}\mathcal{A}_f(t) &= \frac{\Gamma_{\overline{B}^0\to f}(t) - \Gamma_{B^0\to f}(t)}{\Gamma_{\overline{B}^0\to f}(t) + \Gamma_{B^0\to f}(t)}\,,\\ \mathcal{A}_{\bar{f}}(t) &= \frac{\Gamma_{\overline{B}^0\to \bar{f}}(t) - \Gamma_{B^0\to \bar{f}}(t)}{\Gamma_{\overline{B}^0\to \bar{f}}(t) + \Gamma_{B^0\to \bar{f}}(t)}\,.\end{aligned} \tag{2.33}$$

In case the final state is not a *CP* eigenstate ($f \neq \bar{f}$), this equation describes the flavour asymmetries. For decays in which the final state is a *CP* eigenstate, and assuming $|q/p| = 1$, the time-dependent decay rate asymmetries are identical and referred to as the *CP* asymmetry:

$$\mathcal{A}_{CP}(t) = \frac{-C_f \cos(\Delta M t) + S_f \sin(\Delta M t)}{\cosh(\Delta\Gamma t/2) + D_f \sinh(\Delta\Gamma t/2)}\,. \tag{2.34}$$

2.3.3 *B* meson *CP* violation

The decays of charged and neutral *B* mesons can violate *CP* symmetry in several ways, which are categorised as three different types: *CP* violation in mixing, in decay and in interference between mixing and decay.

CP violation in mixing

CP violation in meson mixing can occur in the neutral *B* meson sector. It emerges from the time evolution of the B^0 and $\overline{B}^0$, as given by the Schrödinger equation (2.16). The oscillation probabilities for the $B^0 \to \overline{B}^0$ and $\overline{B}^0 \to B^0$ transitions are not necessarily identical, as seen in (2.24). The origin of different probabilities is a phase difference between the M_{12} and Γ_{12} matrix elements. It results in different magnitudes of the off-diagonal matrix elements in the effective Hamiltonian (2.17):

$$|2M_{12} - i\Gamma_{12}| \neq |2M_{12}^* - i\Gamma_{12}^*|\,. \tag{2.35}$$

A phase convention independent formulation for *CP* violation in mixing reduces this inequality to (2.19):

$$\left|\frac{q}{p}\right| = \left|\frac{2M_{12}^* - i\Gamma_{12}^*}{2M_{12} - i\Gamma_{12}}\right| \neq 1\,. \tag{2.36}$$

Therefore *CP* violation in mixing occurs in case the neutral *B* meson mass eigenstates are not *CP* eigenstates. The mixing is predicted to be an effect of $O(< 10^{-3})$.

CP violation in decay

The decay amplitudes of $B \to f$ and the *CP*-conjugate $\overline{B} \to \bar{f}$ decays are given by (2.27). These amplitudes differ by the sign of the weak phase ϕ_k, which is the source of this type of *CP* violation. The observable ratio of the decay amplitudes is used as a phase convention independent formulation of the criterium for *CP* violation in decay:

$$\left|\frac{\bar{A}_{\bar{f}}}{A_f}\right| = \left|\frac{\sum_k A_k e^{i(\delta_k - \phi_k)}}{\sum_k A_k e^{i(\delta_k + \phi_k)}}\right| \neq 1\,. \tag{2.37}$$

As charged B mesons do not feature *CP* violation in mixing, their decays offer practical channels to be measured for the study of *CP* violation in decay. The first observation of this type of *CP* violation was made in the $B_d^0 \to \pi^{\mp} K^{\pm}$ and $B^0 \to \pi^+\pi^-$ channels [31, 32].

CP violation in interference

CP symmetry can also be violated while there is neither *CP* violation in decay nor in mixing. In that case $|q| = |p|$ and $|\bar{A}_{\bar{f}}| = |A_f|$. The *CP* violation which can occur in this scenario is a result of interference between mixing and decay amplitudes of neutral B mesons. This can take place when both the B^0 and $\overline{B}^0$ can decay into the same final state f. In that case, the B^0 meson either decays directly or first undergoes a transition into a $\overline{B}^0$ and then decay. The magnitudes from equations (2.29) respect $|\lambda_f| = 1/|\lambda_{\bar{f}}|$, leaving the *CP* violation to take place between the phases:

$$\arg \lambda_f + \arg \lambda_{\bar{f}} \neq 1\,. \tag{2.38}$$

In case of decay to a *CP* eigenstate, the decay and mixing phases interfere such as to create a non-zero imaginary component:

$$\Im \lambda_f \neq 0\,. \tag{2.39}$$

2.4 B_s physics at LHCb

Existing B-physics experiments have extensively explored the $B_{u,d}$ mesons, resulting in the knowledge of the unitarity triangle angles as shown in figure 2.2. The centre-of-mass energy and projected luminosity available at the LHC allows to create several orders of magnitude more $B_{u,d}$ mesons than existing B factories, facilitating the reduction of statistical errors in the related measurements. In addition, LHC will copiously create B_s mesons, opening up its decay channels to inspection. To exploit B physics, the LHCb detector is required to have dedicated trigger capabilities to select b-quark decays online, whereas the B_s decays require high detector resolution, both in momentum and in decay-time. These conditions are met by the LHCb detector, as described in the next chapter. The reconstruction performance described in chapter 7 is discussed in the context of a selection of LHCb's decay channels of interest in the outlook, chapter 8. These channels are detailed next.

LHCb intends to make detailed measurements of $B_s^0 - \overline{B}_s^0$ mixing, using channels like $B_s^0 \to D_s^- \pi^+$, $B_s^0 \to J/\psi\phi$ and $B_s^0 \to J/\psi\eta$, in order to precisely determine the parameters ΔM_s, $\Delta\Gamma_s$ and ϕ_s. As seen from table 2.5, the angle γ has the largest uncertainty of the unitarity triangle angles. LHCb aims to improve the knowledge of the angle γ, while at the same time searching for signs of new physics. An approach of combining measurements of γ from tree-level only B decays, such as $B_s^0 \to D_s^\mp K^\pm$, $B^0 \to D^0 K^{*0}$ and $B^\pm \to D^0 K^\pm$, with those including box or penguin contributions, like $B^0 \to \pi^+\pi^-$ and $B_s^0 \to K^+K^-$, is adopted. A difference between their observations may be due to new physics, present as virtual particles in the loop diagrams. From this perspective, the $B_s^0 \to D_s^\mp K^\pm$, $B_s^0 \to J/\psi\phi$ and $B_{(s)}^0 \to h^+h'^-$ decays are discussed in this section. In addition, the mentioned channels are benchmarks for LHCb as they illustrate the detector performance for two-prong and four-prong decays, as well as for leptonically and hadronically triggered decays.

2.4.1 $\gamma + \phi_s$ from $B_s^0 \to D_s^\mp K^\pm$ decays

B_s^0 and $\overline{B}_s^0$ mesons can decay, with different amplitudes, to the same $D_s^\mp K^\pm$ final states. These decay modes are dominated by tree-level contributions, and no penguin contributions are expected. *CP* violation in interference occurs in this decay, which allows for the measurement of the weak phase $\phi = \gamma + \phi_s$.

The four relevant time-dependent decay rates are given by the master equations (2.30). Those show the need have input values for $\Delta\Gamma_s$ and ΔM_s, which can be obtained through observation of the $B_s^0 \to D_s^-\pi^+$ decay channel with uncertainties $\sigma(\Delta M_s) = 0.008\ \text{ps}^{-1}$ and $\sigma(\Delta\Gamma_s) = 0.03\ \text{ps}^{-1}$ [33].

As the $B_s^0 \to D_s^\mp K^\pm$ decay amplitudes are dominated by a single diagram, the time-dependent decay amplitudes of equation (2.27) relate as: $|A_f| = |\bar{A}_{\bar{f}}|$ and $|A_{\bar{f}}| = |\bar{A}_f|$. Using these relations and $|q/p| = 1$, the flavour asymmetries of equation (2.33) become:

$$\mathcal{A}_{f,\bar{f}}(t) = \frac{-(1-|\lambda_f|^2)\cos(\Delta M_s t) + 2|\lambda_f|\sin(\Delta_s \mp (\gamma+\phi_s))}{(1+|\lambda_f|^2)\cosh(\Delta\Gamma_s t/2) + 2|\lambda_f|\cos(\Delta_s \mp (\gamma+\phi_s))\sinh(\Delta\Gamma_s/2)}\,, \tag{2.40}$$

where Δ_s is the difference in the strong phases of the hadronic amplitudes of the B_s^0 and $\overline{B}_s^0$ mesons decaying into the same final state. For this decay channel, the λ parameters of equation (2.29) are:

$$\begin{aligned} \lambda_f &= |\lambda_f| e^{i(\Delta_s - (\gamma+\phi_s))}\,, \\ \bar{\lambda}_{\bar{f}} &= |\lambda_f| e^{i(\Delta_s + (\gamma+\phi_s))}\,. \end{aligned} \tag{2.41}$$

Both Δ_s and the weak phase $\phi = \gamma + \phi_s$ can be determined by measuring the phases of λ_f and $\bar{\lambda}_{\bar{f}}$. The B_s mixing phase ϕ_s can be determined from $B_s^0 \to J/\psi\phi$ decays, as discussed in the next subsection. Combining these measurements is expected to result in a sensitivity of $\sigma(\gamma + \phi_s) = 10.3°$, based on 2 fb^{-1} of data [34].

2.4.2 ϕ_s from $B_s^0 \to J/\psi\phi$ decays

The channel $B_s^0 \to J/\psi\phi$ is a decay to a *CP* eigenstate, implying $\lambda_f = \lambda_{\bar{f}}$. As the tree-diagrams and dominant penguin diagrams of this decay have the same weak phase, $|A_f/\bar{A}_f| = -\eta_f$ with $\eta_f = \pm 1$ for *CP* even and odd final states, respectively. Using the approximation $|q/p| = 1$, the time-dependent *CP* asymmetry (2.34) becomes:

$$\mathcal{A}_{CP}(t) = \frac{-\eta_f \sin(\phi_s)\sin(\Delta M_s t)}{\cosh(\Delta\Gamma_s t/2) - \eta_f\cos(\phi_s)\sinh(\Delta\Gamma_s t/2)}\,. \tag{2.42}$$

Measuring this asymmetry allows to determine the B_s mixing phase ϕ_s with a significance $\sigma(\phi_s) = 0.023$ rad, based on 2 fb^{-1} of data [35], from λ_f:

$$\begin{aligned} \lambda_{J/\psi\phi} &= -\eta_f e^{i\phi_s} \, , \\ \Im \lambda_{J/\psi\phi} &= \sin\phi_s \, . \end{aligned} \tag{2.43}$$

This approach is similar to the way in which the B_d mixing angle ϕ_d is determined from $B_d^0 \to J/\psi K_s$ decays. One difference is the need for an angular analysis of the $B_s^0 \to J/\psi\phi$ decays, as the final state contains two vector mesons, enabling contributions from both *CP* even (L=0,2) and *CP* odd (L=1) decay amplitudes.

2.4.3 γ from $B^0_{(s)} \to h^+h'^-$ decays

Decay channels of the form $B^0_{(s)} \to h^+h'^-$ can also provide measurements of γ, since $B_d^0 \to \pi^+\pi^-$ and $B_s^0 \to K^+K^-$ have tree-level contributions from $\bar{b} \to \bar{u}$ diagrams and in addition $\bar{b} \to \bar{d}(\bar{s})$ penguin diagrams [36]. Their penguin contributions offer the possibility to deduce the presence of new physics, for instance when compared to tree-level determinations of γ by decay channels like $B_s^0 \to D_s^{\mp}K^{\pm}$, $B_d^0 \to D^0K^{*0}$ and $B_d^0 \to \overline{D}^0K^{*0}$. Those channels offer a sensitivity of $\sigma(\gamma)$=9° from 2 fb^{-1} of data [37].

The $B_d^0 \to \pi^+\pi^-$ and $B_s^0 \to K^+K^-$ decay modes give rise to the following *CP* asymmetries:

$$\begin{aligned} \mathcal{A}_{CP}^{\pi\pi}(t) &= -C_{\pi\pi}\cos(\Delta M_d t) + S_{\pi\pi}\sin(\Delta M_d t) \, , \\ \mathcal{A}_{CP}^{KK}(t) &= \frac{-C_{KK}\cos(\Delta M_s t) + S_{KK}\sin(\Delta M_s t)}{\cosh(\Delta\Gamma_s t/2) + D_f \sinh(\Delta\Gamma_s t/2)} \, . \end{aligned} \tag{2.44}$$

The C and S factors are functions of seven parameter [36]:

$$\begin{aligned} C_{\pi\pi} &= G_1(d,\theta,\gamma) \quad , \quad S_{\pi\pi} = G_2(d,\theta,\gamma,\phi_d) \quad , \\ C_{KK} &= G_3(d',\theta',\gamma) \quad , \quad S_{KK} = G_4(d',\theta',\gamma,\phi_s) \quad , \end{aligned} \tag{2.45}$$

where $d(d')$ and $\theta(\theta')$ describe the relative strength and phase of penguin to tree contributions for the $B_d(B_s)$ decays, respectively. As the two decay modes are related through the interchange of down and strange quarks, U-spin flavour symmetry of strong interactions links the strength and phase ratios as [36]:

$$d \approx d' \quad , \quad \theta \approx \theta' \quad . \tag{2.46}$$

Therefore, combining the measurements from $B_d^0/\overline{B}_d^0 \to \pi^+\pi^-$ and $B_s^0/\overline{B}_s^0 \to K^+K^-$ decays results in a system of four equations and five unknowns. Two of these unknowns are the B_d and B_s mixing angles ϕ_d and ϕ_s, which can be determined from $B_d^0 \to J/\psi K_s$ and $B_s^0 \to J/\psi\phi$ decays. The remaining three unknowns contain the angle γ, which is expected to be determined with a significance of $\sigma(\gamma)$=10° from 2 fb^{-1} of data [38].

Chapter 3

Experiment

The Large Hadron Collider [39] (LHC) is the planned successor of the Large Electron Positron (LEP) accelerator since 1993. It will collide protons at a centre-of-mass energy $\sqrt{s} = 14$ TeV, allowing tests of the Standard Model and searches for additional physics at an as yet unexplored energy scale. The LHC infrastructure provides four interaction points, of which one is designated for use by a dedicated B-physics experiment. Originally the COBEX, GAJET and LHB detector designs competed for this opportunity. Their proponents have subsequently united into the Large Hadron Collider beauty collaboration and designed the LHCb detector [40]. The LHCb experiment specialises in heavy-flavour physics, including the search for new physics in CP violation, and rare decays of beauty and charm hadrons. This chapter describes the LHC facility in section 3.1, the LHCb detector in sections 3.2, 3.3 and 3.4, and the trigger in section 3.5.

3.1 The Large Hadron Collider

The European Organization for Nuclear Research (CERN) is a high-energy physics laboratory, located on the border between France and Switzerland, near the city of Geneva. CERN was founded by twelve countries in 1954 and now has 20 member states, supplemented by collaboration with many other nations. It focusses the efforts to study elementary particles and their interactions by hosting infrastructure for physicists to conduct experiments.

One part of the underground infrastructure is a 27 km long nearly circular tunnel, which was constructed to accommodate the LEP accelerator. The LHC has been designed as the successor of LEP. The LHC machine is assembled in the LEP tunnel and also reuses part of the existing pre-acceleration facilities. These accelerators are the Proton Synchrotron Booster (Booster), the Proton Synchrotron (PS) and the Super Proton Synchrotron (SPS), whose layout is shown schematically in figure 3.1.

LHC [41] is capable of accelerating proton beams as well as lead-ion beams. Protons are produced by stripping hydrogen atoms, which are then accelerated to 50 MeV by the LINAC2. The Booster, PS and SPS increase the energy of the protons from 50 MeV to respectively 1.4 GeV, 25 GeV, and finally 450 GeV. Two oppositely moving beams of protons will be injected into the LHC, which provides

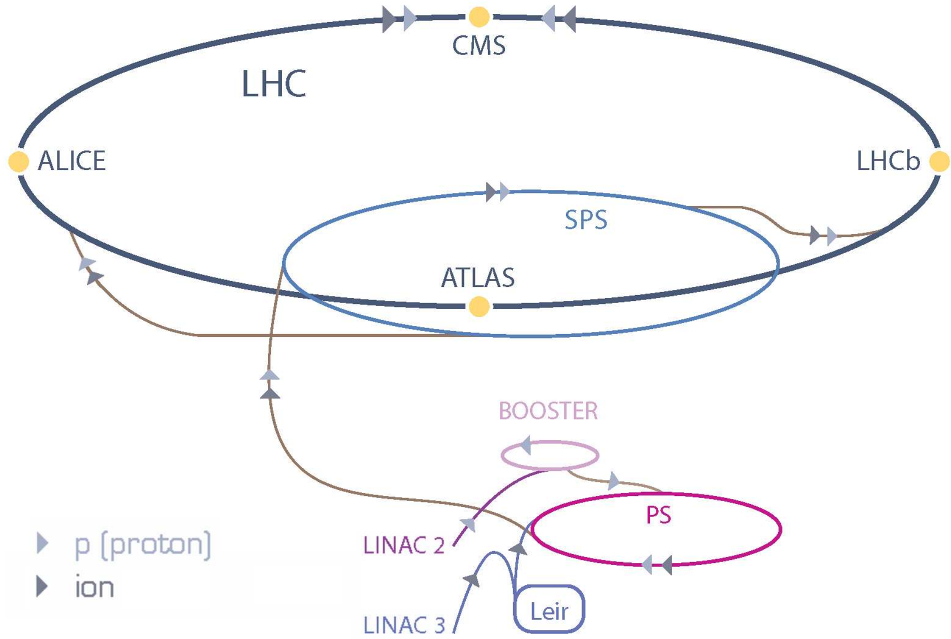

Figure 3.1: *Layout of a part of the accelerator complex at CERN. The protons travel through the LINAC2, Booster, PS, SPS and LHC machines and are collided at the interaction points of ALICE, ATLAS, CMS and LHCb. Ions are first accelerated by the LINAC3 and LEIR after which they are inserted in the Booster.*

a final centre-of-mass energy of 14 TeV at a design luminosity of $10^{34}\text{cm}^{-2}\text{s}^{-1}$. Lead ions are created from a pure sample of lead at the beginning of the LINAC3. The ions are accelerated to 4.2 MeV per nucleon by the LINAC3 and further to 72 MeV per nucleon by the Low Energy Ion Ring (LEIR). After travelling through the pre-acceleration machines, lead-ion beams can be accelerated up to a combined centre-of-mass energy of 1148 TeV at a luminosity of $10^{27}\text{cm}^{-2}\text{s}^{-1}$ by the LHC.

A total of 9593 magnets are used in the LHC [41] to bend and focus the two beams along its length of 26659 m. At an energy of 7 TeV per proton, given the layout of the machine, the bending magnets need to establish a magnetic field of 8.33 T to keep the beams on track. This is achieved by 1232 dipole magnets with dual apertures, see figure 3.2, allowing both beams to be bent by each magnet. The dipoles are made from Niobium-Titanium alloy cable, which is superconducting at the operational temperature of 1.9 K. At this temperature, the dipoles can conduct a current of 11850 A. The magnets and iron return yokes are cooled by a system containing 120 tonnes of superfluid Helium.

Radio frequency cavities are used to accelerate the beams and to compensate for energy losses sustained during their 7 hour nominal operational lifetime. There are eight superconducting cavities for each beam, which are cooled to 4.5 K. The cavities each deliver a 2 MV electric field for acceleration. Each beam is structured in bunches as the oscillating RF fields can only accelerate the protons when in the proper phase. As a result, the bunches are actively compacted by the RF fields, ensuring optimal luminosity.

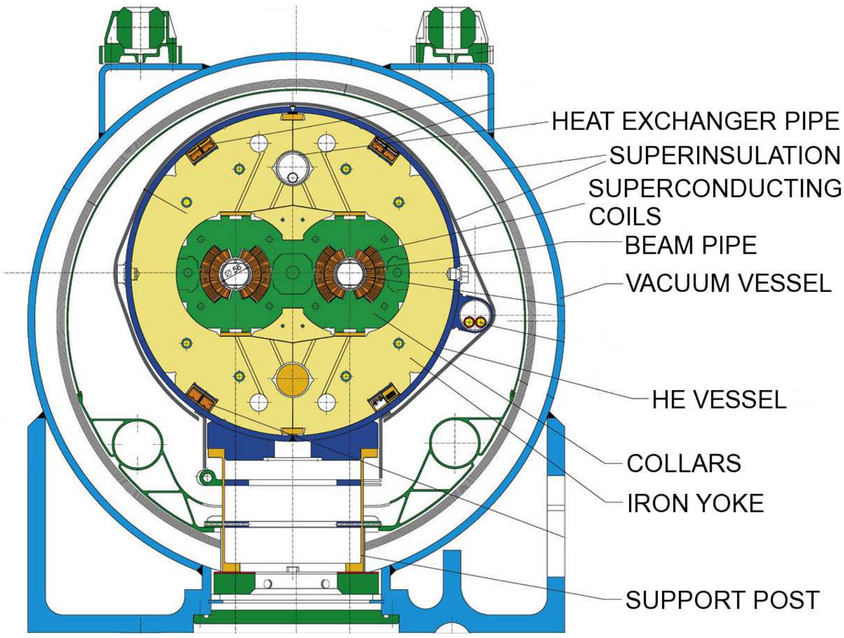

Figure 3.2: *A cross-sectional view of a LHC dipole magnet. Inside the support structure, the two beam pipes, the superconducting magnet coils, the iron return yoke, and the cooling and insulation components are shown.*

A proton beam comprises 2808 bunches, initially consisting of $1.1 \cdot 10^{11}$ protons each. The bunches are separated by 25 ns, corresponding to a bunch crossing frequency of 40 MHz. In order to allow time for the kicker magnets to switch on during beam injection and beam dumping, there are several gaps in the bunch structure. This results in an effective interaction frequency ν_{eff} of 31.6 MHz. The proton bunches measure 7.55 cm in length (RMS) when circling the accelerator and are focussed to 70.9 µm (RMS) at the LHCb interaction point (IP8), increasing the luminosity [42].

The proton-proton collisions can be either elastic or inelastic in nature. In case of an elastic *p*-*p* collision, the protons remain intact and predominantly continue travelling within the beam pipe. Therefore most collisions of this type cannot be detected. Inelastic collisions break up the protons and offer numerous particles for detection. At a centre-of-mass energy of 14 TeV, the predicted cross-section of inelastic *p*-*p* collisions is 80 mb, compared to 20 mb for elastic collisions [43]. The number of inelastic collisions per bunch crossing follows a Poisson distribution with a mean given by:

$$< n_{\mathrm{pp}} >= \frac{\mathcal{L}\sigma_{\mathrm{inel}}}{\nu_{\mathrm{eff}}}, \tag{3.1}$$

where $\mathcal{L}$ is the luminosity, σ_{inel} is the inelastic cross-section and ν_{eff} is the effective interaction frequency. At the design luminosity of $10^{34}\mathrm{cm}^{-2}\mathrm{s}^{-1}$, a mean of 27 collisions is expected per bunch crossing. It scales linearly with the luminosity, which deteriorates exponentially with an expected characteristic lifetime of 10 hours during operation.

The proton beams are crossed at four locations along the LHC machine. Each of these interaction regions has been assigned to one of the four main detectors: LHCb, Compact Muon Solenoid (CMS), A Large Ion Collider Experiment (ALICE) and A Toroidal LHC ApparatuS (ATLAS). They are supplemented by the detectors of the Large Hadron Collider forward (LHCf) and TOTal Elastic and diffractive cross-section Measurement (TOTEM) experiments. The experiments are summarised as follows:

- CMS [44, 45] and ATLAS [46, 47] are general purpose detectors, with 4π solid-angle coverage of their interaction regions. Their physics programmes include precision measurements of Standard Model quantities, the search for the Higgs boson(s), for signs of supersymmetry and other extensions of the Standard Model, and for indications of the existence of extra dimensions.

- The ALICE detector [48, 49] has been designed with the study of quark-gluon plasma in mind, a state of matter which can be created by heavy-ion collisions. The temperature and density of such a plasma is sufficient to allow quarks and gluons to become deconfined. This state of matter is considered to have existed after the Big Bang and to have undergone a phase transition into hadronic matter.

- LHCf [50, 51] is an experiment located along the accelerator, 140 m away from the ATLAS detector. It will measure particles produced at ATLAS in the very forward region. These are similar to the particles in showers which are initiated by cosmic rays in the atmosphere. This information allows to test models used to estimate the primary energy of ultra high-energy cosmic rays.

- TOTEM [52, 53] detects very forward moving particles to determine the total proton-proton cross-section. In addition it will study elastic scattering and diffractive processes at the LHC. It consists of Gas Electron Multiplier detectors and cathode strip chambers, which are installed around the interaction region of CMS.

- The LHCb experiment [43, 54] specialises in measuring *CP* violation in *B*-hadron decay processes and studying rare *B*-hadron decay modes for signs of new physics. Its design is detailed in the remainder of this chapter.

3.2 The LHCb detector

The LHCb experiment [43, 54, 55] intends to precisely measure the particles produced in *B*-meson decays, which are predicted to be produced in larger amounts at the LHC than by previous accelerators. Certain *B*-meson decay modes provide insight into the phenomenon of *CP* violation, while some of the rare decay modes can exhibit signs of new physics. Study of these decays requires an efficient, robust and flexible trigger in order to select a range of interesting event types out of a considerable amount of background. Of these events, the primary and secondary vertices must be distinguished, as B-hadron decays result in secondary vertices. The momentum and vertex resolutions must be sufficient to reduce combinatorial background and to offer a proper-time resolution that enables the study of B_s-meson oscillations. Particle identification over a wide momentum range allows for the separation of B-hadron decay modes that are topologically and kinematically alike. In addition to electron, muon, γ and π^0 detection, identification of kaons and pions is critical in order to reconstruct hadronic B-meson decay final states.

Reconstructing the primary and secondary vertices in B events becomes more complicated as the number of p-p collisions in a single bunch crossing increases. Multiple collisions also increase the radiation damage to the detector. Given these considerations, the luminosity has been found to be optimal in the range from $2 \cdot 10^{32}\text{cm}^{-2}\text{s}^{-1}$ to $5 \cdot 10^{32}\text{cm}^{-2}\text{s}^{-1}$ [43]. An average of 0.53 inelastic collisions per bunch crossing is expected at those running conditions. The collision multiplicity probability distributions and the impact of additional collisions per bunch crossing on the average number of $b\bar{b}$ events are shown in figure 3.3.

The heavy-flavour hadrons of interest to the LHCb experiment are predominantly present in identical forward and backward cones, as shown in chapter 4. A single arm spectrometer design has been decided on for LHCb, capturing the forward cone between 10 and 300 respectively 250 mrad in the bending and non-bending directions. These correspond to the horizontal x-z and vertical y-z planes. A side view of the LHCb detector is given in figure 3.4, showing its main components and their locations in the cavern. These components are the beam pipe, magnet system, VErtex LOcator (VELO), Tracker Turicensis (TT), Inner Tracker (IT), Outer Tracker (OT), Ring Imaging CHerenkov detectors (RICH1 and RICH2), electromagnetic and hadronic calorimeters (ECAL and HCAL) and muon detector (MUON). They are detailed in this and the following two sections.

3.2.1 Beam pipe

The LHCb beam pipe [54, 55] serves to separate the LHC machine vacuum from the atmosphere. It is situated in the upper pseudorapidity[1] region of the LHCb detector, running from the VELO until the end of the muon chambers. Primary particles passing through the material of the beam pipe can result in the creation of secondary particles. This increases the occupancy of the RICH and tracking sub-detectors with unwanted hits and should be minimised. An optimised gas-tight design, offering a minimal amount of material to traverse by primary particles, while capable of withstanding the mechanical stress resulting from the pressure difference, is shown in figure 3.5.

The beam pipe comprises four sections, consisting of conical tubes, flanges and bellows. At the end of the VELO, the beam pipe is welded to the 2 mm thick Aluminium VELO exit window, which covers the full acceptance. The sections are made up by a 25 mrad Beryllium cone, followed by three 10 mrad Beryllium cones. Constructing the tubes from Beryllium of 1 to 2.4 mm thickness in a conical shape

[1] The pseudorapidity η is defined as $\eta = -\ln[\tan(\theta/2)]$, where θ is the angle with the beam-axis.

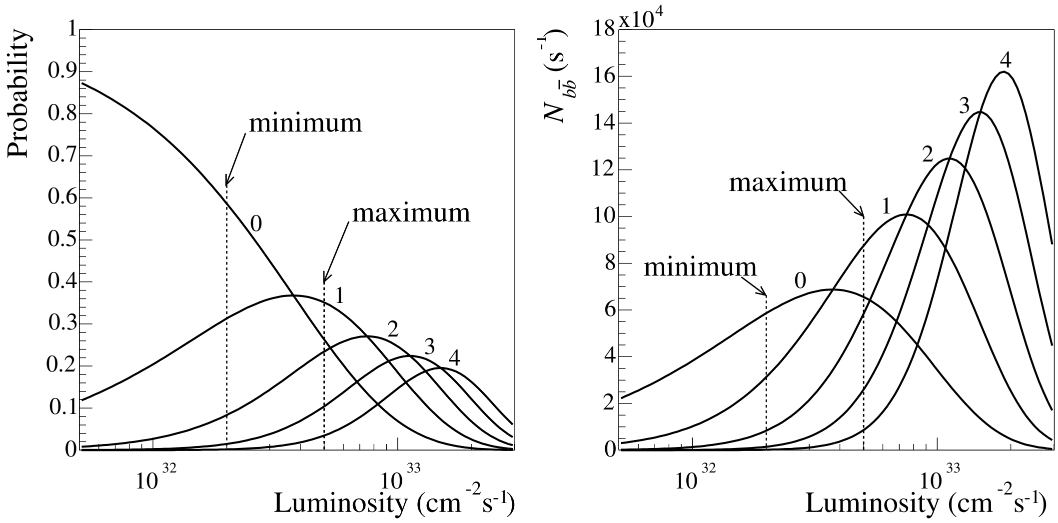

Figure 3.3: ***(left)*** *The probability distributions for zero to four inelastic collisions per bunch crossing as a function of the luminosity.* ***(right)*** *The impact of additional collisions per bunch crossing on the number of $b\bar{b}$ events per second as a function of the luminosity. In both plots, the limits of the optimal luminosity range are indicated.*

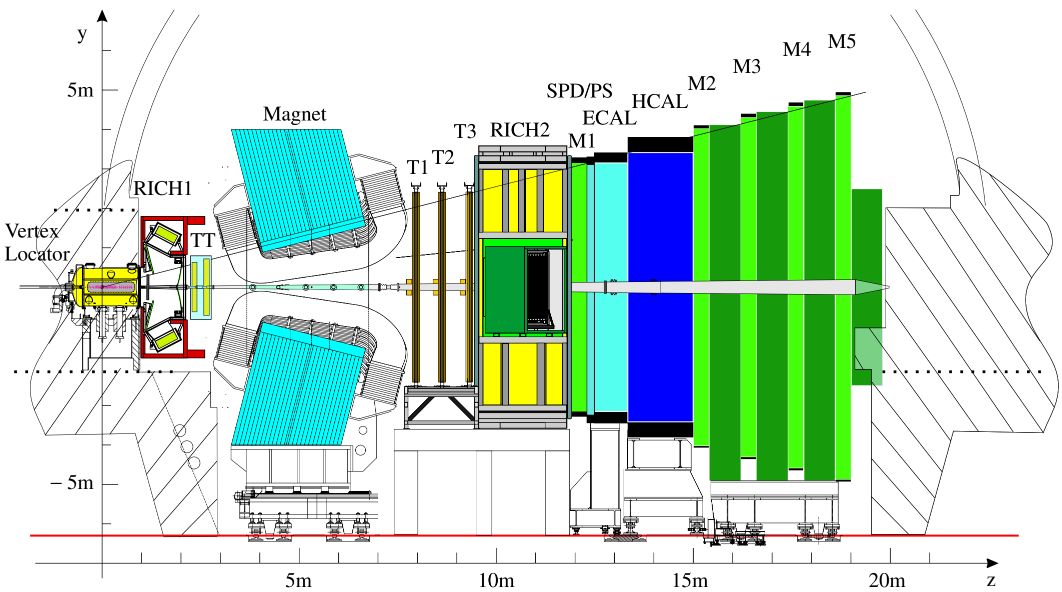

Figure 3.4: *A schematic view of the LHCb detector, showing the magnet, the beam pipe, the tracking sub-detectors, the RICH detectors, the calorimeter system, and the Muon stations as located within the cavern.*

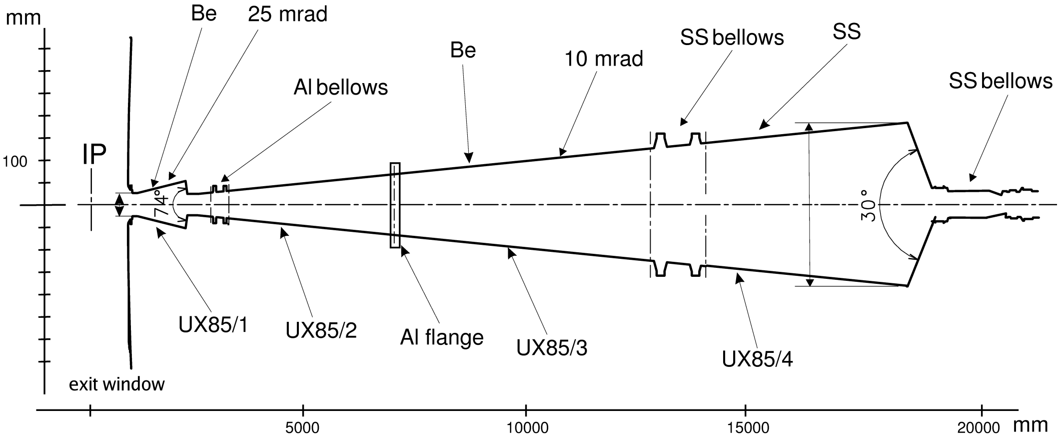

Figure 3.5: *Layout of the LHCb beam pipe, showing the four main conical sections UX85/1 – 4, connected by flanges and bellows.*

minimises the amount of material encountered by primary particles. The segmentation is dictated by mechanical constraints and optimised to place the Aluminium flanges and bellows in locations where the least number of produced secondary particles can reach the tracking detectors. A final section is formed by two 10 mrad stainless steel cones which pass through the calorimeters and the muon system, where secondaries are a less important design factor.

An average pressure between 10^{-8} and 10^{-9} mbar in the beam pipe is obtained by ion pumps and a non-evaporative getter coating on the vacuum chambers. Once saturated, the coating can be reactivated by heating it to 200°C for 24 hours. All components of the beam pipe are rated to temperatures of 250°C and above. Bellows are incorporated in the design to deal with the thermal deformation of the beam pipe components.

The obtained pressure difference over the conical beam pipe results in an average longitudinal force on the beam pipe of 0.58 N mm^{-1}. Stainless steel cables and rods are connected to Aluminium collars at each section to keep the beam pipe in place.

3.3 Tracking system

Charged particle detection for track reconstruction purposes is done by the tracking sub-detectors. These are the VELO, TT, IT and OT, which are described in this section. In order to allow for particle momentum measurements, a magnet provides a magnetic field in which the charged-particle paths bend with a radius of curvature proportional to their momentum.

3.3.1 Magnet

A magnetic field is needed to bend the trajectory of charged particles and thereby enable the tracking detectors to measure their momentum up to 200 GeV within

0.5% uncertainty. This requires an integrated field of 4 Tm as seen by particles originating from the interaction region. The LHCb magnet [54, 56] is capable of providing such a magnetic field within the detector, with the principal field component oriented along the y-coordinate.

The magnet comprises two trapezoidal coils inside a rectangular steel yoke frame, as shown in figure 3.6. Each coil is bent 45° on the transverse side into a saddle shape, producing a wedge shaped gap slightly larger than the acceptance of LHCb. The coils consist of 15 layers, each formed by 15 windings of square Aluminium tube some 320 meters in length. Water is circulated inside the tubular conductor at a rate of 150 m^3h^{-1} for cooling purposes, as the total magnet consumes up to 4.2 MW. A wrapping of glass-fibre tape is applied to insulate the windings and the layer is vacuum-impregnated with raisin for stability.

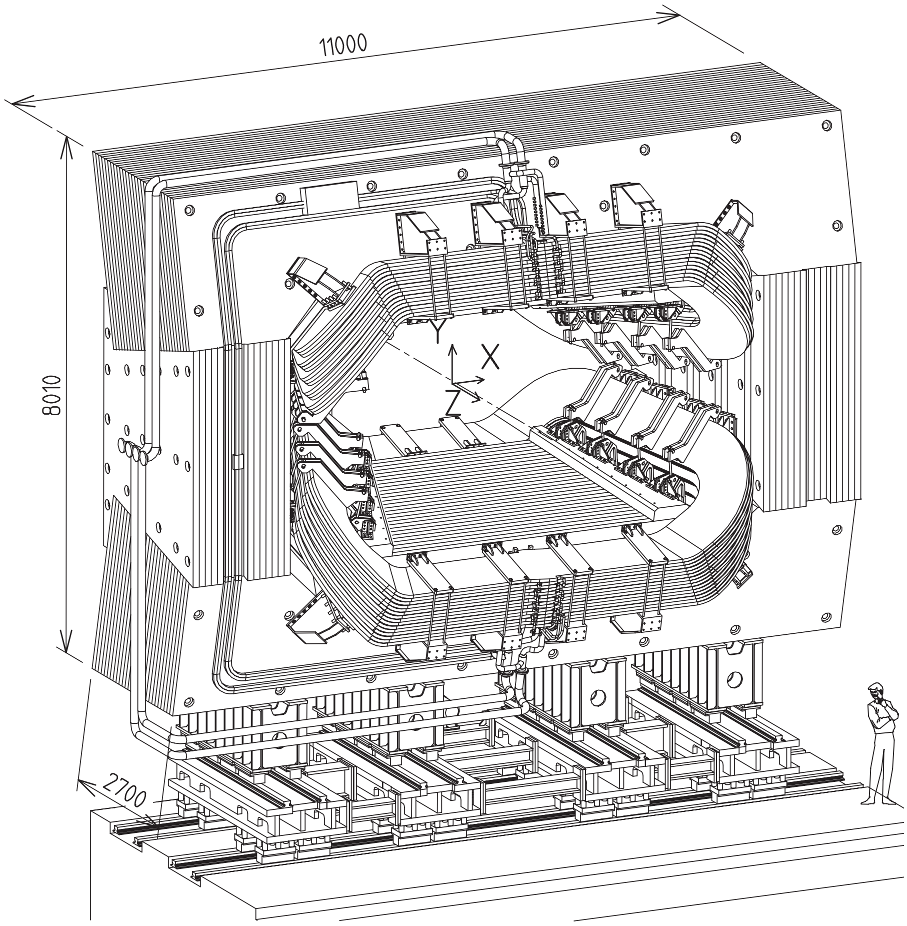

Figure 3.6: *Perspective view of the LHCb magnet, showing the trapezoidal coils and steel yoke.*

The magnetic flux generated by the two coils is shaped and guided by a steel yoke. It produces a vertical magnetic field in the gap between the pole faces. The yoke is assembled from low carbon steel plates of 100 mm thickness. In the horizontal plane the plates are trapezoidal in shape and are arranged orthogonal to the plane of the coils. Vertical uprights close the flux return.

3.3.2 Vertex Locator

The VELO [54, 55, 57] is installed directly around the interaction point. It allows to measure the trajectories of charged particles and to determine the vertices from which they originate. At LHCb, the average distance between the production vertex and the vertex of a decayed B hadron is approximately 12 mm [58]. The trigger system uses this relatively long decay length to select B events. The resolution is sufficient to identify and reconstruct B-hadron decays as well as to measure their lifetime and the B_s oscillation frequency. An average uncertainty in the primary vertex position of 42 µm along the beam and 10 µm in the perpendicular plane is predicted, which translates into an average B-decay proper-time resolution of 40 fs.

The sensitive component of the VELO detector is formed by 21 stations, each consisting of two halves with each two silicon strip sensors, which measure the R and ϕ coordinates. These are placed along the beam, enclosing the nominal interaction point. The layout of the stations is such that tracks between 15 and 390 mrad from a vertex located inside 106 mm, which corresponds to 2σ of the nominal interaction point, cross at least three stations. This requirement ensures that the track will be properly reconstructed. The resulting arrangement of the stations which respects the requirements, while being close to the beam for precision, and introducing a minimum amount of material to traversing particles, is shown in figure 3.7. An additional two VELO stations, located more upstream, are called the pile-up system. This identifies bunch crossings with multiple interactions and through the first-level hardware trigger vetoes such events, as detailed in subsection 3.5.1.

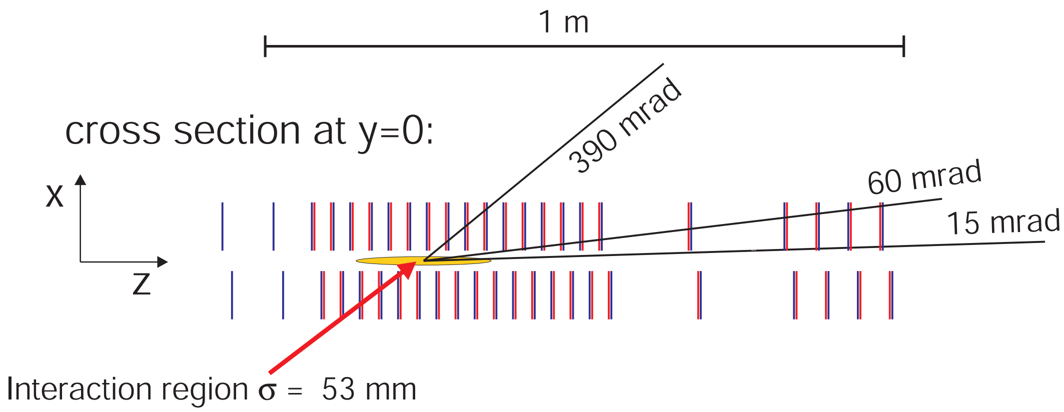

Figure 3.7: *Layout of the VELO tracking stations, showing that at least three stations are crossed by particles within the acceptance.*

The VELO uses semi-circular silicon sensors in a 10^{-4} mbar vacuum, separated from the machine vacuum by a corrugated 300 µm thick Aluminium foil. A corrugated design minimises the interaction length encountered by particles, allows the sensors to overlap and offers greater mechanical strength compared to a flat foil. The foil protects the machine vacuum from the lower quality vacuum inside the VELO and shields the sensors from the RF currents induced by the beams. On the sensor side, the foil is coated to electrically insulate it from the sensors. Both the sensors and foil can be moved to and from the beam line within a range from 5 mm to 30 mm, in order to protect the sensors from damage during beam injection. During measurements, the silicon sensors are placed as close to the beams as possible, as extrapolation degrades the accuracy of measured vertices. This distance is 8.2 and 7.0 mm for respectively R and ϕ sensors, dictated by the extent of the beam halo.

Single sided n-on-n silicon strip sensors of 300 μm thickness are adopted for measuring the R and ϕ coordinates of a passing particle, see figure 3.8. An R sensor comprises 2048 arc-shaped strips, grouped in four radial sectors of 512 strips each to form a half-circle. Their pitch increases from 38 μm on the inside to 101.6 μm on the outside. A ϕ sensor has 2048 straight line strips, arranged in an inner sector of 683 strips and an outer sector of 1365 strips. Their pitch ranges from 37.7 μm to 78.3 μm in the inner region and from 39.3 μm to 96.6 μm in the outer region. The strips in the inner sector are placed at a 20° angle to the radial and the outer sector strips at −10°. This design homogenises the detector occupancy, keeping it below the 1% level. A sensor of R type is mounted back-to-back with a sensor of ϕ type in order to determine the point of passage in three dimensions. Such a pair or module is roughly shaped as a half-circle, covering 182°. Two opposite modules, separated by 15 mm in z, form a station and have a circular aperture in the middle to allow the beam to pass through.

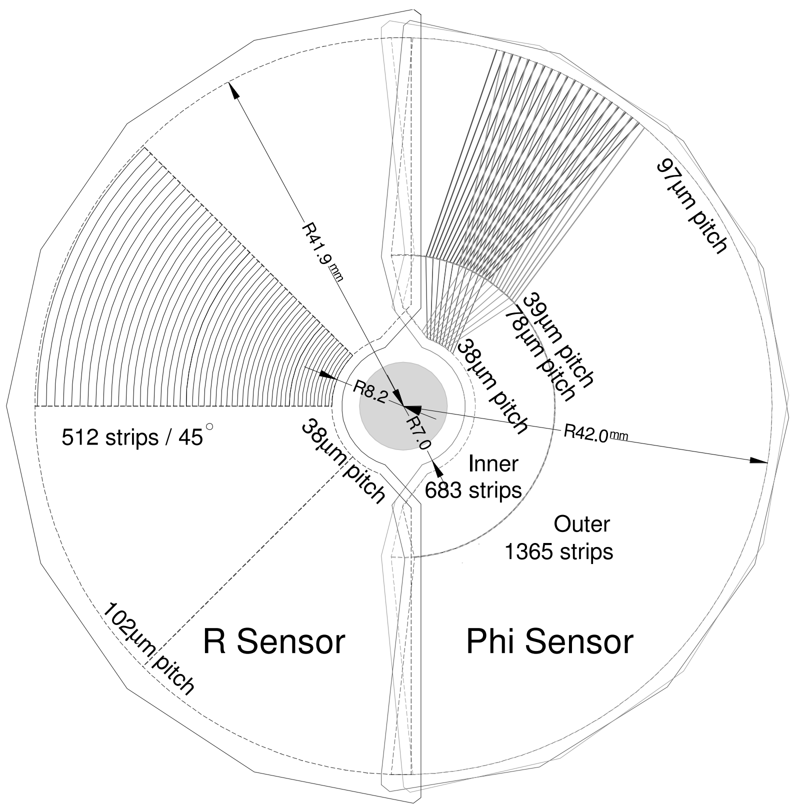

Figure 3.8: *Schematic of both R and ϕ type sensors, showing their overall dimensions and their strip layout.*

3.3.3 Tracker Turicensis

The TT [54, 55] is a silicon tracker, positioned between RICH1 and the magnet. The magnet's fringe field permeates the region between the VELO and the TT with an integrated field of 0.15 Tm. This enables the TT to determine the momentum of charged particles. It measures particle trajectories, including those of low-momentum particles, which are bent out of the acceptance before the T stations. In addition, the TT can detect the decay products of long-lived neutral particles, which decay outside of the VELO detector volume.

The TT has four detection layers, covering an angular region from 30 mrad up to the outer acceptance of LHCb. Its layers consist of p-on-n silicon strip sensors, grouped in pairs which are about 27 cm apart. The outer layers are oriented vertically, while the two inner layers have their strips angled at respectively $-5°$ and $5°$. This is referred to as an x-u-v-x configuration, and enables the TT to measure both x and y coordinates. Figure 3.9 shows the layout of the third layer from the interaction point. The layers consist of an upper and lower side. The first two layers form TTa and are composed of 30 staggered silicon ladders, which overlap a few mm in x. The other two layers form TTb and each comprise 34 ladders. Seven sensors of 9.64 by 9.44 cm, with a thickness of 500 μm, are mounted on aluminium-nitride baseplates to form the ladders or half modules. A frame of carbon-fibre and glass-fibre rails is used to support the ladders mechanically.

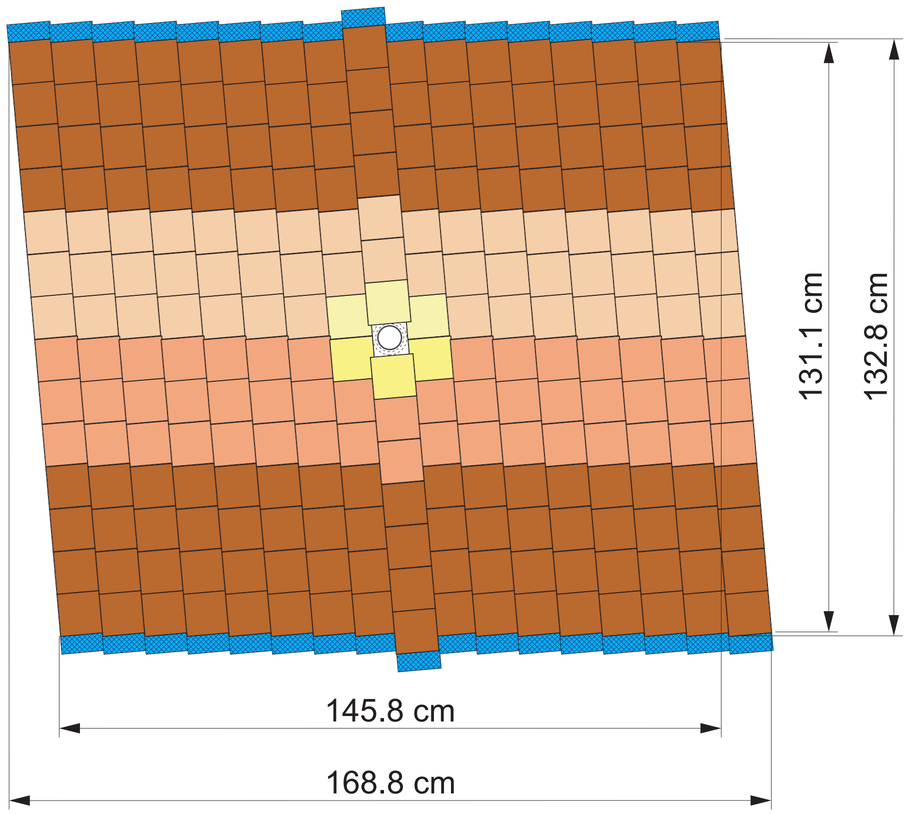

Figure 3.9: *Layout of the v layer of TTb, showing the ladders with sensors and the read-out electronics at the outer ends.*

The silicon sensors require an environmental temperature below 5°C in order to achieve the design performance. In order to facilitate this, the layers are enclosed within a thermal-insulating box that also provides electrical and optical shielding. The insulating walls of the detector box are formed by 40 mm thick foam, which is layered with Kevlar and Aluminium foils on both sides. Each half module is thermally and mechanically connected to an Aluminium support balcony, which is located outside of the acceptance. Four 8 mm thick Aluminium cooling plates are placed along the outer walls of the box. They contain ducts through which liquid C_6F_{14} at −15°C flows as a cooling agent. This system is supplemented by four copper cooling elements. In order to prevent condensation on the detectors, the box is continuously flushed with dry nitrogen gas.

A strip pitch of 183 μm results in a single hit resolution better than 50 μm, making multiple scattering the dominant factor in the momentum resolution. Given the particle density varying from $5 \cdot 10^{-2}$ to $5 \cdot 10^{-4}$ cm^{-1}, strip lengths increase with distance from the beam axis, thus maintaining an occupancy of a few percent. A signal-to-noise ratio better than 12:1 ensures sufficient single-hit efficiency for track reconstruction.

3.3.4 Tracking Stations

The region between the magnet and the RICH2 detector is occupied by the three Tracking Stations. Charged particles passing through the magnet are bent and spread out over a covered surface of 5971 × 4850 mm^2. As the density of tracks decreases with the distance from the beam pipe, a sectioning, based on two detector granularities, has been made. The inner region is covered by the silicon sensors of the Inner Tracker whereas the outer region is covered by the straw tubes of the Outer Tracker. Their dimensions are dictated by the geometry of the beam pipe, the design acceptance of LHCb, and a maximal allowed occupancy of 10% in the OT detector. In collaboration, the IT and OT provide position measurements, which can be used to determine the momentum of a particle. In order to detect a particle track with sufficient efficiency to reconstruct decays with multiple particles in the final state, a total of 12 detection layers is used.

A cross-shaped surface around the beam pipe is covered by four IT [54, 55] detector boxes per station, as illustrated in figure 3.10. This is a region 120 cm wide and 40 cm high, accounting for 1.3% of the total T-station area. At a mean particle flux of $1.5 \cdot 10^5$ cm^{2}s^{-1} in this region, on average 25% of the charged particle tracks in the T stations pass through this surface, resulting in a 2% occupancy of the IT. Each of the IT boxes contains four layers of silicon strip sensor ladders, arranged in a x-u-v-x configuration, similar to the TT. The main difference with the TT is the use of one silicon sensor per ladder for the top and bottom boxes and two sensors per ladder in the left and right boxes. The sensors are 7.6 cm wide and 11 cm long, with a thicknesses of 320 μm and 410 μm for respectively the single and double sensor ladders. These thicknesses have been determined to minimise the material budget of the detector, while offering a sufficiently high signal-to-noise ratio. Both have a strip pitch of 198 μm and a resolution of 50 μm.

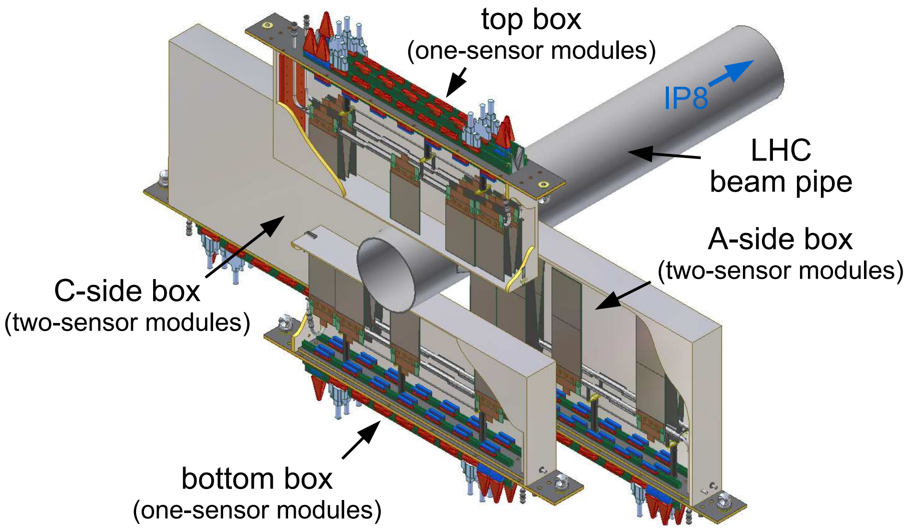

Figure 3.10: *A 3D view of an IT station with four boxes, each containing four layers of sensors.*

The OT [54, 59] covers an acceptance up to 300 mrad in the horizontal and 250 mrad in the vertical plane, excluding the region of the IT, save for some overlap for alignment purposes. There are three OT stations, each formed by four layers of modules, arranged in the same x-u-v-x layout as the IT and TT, see figure 3.11. This implies that the two x layers are vertical and the inner two layers are rotated by respectively -5° and 5°, enabling a measurement of the vertical y-coordinate. Different length modules are used, depending on their location with respect to the IT. In total 168 long and 96 short modules form the OT. Each module is made up of two staggered layers of 64 straw-tubes, glued to a 10 mm thick rigid foam core and covered by 120 μm thick carbon-fibre foils. The tubes have an inner diameter of 4.9 mm and are filled with a gas mixture of Ar/CO_2, offering a drift-coordinate resolution of 200 μm. A tube is produced from an inner layer of 40 μm thick carbon doped polyimide and a gas-tight outer layer composed of 25 μm polyimide and 12.5 μm Aluminium for electrical conduction. The anode wires are made from gold-plated tungsten, with a diameter of 25.4 μm and are strung at a tension of 0.7 N. Electrons, which are created in the gas by traversing charged particles, drift towards the wire under the influence of a voltage difference between the straw wall and the wire. Near the wire, the electrons are multiplied by the large local field gradient to produce a detectable signal on the wire.

3.4 Particle identification

Particle identification in the LHCb experiment is provided by three detector systems. The two RICH detectors identify charged hadrons, the electromagnetic and hadronic calorimeters are used to identify electrons, photons and hadrons, and the muon system identifies muons.

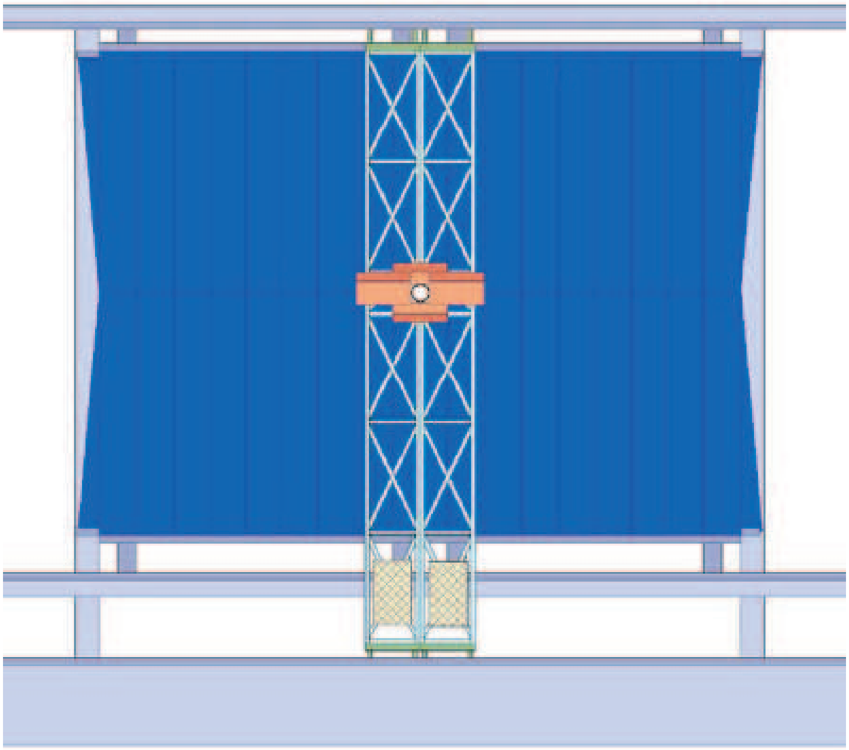

Figure 3.11: *Front view of an Outer Tracker station, showing x, u and v layers and the IT around the beam pipe.*

3.4.1 RICH

LHCb's two RICH [54, 60] detectors serve to identify charged particle species and especially to distinguish pions from kaons. Several interesting final states of B hadron decays are topologically similar and can be distinguished by identifying their pion and kaon content. Additionally, kaon identification is used to determine the b quark flavour of neutral B hadrons at the time of creation, a procedure known as flavour tagging. Separation between pions and kaons in the momentum range from 1 to 100 GeV is required to achieve the physics goals of LHCb. The electron and muon identification efficiency is 95% with a 1% pion misidentification rate. Kaon-pion separation efficiency is 90%, with a misidentification rate of 10% in the momentum range from 10 to 80 GeV [61].

The polar angle distribution of the final state pions of the $B_d^0 \to \pi^+\pi^-$ decay is not uniform as a function of momentum, as shown in figure 3.12. This inspired the design using two detectors [55, 60], each covering a different region of this angle versus momentum plane. RICH1 is aimed at particle identification in the momentum range from 1 to 60 GeV, covering the horizontal plane from 25 to 300 mrad and the vertical plane from 25 to 250 mrad. RICH2 detects charged particles in a momentum range from 15 to 100 GeV and has a horizontal acceptance of 15 to 120 mrad and a vertical acceptance of 15 to 100 mrad.

Charged particles polarise atoms when moving through a dielectric medium, by displacing the electrons with their electric fields. The electrons emit photons as

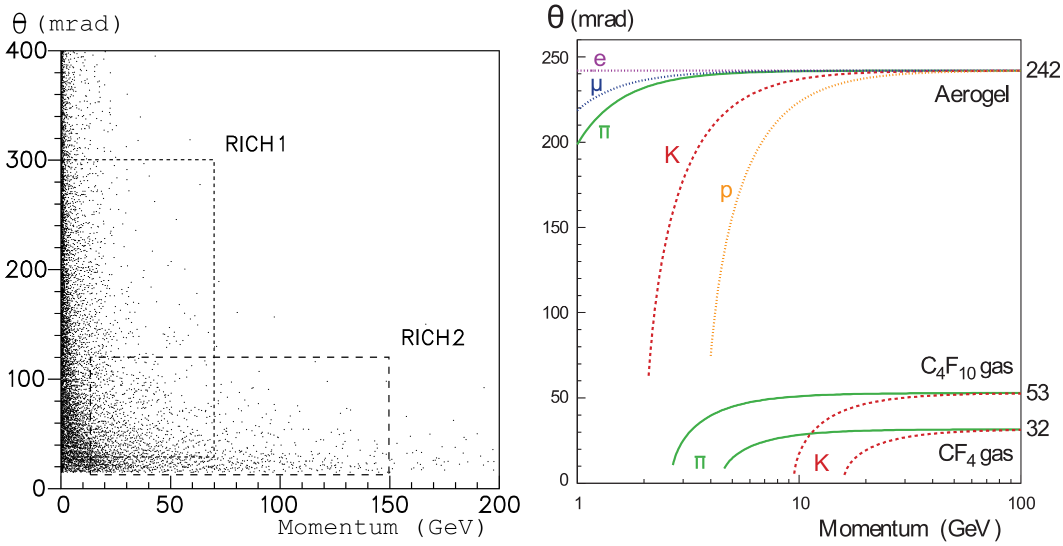

Figure 3.12: ***(left)** The polar angle distribution of pions from $B_d^0 \rightarrow \pi^+\pi^-$ decays, plotted as a function of momentum. Indicated are the regions which are covered by the two RICH systems of LHCb. **(right)** The Cherenkov angle as a function of momentum, for different particles, as produced when traversing the three types of radiator material.*

they return to equilibrium, which can interfere destructively or constructively. In case the particle's speed exceeds the speed of light in the medium, the interference is constructive and Cherenkov light is radiated. The light is emitted in a cone with a characteristic Cherenkov angle θ_C, given by [62]:

$$\cos(\theta_c) = \frac{1}{n}\sqrt{1+\left(\frac{m}{p}\right)^2} = \frac{1}{n\beta}, \tag{3.2}$$

where n is the medium's refractive index, p is the particle's momentum, m is its mass and β is the particle's velocity divided by the speed of light. Therefore a particle can be identified by measuring the Cherenkov angle and the particle's momentum.

The three radiator materials used in the two RICH detectors have different refractive indices and emit photons under angles as plotted in figure 3.12. As dictated by formula (3.2), given a detection resolution for the angle θ_c, particles with different masses become indistinguishable at higher momenta. The solution to this issue is to utilise several radiator materials to cover the intended momentum range. RICH1 has a 5 cm thick layer of silica aerogel at the VELO side, which offers kaon identification above a momentum of 2 GeV and pion-kaon separation up to 10 GeV. This is followed by an 85 cm path through fluorocarbon (C_4F_{10}) gas, which enables pion-kaon separation up to 50 GeV at a 3σ level. The CF_4 radiator is used in RICH2 to identify particles from 15 to 100 GeV.

The placement of RICH1 and RICH2 is designed to match the polar angle distribution of the incident particles. Low momentum particles are bent out of the detector acceptance by LHCb's magnetic field, therefore RICH1 is located upstream of the magnet. Higher momentum particles retain polar angles closer to the beam axis, allowing RICH2 to be located further downstream. Both RICH detectors have their radiator material and spherical mirrors located within the acceptance of LHCb. Six millimeter thick, flat borosilicate glass mirrors are placed outside the acceptance and reflect the Cherenkov light to Hybrid Photon Detectors (HPD). This step is needed to enable the HPDs to be mounted in a region with a magnetic field below 3 mT, while minimising the amount of material within the acceptance.

RICH1 is located between the VELO and TT and uses 2 mm thick Aluminium coated composite carbon spherical mirrors to limit the length of material seen by traversing particles to about 0.07 radiation lengths (X_0). RICH2 uses Aluminium coated borosilicate glass spherical mirrors and offers 0.124 X_0 to traversing particles. It is located between the last T station and the first Muon station, where the material budget is more lenient. It is also a larger detector than RICH1, in order to contain the Cherenkov light emitted by lower refractive index CF_4 radiator. Schematics of the RICH detectors are shown in figure 3.13.

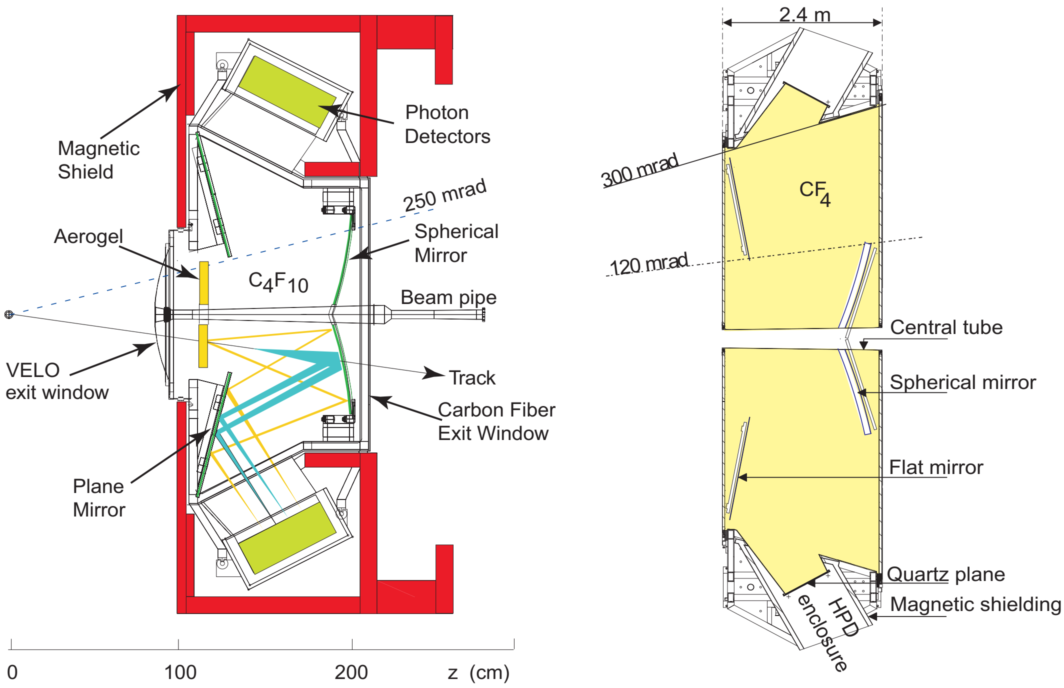

Figure 3.13: *Cross-sections of RICH1* ***(left)*** *and RICH2* ***(right)****, showing their radiators, mirrors and HPD arrays.*

3.4.2 Calorimeter

Hadrons, electrons and photons are detected and distinguished from each other by the calorimeter system. The calorimeters measure the energy of the impinging particles and supply the transverse component to the trigger. Neutral particles are detected with sufficient precision to enable reconstruction of B-decay channels containing a prompt photon or π^0.

LHCb's calorimeter system [54, 63] is formed by the Scintillating Pad Detector (SPD), the Pre-Shower (PS) detector, the Electromagnetic CALorimeter (ECAL) and the Hadronic CALorimeter (HCAL). These are sampling calorimeters, consisting of alternating layers of absorber and detector materials as shown in figure 3.14. The scintillation light, produced in the detection layers, is transported to photomultiplier tubes (PMTs) through wavelength-shifting fibres. This light is a measure of the amount of energy in the shower, therefore detecting the full energy requires the shower to be contained within the calorimeters.

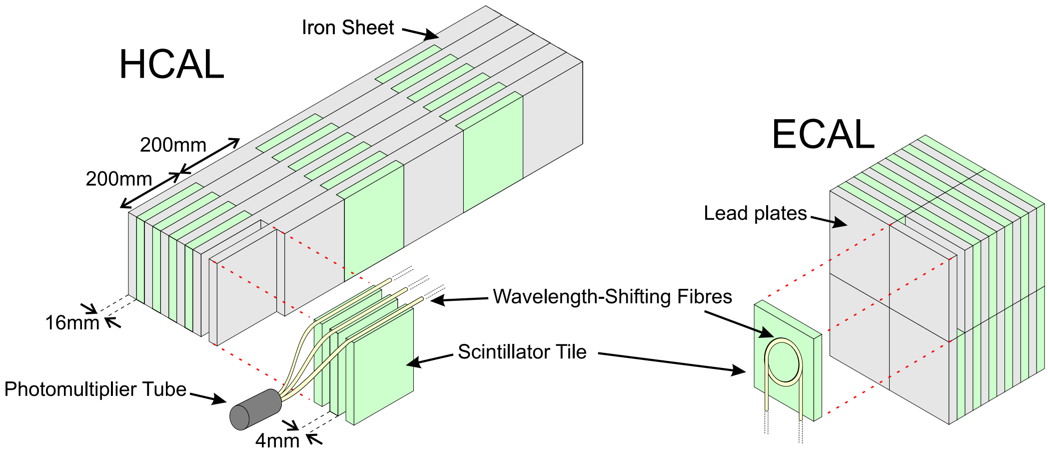

Figure 3.14: *The layers of absorber and scintillator material of the ECAL and HCAL, including the wavelength shifting fibres which transport the scintillation light to the PMTs.*

The hit density varying by two orders of magnitude over the detector surface motivates the segmentation of the calorimeters in the *x*-*y* plane. The SPD, PS and ECAL consist of three regions with different segmentations. In the innermost region, the cell size is close to the Molière radius, so that most of the energy of an isolated shower is contained within a quartet of cells. The other sizes have been optimised with a total channel number of 6000 as the main criterium. This leads to segmentation in square cells with sides measuring 40.4 mm, 60.6 mm and 121.2 mm for the ECAL and projectively smaller sizes for the SPD and PS. The hadron calorimeter requires less segmentation and consists of two regions, with cells being 131.3 mm and 262.6 mm long on either side.

The SPD is located closest to the interaction region and consists of a layer of 15 mm thick polystyrene scintillating tiles, an equivalent of 2 X_0. Charged particles will ionise the material, after which light is emitted, while neutral particles do not. This enables the SPD to distinguish between impinging electrons and photons, as a higher number of photons is detected in case of a passing electron. A lead wall of 2.5 X_0 thickness separates the SPD from the PS. The PS is made up of a 15 mm thick scintillator layer. It is designed to separate electrons from charged pions, by assuming that only the former will shower in the lead wall. Located after the PS, the ECAL consists of alternating layers of 4 mm thick scintillator material and 2 mm thick lead plates. Wavelength-shifting fibres pass through in a shashlik pattern to transport the scintillation light to the photon detectors. In total this offers 25 X_0 to fully contain high energy electromagnetic showers. Furthest downstream is the HCAL, which consists of 16 mm thick lead plates, alternated with 2 mm thick scintillator plates, which adds up to 5.6 X_0 [64].

3.4.3 Muon detector

The detection of muons by the muon system [54, 65] is required for a multitude of tasks. Many benchmark *CP* violating channels have muons in their final states, for example the two gold-plated decays: $B_d^0 \rightarrow J/\psi(\mu^+\mu^-)K_s^0$ and $B_s^0 \rightarrow J/\psi(\mu^+\mu^-)\phi$. Muons from semileptonic *B*-meson decays are also used to identify the initial state flavour of the companion *B* hadron. High p_T muons are searched for in part of the L0 trigger, as described in 3.5.1. Muons are also involved in the high-level software trigger decisions 3.5.2.

The muon system consists of five stations, covering an acceptance ranging from 20 to 306 mrad in *x*-*z* and 16 to 258 mrad in *y*-*z*, of which a side view is shown in figure 3.15. One station is located in front of the calorimeters and four behind the calorimeters. This layout provides sufficient lever arm to estimate the transverse momentum of muons for the trigger. The first and second stations are separated from each other by the calorimeters, and the other stations by 80 cm thick iron shields. These are used to attenuate hadrons, electrons and photons and effectively select muons with a momentum over 6 GeV.

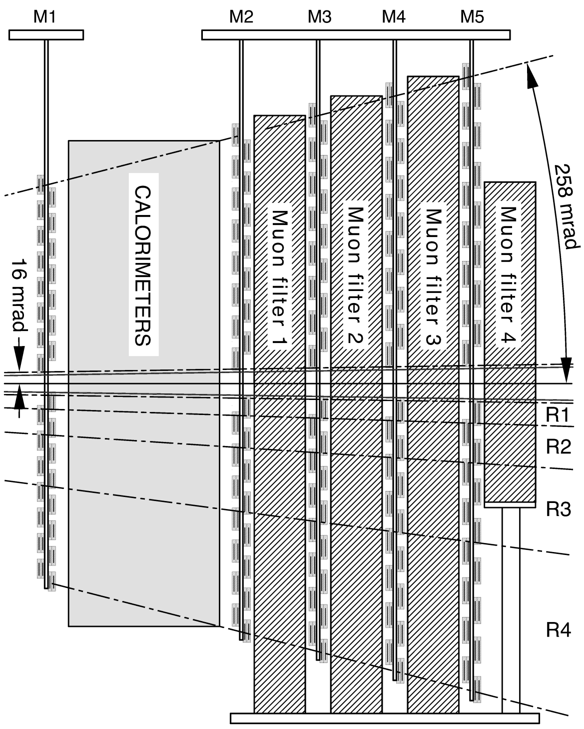

Figure 3.15: *Side view of the muon system (y-z plane), showing the locations of the muon chambers and filters.*

The stations consist of Multi Wire Proportional Chambers (MWPC) and Gas Electron Multiplier (GEM) detectors. Their use and granularity are dictated by the particle flux [66] as a function of the radial distance from the beam axis. The efficiency, time resolution, rate capability and ageing characteristics make MWPCs suitable for all but the innermost region of M1, where triple-GEM detectors [67] are used. In total four different pad granularities are used, with the x size dictated by the transverse momentum resolution needed by the trigger and the y size by the requirement to reject background muons which do not originate from the interaction region. Stations M1 to M3 have a high spatial resolution along the bending axis and are optimised for muon track reconstruction and for p_T estimation, while stations M4 to M5 are foremost intended for muon identification.

The muon trigger requires all five stations to detect the muon before accepting it as a candidate. A trigger efficiency of 95% can be achieved if the single-station efficiency reaches 99%. This efficiency is obtained by stacking detectors within each station and selecting the logical OR of overlapping detectors. Station M1, in front of the calorimeter, uses two layers, in order to minimise the amount of material in front of the calorimeters. The other four stations use four layers each.

A total of 1368 MWPCs are part of the LHCb muon system. They have a 5 mm wide gas gap in which gold-plated tungsten wires are positioned at 2 mm intervals, resulting in a time resolution of 5 ns. A gas mixture of $Ar/CO_2/CF_4$ together with a voltage of 2600 to 2700 V results in a double-gap efficiency of 95%.

The GEM detectors are suited to deal with the expected 500 kHz cm^{-2} particle flux in the innermost section of station M1. A total of 24 GEMs are used to cover this region with a double layer. A GEM consists of three perforated copper-coated Kapton foils inside a gas volume, interspaced by approximately a millimeter and bounded by an anode and cathode plane. The ionisation electrons, produced in the drift gap between the cathode and the first GEM foil, are attracted by electric fields through the three GEM foils where they are multiplied. After the last foil, the charge is collected on lateral and transverse cathode strips. An $Ar/CO_2/CF_4$ gas mixture allows to achieve a time resolution better than 3 ns at an efficiency of 96%.

3.5 Trigger

Operation of the LHCb detector is planned to take place at a nominal luminosity of $2 \cdot 10^{32}$ cm^{-2}s^{-1}. The resulting inelastic proton-proton collision frequency of 12 MHz is dominated by single interactions per bunch crossing as seen in figure 3.3. These occur at 9 MHz, leaving the other 3 MHz to multiple interaction collisions. This run scenario results in sub-detector occupancies in the range 1–10%. At a $b\bar{b}$ production cross-section of 500 μb, the creation rate of B events is of order 100 kHz, of which about 15% are contained within the acceptance of LHCb.

The LHC bunch-crossing frequency is 40 MHz, which is reduced to an event rate of 2 kHz by the trigger system [68] for storage and subsequent offline analysis. Two trigger stages are used to achieve this goal: the hardware level-0 (L0) and software High Level Trigger (HLT). The split into two parts significantly decreases the required buffer size of the sub-detector readout electronics. L0 is constructed from custom designed electronics and operates at 40 MHz, synchronous with the LHC machine clock. It is designed to reduce the event rate to 1 MHz. The HLT is formed by algorithms running on a computer farm, which processes the events passing the L0 trigger to obtain the final 2 kHz output rate. The flow of events through the trigger stages is shown in figure 3.16 and detailed in the next two subsections.

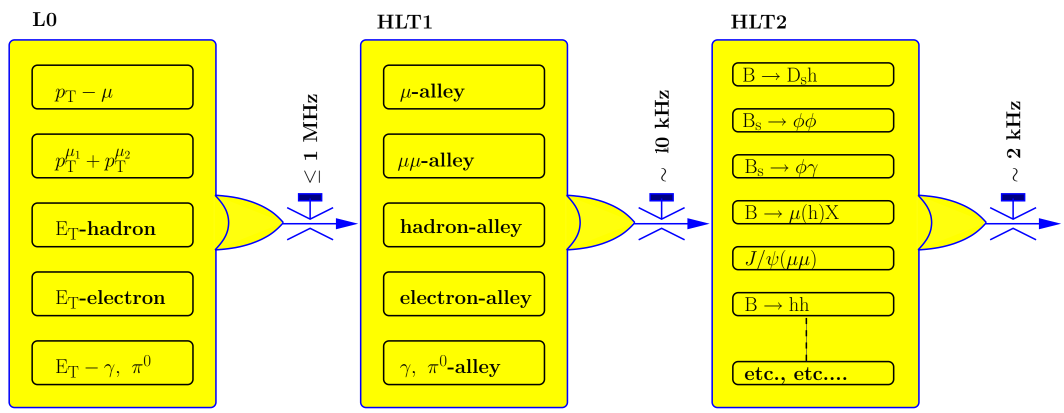

Figure 3.16: *Flow-diagram of the event processing structure of the L0, HLT1 and HLT2 triggers. The aspects used for the selection and the various alleys in which they are processed are shown, together with the event rate after each trigger.*

3.5.1 L0 trigger

The L0 trigger serves to reduce the 40 MHz bunch crossing frequency to 1 MHz, at which rate the whole detector can be read out to yield full information on an observed event. It bases its decision on the input of three component triggers: the pile-up system, the L0 calorimeter trigger and the L0 muon trigger. At a fixed latency of 4 µs, originating from the 160 event capacity of the front-end electronics buffer, the L0 trigger decision is made.

The pile-up system uses four VELO R-type sensors to measure the position of the primary vertices to within 3 mm. A backward moving particle, which crosses both layers of sensors, can leave two hits. For each R octant, all such pairs of hits are connected by a straight line pointing to the beam axis. The z-coordinates at which these cross are entered into a binned histogram. The highest peak corresponds to the primary vertex and a possible second peak is associated to a secondary vertex. If the height of this second peak exceeds a cut value, the event is judged to contain multiple interactions and is vetoed against.

The decay products of B mesons are on average part of the particles from the upper region of the produced E_T spectrum. Electrons, γ's, π^0's and hadrons from this E_T region are identified by the calorimeter trigger. To this end, groups of four neighbouring cells have their E_T summed and the highest combination is selected. The minimum E_T required for these combinations is 2.6 GeV for electrons, 2.3 GeV for photons and 3.5 GeV for hadrons. A couple of checks are made: first, the total

E_T of the HCAL must exceed 5 GeV or the event is rejected as non-reconstructible or a halo muon event; second, the number of hit SPD cells is used as a measure for the track multiplicity, allowing a maximum of 280 hits per event.

The muon trigger [69] uses stand-alone muon track reconstruction software, which offers a mean transverse momentum resolution of 20%. All five stations are required to be hit and the resulting muon candidate is to point towards the interaction region. Per quadrant the highest p_T candidates are selected for the L0 trigger, requiring at least a p_T of 1.3 GeV or a combined p_T of 1.5 GeV for the two muons with the highest transverse momenta.

The results of the individual trigger components are collected by the L0 Decision unit, on which it bases the trigger decision. About 15% of the Level-0 events are selected by multiple triggers. All L0 calorimeter clusters and muon tracks above their respective thresholds are passed to the HLT as part of the L0 trigger information, and are referred to as L0 objects.

3.5.2 HLT

The HLT is a computer program which runs on a cluster of computing units comprising the Event Filter Farm (EFF). It selects the events of most interest to the physics analyses. The HLT consists of two parts, being HLT1 and HLT2.

The L0 confirmation or HLT1 algorithm distributes the L0 objects by type into so-called alleys, as shown in figure 3.16. An alley consists of a dedicated algorithm, which progressively adds hits from the tracking stations to the L0 object. Cuts on the transverse momentum and impact parameter are used at each step to see whether the candidate is to be rejected. Alleys dealing with a photon or π^0 L0 object require the absence of a charged particle associated to these objects. Other alleys search for additional particles apart from the L0 candidate in order to improve the likelihood estimate of a B decay.

HLT1 reduces the event rate to around 10 kHz, on which the HLT2 is able to perform track reconstruction. The HLT2 tracks are found by pattern recognition as in the offline track reconstruction, see chapter 5. A subset of these tracks is selected by applying loose cuts on their momenta and impact parameters. Composite particles are constructed from these tracks, which are used in all selections in order to avoid recreation of existing final states. The selections are both inclusive, aiming for generic B decays and for resonances, and exclusive, designed to provide the highest possible efficiency on specific B-decay channels. Events which pass either selection are written to disk. The output bandwidth is resolved into:

- Exclusive B-hadron decays ($\sim$ 200 Hz) : The main events of interest for physics analysis, selected using essentially the final offline selection with loosened-up selection criteria.

- Inclusive $b \to \mu X$ ($\sim$ 900 Hz) : An unbiased sample of B hadrons, selected on the presence of a high p_T, large impact parameter muon, useful for studying the trigger and flavour tagging performance.

- Dimuon ($\sim$ 600 Hz) : J/ψ decays can be reconstructed from two muons without applying geometrical selection criteria, allowing study of the detector proper time resolution.

- D* ($\sim$ 300 Hz) : $D^{*+} \rightarrow D^0\pi^+$ decays can be used for an unbiased calibration of the particle identification performance for pions and kaons.

Chapter 4

Simulation

Between submission of the letter of intent [40] and the currently expected date of recording the first p-p collisions, there is a time span of 14 years. This time is used to design and construct a detector and to write the required software for online and offline data processing. Both hardware and software development offer design issues, for which the optimal choices are not transparent. At this stage, it becomes useful to be able to calculate the effects of a particular solution on the relevant performance parameters. Monte Carlo simulation software fulfils this task for the LHCb experiment by simulating collisions in the LHC machine and the detector response to such events.

In effect, event simulation offers a preview of what actual data can look like. For example, the predicted distribution of the polar angle between b and $\bar{b}$ quarks of a $b\bar{b}$ pair, as shown in figure 4.1, leads to the choice of a wedge-shaped detector acceptance. The simulated data is processed for the refinement of the sub-detector designs, for example by evaluating the hit occupancy for a given detector technology or by demonstrating the impact of material on the physics performance [55, 70]. It also allows for developing trigger, reconstruction, and physics analysis algorithms. This facilitates the prediction of signal yields, from which the sensitivity of LHCb to B-physics parameters is estimated.

The software used by the LHCb collaboration for event simulation and reconstruction, is introduced in section 4.1. Using this software, event samples are generated as stated in section 4.2. For the study of track reconstruction, understanding the impact of the magnetic field and detector material on the path of a particle is important. Both the theory and the approach of the simulation package Geant4 are detailed in sections 4.3, 4.4 and 4.5. Finally, the amount of material in the tracking region of the detector is shown in section 4.6.

4.1 Software chain

Simulation, reconstruction and analysis software for LHCb is built to function on top of the Gaudi software framework [71]. Gaudi provides the common infrastructure and functionality, built out of generic, decoupled components to facilitate maintenance and increase its lifetime. This approach in addition allows Gaudi to be

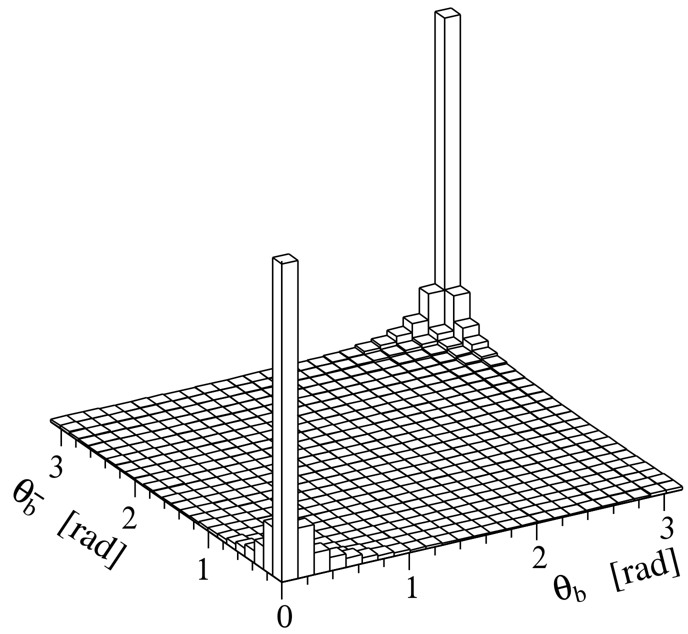

Figure 4.1: *The polar angle distribution of the b and $\bar{b}$ quarks of a $b\bar{b}$ pair, obtained from simulated p-p collisions at $\sqrt{s}$ =14 TeV [43].*

used by other experiments such as ATLAS, HARP and GLAST.

The simulation of *p-p* collisions and the propagation and decay of the ensuing particles and radiation is managed by the Gauss package [72]. It delegates these tasks to the Pythia [73] and EvtGen [74] generator libraries and the Geant4 [75] software toolbox. Pythia generates the collisions and decays the unstable particles. EvtGen specialises in the decay of B hadrons, a task which it takes over from Pythia. Geant4 simulates the physics of particles passing through the detector material and the magnetic field.

The locations at which the particles and radiation traverse the sensitive detector components are stored as hits. The detector response to those hits is computed by Boole [76]. Boole generates front-end readout signals for each of the hits and determines the level-0 trigger response to those signals. The detector output is called raw data, and in the simulation it is of identical format to actual data.

This raw data is input to the particle reconstruction software of Brunel [77], which is detailed in chapters 5 and 6. The reconstructed particle paths are made available as tracks to the analysis software packages DaVinci [78], Bender [79] and LoKi [80]. These assign particle type hypotheses to each track and reconstruct the event from which they originate, using the additional information provided by the calorimeters, and the RICH and muon detectors.

A visualisation of particles in the LHCb detector can be made with the use of Panoramix [81], of which two examples are shown in figure 4.2. It allows to inspect details like individual detector components, hit strips and wires, and tracks, which is helpful for understanding the behaviour of and identifying possible errors in the reconstruction and analysis software.

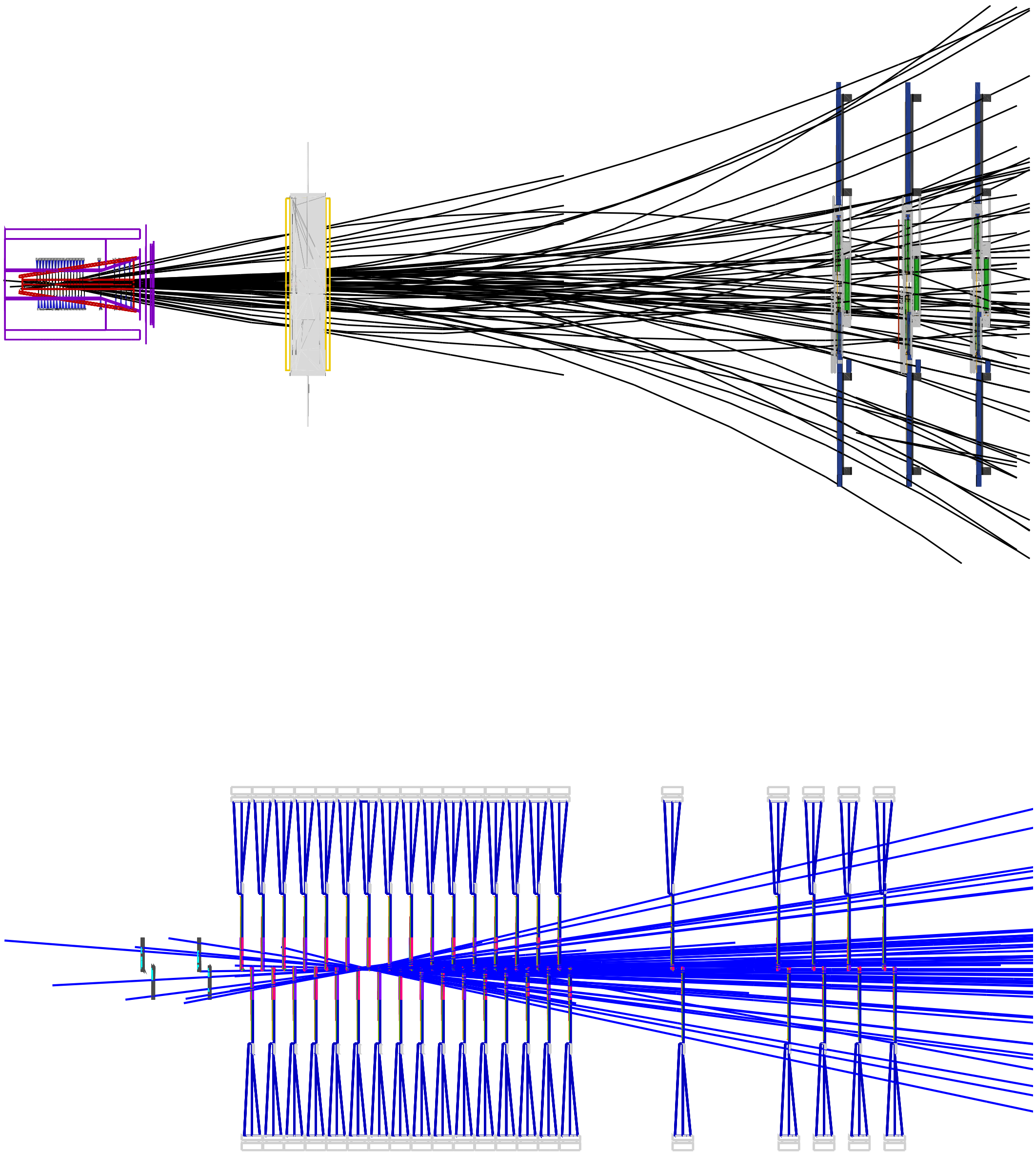

Figure 4.2: ***(top)*** *A top view of the reconstructed tracks of charged particles passing through the tracking sub-detectors.* ***(bottom)*** *A zoomed-in view of the event, showing the components of the VELO detector and the reconstructed tracks.*

4.2 Event sample

A sample of 25000 $B_s^0 \to D_s^- \pi^+$ [1] events at a luminosity of 2 10^{32} cm^{-2}s^{-1} is generated for tracking studies in the course of this thesis. The Monte-Carlo (MC) information of these events is used in the evaluation of the track reconstruction performance, as done in section 5.4 and in chapter 7. For the generation, the latest versions of the software packages that are compatible with the DC06 format are used

DC06 refers to the 2006 Data Challenge, which serves as a performance test of the complete software chain. In the course of DC06, a selection of signal (in this thesis events containing the decay $B_s^0 \to D_s^- \pi^+$), $b\bar{b}$ inclusive and minimum bias events were generated. To obtain signal events, the appropriate B-hadron is forced to decay into a user-specified channel by EvtGen. It takes into account the mixing of neutral B mesons as well as possible time-dependent CP asymmetries. In case a B hadron is allowed to decay generically within the detector acceptance, $b\bar{b}$ inclusive events are produced. These events constitute background in a physics analysis of the signal decay channel. Another source of background is formed by minimum bias events, which are generated by randomly sampling events.

The production envelope of primary vertices is inspected for the generated event sample. It is defined as the widths of Gaussian fits to the x, y and z-coordinate distributions of the primary vertices. According to the LHC beam specifications, these are 70.9 µm in x and y [42]. The width in z is expected to be 53 mm [54]. From the data sample, in x and y these widths σ_x and σ_y are both found to be 70.0 ± 0.3 µm. Along the z-axis, the width σ_z equals 49.6 ± 0.2 mm. The coordinate distributions are shown in the plots of figure 4.3.

The simulation produces raw data from which hits in the silicon detectors and in the OT are made. Silicon detector hits contain the hit strips and the total charge that they have collected. OT hits contain the hit wire, the TDC time and the TDC time corrected for the time at which the event took place [58]. The hits are created by sub-detector specific algorithms. They form the input to the pattern recognition, which combines them into tracks as described in chapter 5. The MC equivalent of hits are the MC hits. They contain the entry and exit points of the particle in the material layer, the amount of lost energy and the momentum of the particle at the entry point. These MC hits are used in the determination of performance parameters as detailed in chapter 7.

4.3 Magnetic field

Electrically charged particles moving through a magnetic field are bent away from their initial direction. This is exploited to determine the sign of their charge, as positively charged particles bend in the opposite direction of negatively charged particles. Knowing the amount of deviation allows for the momentum to be estimated. As the bending is dependent on the strength of the traversed magnetic field,

[1] The charge conjugate mode is implied unless stated otherwise.

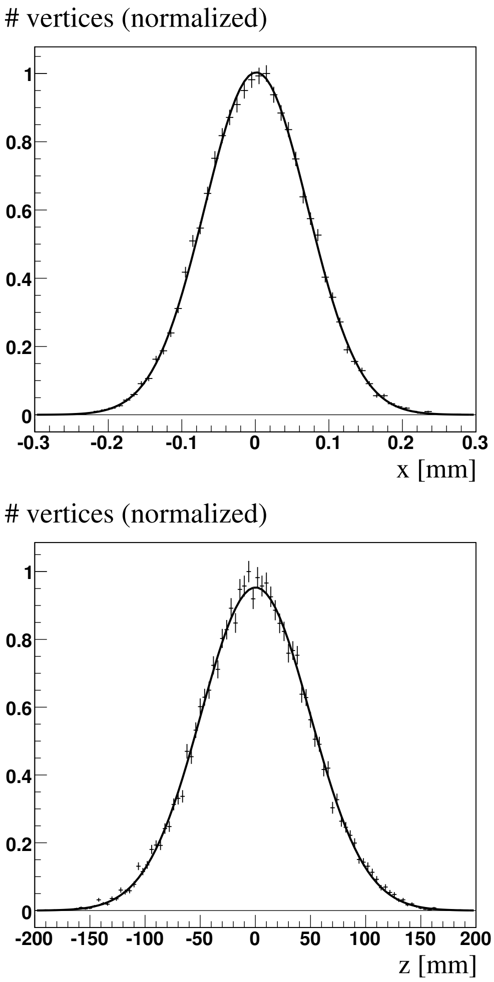

Figure 4.3: *The x, y and z coordinate distributions of the primary vertices, fitted by Gaussian functions.*

the field of LHCb needs to be known. In order to achieve a momentum resolution of 0.5%, the required relative accuracy of a field integral is calculated to be of order 10^{-4} [54].

A field map with a granularity of $8 \times 8 \times 10$ cm^3 has been measured in situ in 2005. The measurements were done with the use of an array of Hall probes. The array consists of two vertical $8{\times}8$ cm^2 planes, separated by 64 mm, on which the 60 probes are mounted as orthogonal triplets to form cubes on a grid. Each Hall probe is calibrated to a relative precision of 10^{-4} T [82]. The field integral within the tracking volume is measured with a relative precision of $4 \cdot 10^{-4}$ T.

As a part of the design procedure of the magnet, a finite element calculation of the field corresponding to the magnet's technical drawing is performed in TOSCA [56]. The TOSCA model works with a ten centimetre grid in all three dimensions, resulting in ~180000 field strength values per component. An overall agreement to 1% between the values calculated by this simulation and the measured values, which are measured with a relative precision of 10^{-4} T, is observed [83]. The VELO-RICH1 region forms an exception with a 3.5% discrepancy, ascribed to metal reinforcements of the hall [54]. A functional description of the magnetic field by means of Chebyshev polynomials was developed for use by the reconstruction software [84].

Geant4 is able to simulate both homogeneous and inhomogeneous magnetic fields. Depending on the field configuration and the desired accuracy, a particle is propagated through the field by solving the equation of motion (see section 6.3.1) either analytically or numerically. For the inhomogeneous magnetic field of LHCb, the equations of motion are solved using a fifth order Runge-Kutta method, the same as used in the track reconstruction as described in subsection 6.3.4. In figure 4.4 the principal component of the magnetic field is shown as a function of the z-coordinate along the beam line. It shows an inhomogeneous profile, peaking inside the magnet. The x and z components are zero along the beam line and their profiles at 197 mrad can be found in [56].

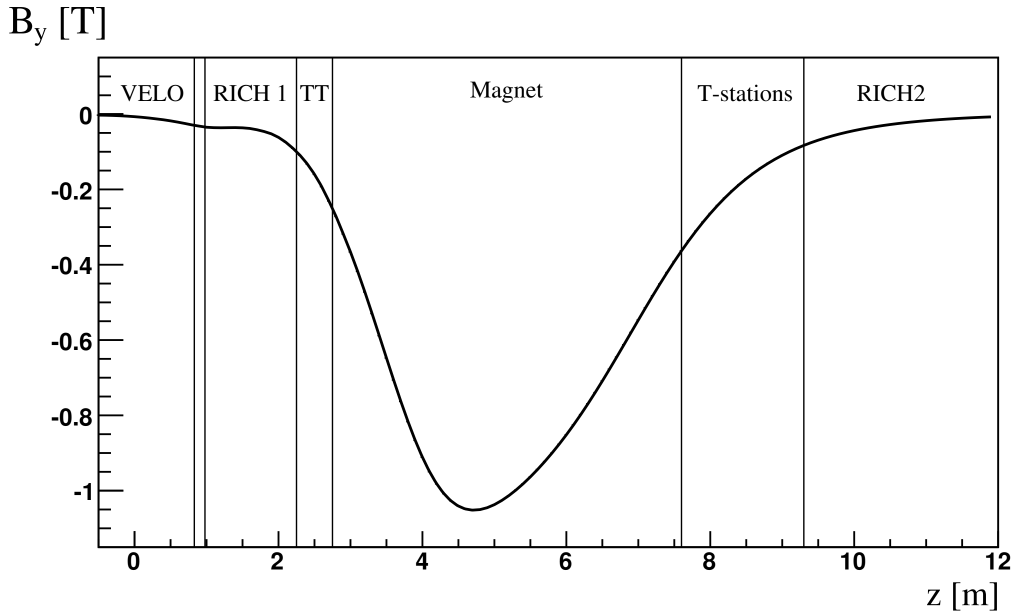

Figure 4.4: *The y-component of the magnetic field, determined along the z-axis at* $x = y = 0$.

The track reconstruction uses a linear, a parabolic and a Runge-Kutta solution of the equations of motion, as described in section 6.3. Depending on the field strength, the distance travelled through the field and the required accuracy, the pattern recognition and track fit strategies select the appropriate one from these solutions. In table 4.1, the integrated magnetic field is listed for various regions of the detector, as encountered by particles moving along the beam line. Using a two GeV particle, the differences in the calculated x-coordinate between the linear or parabolic solutions and the Runge-Kutta solution is calculated. The results show increased discrepancies both when longer distances are involved and as the encountered field integral increases. Based on these numbers, for the VELO (subsection 5.2.1) and T-station (subsection 5.2.2) seeding algorithms, it is concluded that respectively the linear and the parabolic solutions offer sufficient accuracy to determine which hits belong to which particle. The track fit uses the parabolic and Runge-Kutta solutions, see section 6.3.

Table 4.1: *The field integral for particles traversing the listed regions, starting at $x = y = 0$. For 2 GeV charged particles, the difference in final x-coordinates between the linear method and the Runge-Kutta method are given in the one but last column, and between the parabolic and RK methods in the last column. The uncertainty on these numbers is smaller than the last presented digit.*

region	z range [mm]	$\int Bdl$ [Tm]	$\lvert\Delta x\rvert$ (lin-RK) [mm]	$\lvert\Delta x\rvert$ (par-RK) [mm]
VELO	0 – 830	0.0136	0.65	0.14
VELO-RICH1	830 – 978	0.0048	0.05	0.001
RICH1	978 – 2250	0.0608	4.80	0.13
TT	2250 – 2750	0.0821	2.63	0.37
Magnet	2750 – 7600	3.6727	1493	299
T stations	7600 – 9300	0.3316	52	13

4.4 Multiple scattering

A charged particle traversing the material of the detector can scatter in the Coulomb fields of the nuclei. Given the relative mass difference between the particle and a nucleus, this will be an elastic scattering. Such a scatter changes only the particle's direction, not the absolute value of its momentum. The material layers encountered by a particle in LHCb are thick enough to on average result in several such deflections. Their combined effect on a particle's path is referred to as multiple scattering.

The path of a charged particle through matter is given by a transport equation. It is this equation that needs to be solved by the algorithms of the simulation software. A classification of solution strategies is made, resulting in the detailed, condensed and mixed categories. Algorithms of the detailed kind treat each interaction of a particle with material individually, amounting to an exact solution of the transport equation, modulo inherent statistical uncertainties. The detailed approach has the benefit of being accurate, but is limited by practical considerations to a few hundred interactions per particle [75]. This limits its use to scenarios involving thin foils, low density gasses and particles with sufficiently low kinetic energies.

Higher energies and larger number of interactions can be handled by the condensed strategy. In that scenario, the interactions are combined into a global effect on the particle's path. This effect is calculated at a number of points along the path, each pair of points enclosing multiple interactions, and consists of a displacement from the unperturbed trajectory, a change in direction, and loss of kinetic energy, see also section 4.5. Several models are available to calculate these quantities. They are inexact by construction, limiting their accuracy by the approximations they are based on, and susceptible to the step size between two points. Mixed models combine both approaches, treating hard collisions in detail and the effect of soft interactions globally. This is computationally possible as the fraction of hard collisions is small.

Geant4 implements a condensed approach [85], based on the multiple scattering theory of Lewis [86]. Lewis theory contains formulae for the computation of the first moments of the displacement distribution at the end of a step. This in contrast to the theory of Molière [87] and the theory of Goudsmit and Saunderson [88], which are limited to describing the angular distribution. Custom algorithms define the angular and spatial distributions, matching it to the moments given by the Lewis theory. It is this approximation, made for the spatial distribution, which introduces the largest uncertainties in the determination of the effect of multiple scattering by Geant4. The uncertainties scale with the inverse of the step size, requiring a balance between the computing time and accuracy to be determined.

A particle's path is segmented into steps, which have a shortest unperturbed geometrical path length s. This takes into account the effect of a magnetic field, but not the interactions with the material. Therefore the true path length l is longer. The average geometrical path length is related to the true path length as [85]:

$$< s >= \lambda_1 \left[1 - e^{-l/\lambda_1}\right] \quad [\mathrm{mm}] . \tag{4.1}$$

In this equation, λ_1 stands for the first transport mean free path of the material the particle traverses. A particle travels unperturbed for an average distance λ between collisions. The expression for λ can be expanded in a Legendre series, whose terms are the transport mean free paths. Its first and second terms completely determine the properties of multiple scattering in Geant4. The equations for λ_1 and λ_2, using the atomic density N, the change in angle χ, the solid angle Ω, and the elastic scattering differential cross section, are [89]:

$$1/\lambda_1 = 2\pi N \int_{-1}^{1} (1 - \cos\chi) \frac{d\sigma(\chi)}{d\Omega} d(\cos\chi) \quad [\mathrm{mm}^{-1}] , \tag{4.2}$$

$$1/\lambda_2 = 3\pi N \int_{-1}^{1} (1 - \cos^2\chi) \frac{d\sigma(\chi)}{d\Omega} d(\cos\chi) \quad [\mathrm{mm}^{-1}] . \tag{4.3}$$

The path of a particle through material is described by a diffusion equation [89]. Solving this equation results in an expression for the distribution of the polar angle θ at the end of a step:

$$F(\theta, l) = \sum_{i=0}^{\infty} \frac{2i+1}{4\pi} e^{-l/\lambda_i} P_i(\cos\theta) , \tag{4.4}$$

where λ_i are the mean free paths and P_i are Legendre polynomials.

Using the orthogonality of the Legendre polynomials, the average cosine value of the polar scattering angle with respect to the initial direction is found to be:

$$< \cos\theta >= e^{-l/\lambda_1} . \tag{4.5}$$

The variance of $\cos\theta$ is determined by the expression:

$$\sigma^2 = \frac{1}{3} + \frac{2}{3} e^{-2l/\lambda_2} - e^{-2l/\lambda_1} . \tag{4.6}$$

Geant4 implements a model function for the angular distribution of equation (4.4). It is chosen such as to reproduce the moments as defined by equations (4.5) and (4.6).

The RMS is given by the modified Highland-Lynch-Dahl formula for the polar angle [90, 91]. This formula defines the width θ_0 of the approximate Gaussian projected angle distribution as:

$$\theta_0 = \frac{13.6\text{MeV}}{\beta c p} z_{ch} \sqrt{\frac{l}{X_0}} \left[1 + 0.105 \ln\left(\frac{l}{X_0}\right) + 0.0035 \left(\ln\left(\frac{l}{X_0}\right)\right)^2 \right]^{\frac{1}{2}} \cdot \left(1 - \frac{0.24}{Z(Z+1)}\right), \quad (4.7)$$

where βc is the velocity, p the momentum, z_{ch} the particle's charge number, X_0 the radiation length and Z the atomic number. The last term is determined empirically from high energy proton scattering observations [92].

The geometrical displacement at the end of a step is calculated in [93], from which the result for the mean displacement is used. Assuming the particle to initially move parallel to the z-axis, the mean lateral displacement squared at the end of a step is given by:

$$< x^2 + y^2 >= \frac{4\lambda_1^2}{3} \left[-1 + \frac{l - \lambda_2}{\lambda_1} + \frac{\lambda_1}{\lambda_1 - \lambda_2} e^{-l/\lambda_1} - \frac{\lambda_2^2}{\lambda_1^2 - \lambda_1 \lambda_2} e^{-l/\lambda_2} \right] \quad [\text{mm}^2]\,. \quad (4.8)$$

The lateral displacement is correlated to the polar angle θ. Using $\hat{x}$ and $\hat{y}$ for the x and y components of the unit direction vector, this correlation is formulated as:

$$< x\hat{x} + y\hat{y} >= \frac{2\lambda_1}{3} \left[1 - \frac{\lambda_1}{\lambda_1 - \lambda_2} e^{-l/\lambda_1} + \frac{\lambda_2}{\lambda_1 - \lambda_2} e^{-l/\lambda_2} \right] \quad [\text{mm}]\,. \quad (4.9)$$

At the end of a step, Geant4 samples its model function to determine the polar angle θ of the particle. Its azimuthal angle is chosen as a random drawing from a uniform distribution, ranging from 0 to 2π. The size of the lateral displacement is given by equation (4.8), and with the polar angle θ and equation (4.9), the values of the x and y components are determined.

This approach is different from the one implemented in the track reconstruction of LHCb, as described in subsection 6.3.6. The track fit takes the average coordinate change into account as a contribution to the errors of the track parameters with which the fit describes the path of a charged particle. By increasing those errors, a hit located after the material in which multiple scattering occurred, will have a relatively larger weight in the determination of the track parameters. The hit is a measurement of the path of a charged particle, which includes the effects of multiple scattering on the track parameters. Therefore the track parameters on average are changed, from the values they would have in absence of multiple scattering, consistently with the average multiple scattering induced coordinate change.

4.5 Energy loss

A charged particle traversing material loses kinetic energy by means of ionisation, atomic excitation and bremsstrahlung. Bremsstrahlung is the radiation which a charged particle emits when deflected by the electromagnetic field of a nucleus, and the amount of energy is inversely proportional to the particle's mass. This is the dominant process of energy loss for high-energy electrons. The average energy loss due to emission of bremsstrahlung by an electron in a screened Coulomb field is formulated by Bethe and Heitler as [94]:

$$-\frac{dE}{dx} = \frac{E}{X/X_0} \quad [\mathrm{MeV\,cm^{-1}}]\,, \tag{4.10}$$

where E is the electron's initial energy, x is the length of traversed material and X/X_0 is the thickness of encountered material in radiation lengths. The radiation length X_0 is the mean distance over which an electron's energy decreases to $1/e$ of its initial value. The value of the radiation length for several materials is calculated [95] and to within a 2.5% accuracy is given by [96]:

$$X_0 = \frac{716.4\,A}{Z(Z+1)\ln\left(287/\sqrt{Z}\right)} \quad [\mathrm{g\,cm^{-2}}]\,, \tag{4.11}$$

in which A and Z are the atomic mass and atomic number of the material.

Ionisation and excitation result in an average energy loss of a particle or stopping power as given by the Bethe-Bloch equation [4]:

$$-\frac{dE}{dx} = 4\pi N_A r_e^2 m_e c^2 z^2 \frac{Z}{A}\frac{1}{\beta^2}\left[\frac{1}{2}\ln\left(\frac{2m_e c^2\beta^2 T_{\max}}{I^2}\right) - \beta^2 - \frac{\delta(\beta\gamma)}{2}\right] \quad [\mathrm{MeV\,cm^{-1}}]\,, \tag{4.12}$$

using Avogadro's number N_A, the classical electron radius r_e, the electron mass m_e, the particle's electric charge z, the maximum kinetic energy that can be transferred to a free electron in a single collision $T_{\max}$, and the density effect correction $\delta(\beta\gamma)$.

The mean excitation potential I of a material is approximated by Bloch as:

$$I = 10\,Z\,. \tag{4.13}$$

In the typical $\beta\gamma$ range of high-energy physics experiments, the energy loss distribution versus $\beta\gamma$ shows a minimum [4]. The particles in this region are referred to as minimum ionising particles or MIPs.

Geant4 simulates a number of processes, which determine the reduction of kinetic energy of a charged particle as it moves through material [85]. The range of simulated energy loss is divided in two at the production threshold T_c of δ-rays. Below this threshold, energy loss is described by a continuous process. Above the cut-off value, secondary particles are generated explicitly, which carry away part of the mother particle's kinetic energy.

In the region of continuous energy loss, the energy loss per step is calculated from a mean energy loss rate. This rate is determined per type of material and is dependent on the kinetic energy of the particle. However, over the length of a transportation step, the differential cross section is treated as a constant when determining the continuous energy loss. This imposes a limit on the step size of the continuous energy loss calculation, related to the desired accuracy of the simulation. The maximum step length is determined by allowing a 20% decrease in the particle's stopping range.

The mean energy loss ΔE over a step of true length l is, for losses below five percent of the particles initial kinetic energy, given by:

$$\Delta E = \frac{dE}{ds} l \quad [\mathrm{MeV}]\,. \tag{4.14}$$

The average energy loss is subsequently transformed into the actual energy loss value, taking into account energy loss fluctuations. This is done by describing the energy loss by a straggling function, with the same mean value as given by the uncorrected formula (4.14).

In some layers of material the number of interactions per step can exceed nine, in which case it is labelled a thick absorber. More specifically, the straggling function for thick absorbers is applied when the following two conditions are met:

$$\Delta E > 10 T_c \quad [\mathrm{MeV}]\,, \tag{4.15}$$

$$T_{max} \leq 2 T_c \quad [\mathrm{MeV}]\,, \tag{4.16}$$

where ΔE is the mean energy loss over a step of true length l, T_{max} is the largest amount of kinetic energy which the particle can transfer to an atomic electron and T_c is the cut-off energy above which δ-electrons are produced.

In case the criteria for a thick absorber are not met, the energy loss model of a thin absorber is used. In this model the total energy loss is decomposed into two parts; one due to excitation and the other as the result of ionisation:

$$\Delta E = \Delta E_{\mathrm{exc}} + \Delta E_{\mathrm{ion}} \quad [\mathrm{MeV}]\,. \tag{4.17}$$

The excitation energy loss is derived from a model using two energy levels for an atom. These levels involve binding energies E_1 and E_2, which are defined as [85]:

$$E_1 = e^{(2 \ln E_2 - Z \ln I)/(Z-2)} \quad [\mathrm{MeV}]\,, \tag{4.18}$$

$$E_2 = 10\, Z^2 \quad [\mathrm{MeV}]\,, \tag{4.19}$$

where I is the mean ionisation energy. Each level is involved in n_1 respectively n_2 number of collisions as drawn from Poisson distributions. Their combined effect is given as:

$$\Delta E_{\mathrm{exc}} = n_1 E_1 + n_2 E_2 \quad [\mathrm{MeV}]\,. \tag{4.20}$$

The ionisation energy loss of a particle during a step follows a distribution function which is inversely proportional to the square of the initial energy. From this function, the ionisation energy loss is found to be:

$$\Delta E_{\mathrm{ion}} = \sum_{j=1}^{n_3} \frac{10}{1 - u_j(1 - 10/T_c)} \quad [\mathrm{MeV}]\,, \tag{4.21}$$

where the summation is over the number of collisions in the step (n_3) involving ionisation and u_j is a random number between 0 and 1.

The simulation changes the energy of a particle as a correction for the energy lost in traversing a material layer. The track reconstruction calculates the average effect of energy loss on the momentum of a particle, see subsection 6.3.7. In case of electrons, due to their low mass, the error on the momentum is also increased. Compared to the simulation, the reconstruction assumes all material layers to be thick absorbers.

4.6 Detector material

The description of the LHCb detector in the software evolves as the amount, location and type of materials of its components change. For example, the VELO sensor-thickness increased from 200 to 300 μm. In addition, the implemented granularity of the description is driven by accuracy requirements of the reconstruction and analysis software. Therefore the beam-pipe supports and detector cabling are included for DC06.

The accuracy requirements for instance originate from the desired momentum resolution, which scales with the square-root of the encountered material in radiation lengths [97]. The pseudorapidity-averaged traversed thickness in radiation lengths is listed as a function of z in table 4.2. Between the vertex and the first hit, the amount of material has remained equivalent to 2.7% [98] of a radiation length, compared to pre-DC06. In contrast, the average traversed thickness in radiation lengths from the vertex to the end of the T stations (z=9300 mm), increased from 45% [55] for the re-optimised detector to 60.7% [98] at the time of DC06, mainly due to adding cables and connectors to the description.

Table 4.2: *The average thickness of material, expressed as a percentage of radiation length, encountered by particles traversing the listed regions. The uncertainty on these numbers is smaller than the last presented digit.*

region	z range [mm]	X/X_0 [%]
VELO	0 – 830	16.2
VELO-RICH1	830 – 978	6.8
RICH1	978 – 2250	9.5
TT	2250 – 2750	5.1
Magnet	2750 – 7600	5.3
T stations	7600 – 9300	17.8

As a function of the pseudorapidity η, the length of material as a number of radiation lengths X_0 that a particle encounters is shown in figure 4.5. Below η=1.89, the encountered number of radiation lengths is large due to the presence of material like the detector frames. Summing up to the end of the T stations (z=0–9300 mm), the average encountered X_0 is 30%, for the region 1.89< η <3.5. This is 45% for 3.6< η <4.3, higher on account of the interface section between the VELO vacuum tank and the beam pipe, and the cooling rods, signal cables, and connectors of the

IT [98]. The beam pipe itself manifests as a peak in X_0 at η=4.38. Towards η=5, the integrated number of radiation lengths increases as particles pass through the 10 mrad beam-pipe sections.

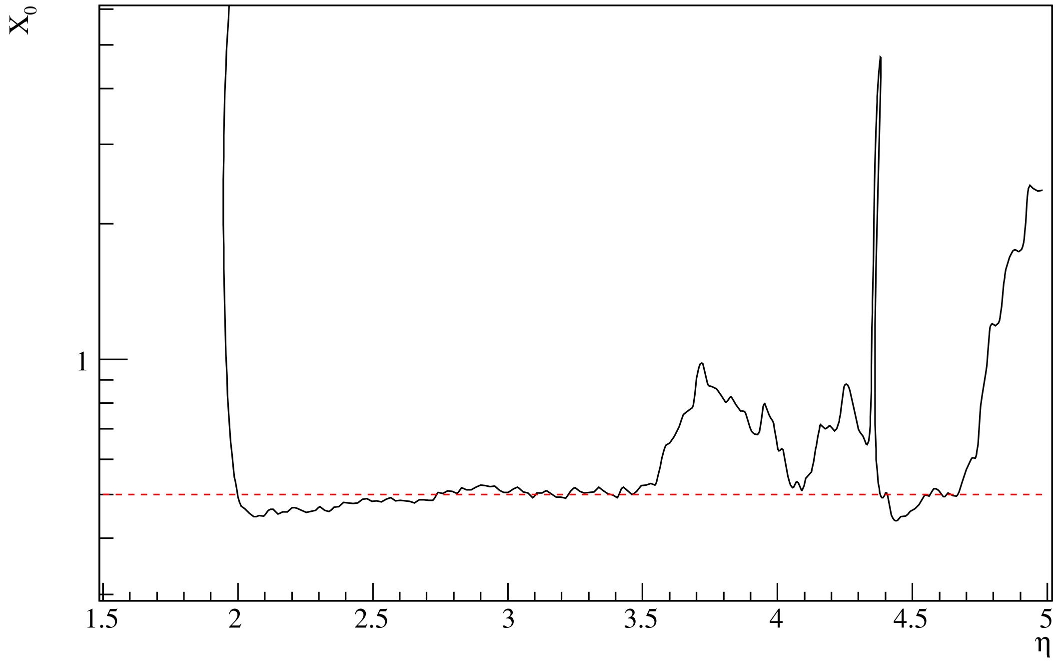

Figure 4.5: *The integrated length of material as a number of radiation lengths, encountered by particles travelling from the vertex to z=9300 mm, plotted as a function of pseudorapidity [98].*

Chapter 5

Pattern recognition

A particle's path through the LHCb spectrometer is reconstructed from the hits that it creates in the position sensitive tracking sub-detectors. These are the Velo, TT, IT and OT, which are described in sections 3.3.2– 3.3.4. The observed silicon and OT hits are either due to traversing particles or to noise. It is the purpose of the pattern recognition algorithms to determine which groups of hits belong to the individual particles. This is the first step of the track reconstruction. The second step is the fitting of the tracks, as discussed in chapter 6.

The pattern recognition identifies the groups of hits in steps. It first determines the upstream or downstream starting points in the VELO or the T stations, as described in section 5.2. These seeds are subsequently complimented by hits from the other tracking sub-detectors, see section 5.3. An identified group of hits is referred to as a track. The pattern recognition procedure can result in tracks that do not correspond to actual particles, as is described in subsection 5.4.1. Alternatively, several tracks can also represent the same particle, which is treated in subsection 5.4.2. The pattern recognition strives to find tracks at a high efficiency, which is evaluated in subsection 5.4.3. The hit content of tracks is inspected to identify which hits should be part of the track, according to the Monte-Carlo information. As the particle that the track represents is known, the purity of the hit assignment procedure can be determined as well. The hit finding efficiency and the purity of the identified hits are detailed in subsection 5.4.4.

5.1 Track and particle types

A track represents the path of a charged particle through the detector, as further discussed in chapter 6. Depending on the nature of a charged particle, it can be detected by the various tracking sub-detectors. Based on which of the sub-detectors contribute hits to a particular track, it is classified to belong to one of five categories [99]. These categories correspond to track types as illustrated in figure 5.1. The hit content of each type of track, and an impression of their role in physics analyses, are described next:

Velo tracks contain only hits of the Vertex Locator. They can travel in the backward direction, or in the forward direction at a sufficient polar angle to leave the detector before the Tracker Turicensis. The L0 trigger uses the backward Velo tracks in its determination of the interaction multiplicity, as described in subsection 3.5.1. Velo tracks can have a pseudorapidity which is lower than the region occupied by Upstream and Long tracks. This makes the uncertainty on the impact parameter of such a Velo track smaller than of the Long and Upstream tracks, allowing the primary vertex to be determined more precisely.

Upstream tracks consist of hits from both the Vertex Locator and the Tracker Turicensis. These can be low momentum particles, which are bend out of the detector acceptance in the magnet region, before they reach the T stations. They are used by RICH1 for kaon reconstruction, which allows for flavour tagging in B-meson decays.

Long tracks have hits in all tracking sub-detectors, so they traverse the entire forward tracking region. This provides them with the most accurate momentum estimate of all track types. These tracks are the dominant input for physics analyses.

Downstream tracks have hits in the Tracker Turicensis and the T stations, but not in the Vertex Locator. They are of interest when looking for long lived K_s and Λ_b particles, which decay outside of the VELO.

T tracks contain only hits of the Inner Tracker and Outer Tracker. These tracks are used for pion and kaon reconstruction in RICH2.

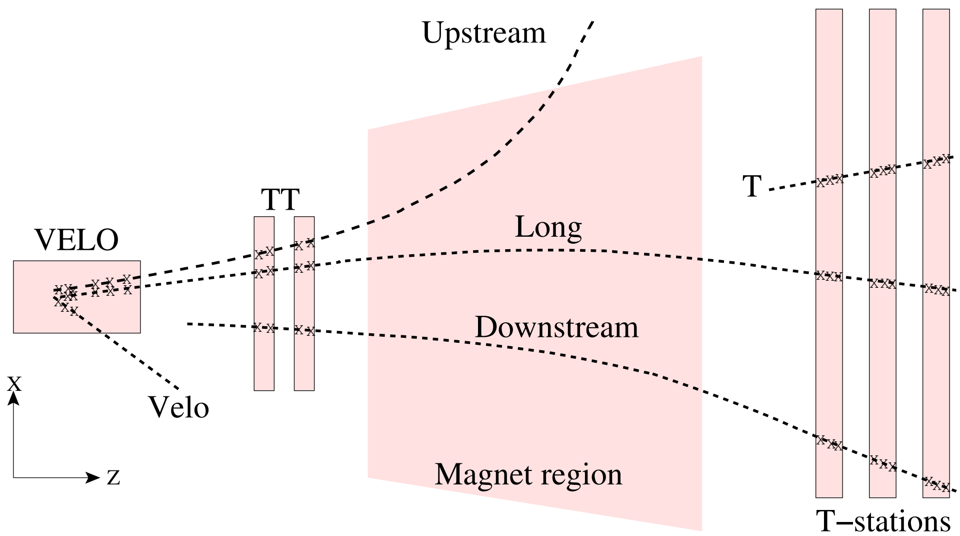

Figure 5.1: *Counting IT and OT as one sub-detector, Long tracks traverse all tracking sub-detectors. The Velo, Upstream, Downstream, and T tracks cross subsets of the tracking sub-detectors, as shown in this illustration.*

MC particles can create MC hits in the tracking sub-detectors during the simulation of an event. An MC particle can be in one of five detector acceptances, depending on the locations of its MC hits:

Velo acceptance: at least three ϕ and three R MC hits in the VELO.

Upstream acceptance: at least three ϕ and three R MC hits in the VELO, and at least one MC hit in each of the two stations of the TT.

Long acceptance: at least three ϕ and three R MC hits in the VELO, and at least one x and one stereo MC hit in each of the three stations of the T stations.

Downstream acceptance: at least one MC hit in each of the two stations of the TT, and at least one x and one stereo MC hit in each of the three stations of the T stations.

T acceptance: at least one MC hit in each of the three stations of the T stations.

The hits that are detected by the tracking sub-detectors, correspond to MC hits or to simulated noise. In the detector simulation, a fraction of the MC hits are not converted into observed hits, for instance to simulate detection efficiencies. A MC particle is defined to be reconstructible as one of five particle types, if its MC hits result in hits that meet the following criteria:

Velo particles create at least three ϕ and three R hits in the VELO.

Upstream particles create at least three ϕ and three R hits in the VELO, and at least one hit in each of the two stations of the TT.

Long particles create at least three ϕ and three R hits in the VELO, and at least one x and one stereo hit in each of the three stations of the T stations.

Downstream particles create at least one hit in each of the two stations of the TT, and at least one x and one stereo hit in each of the three stations of the T stations.

T particles create at least one hit in each of the three stations of the T stations.

5.2 Seeding

The Velo and T-stations register sufficient hits of a traversing charged particle to allow them to be used as a starting point for the track search. The strategies for identifying Velo (5.2.1) and T station (5.2.2) seeds are detailed in this section. In general, they aim to efficiently identify the seeds, while reducing the number of combinations which are inspected, and thereby the amount of computing power required. This is also the case for the track finding strategies of the next section. The techniques involve cuts, which have been tuned on Monte Carlo data samples to minimise the ghost rate (5.4.1), while conserving efficiency.

5.2.1 Velo seed

The hits that are detected by the VELO sensors are inspected to identify those combinations of hits that are likely to be caused by individual particles [100]. Determining which hits belong together is based on a number of assumptions. Firstly, the path of a particle traversing the VELO is considered to be a straight line. This is motivated by the fact that the magnetic field integral in that region of LHCb is sufficiently small, see section 4.3. Secondly, each of the particles is assumed to originate from the interaction region (σ_z = 53 mm), in agreement with the interaction point design [55]. B mesons mainly fly along the beam-axis for an average distance of 12 mm, making this an acceptable assumption for them. Under these conditions, a particle predominantly passes through the same sector of each R sensor on its path. Thirdly, only combinations of R hits from the same sector of different modules are considered. Two collaborating strategies are adopted for finding VELO seeds, as described next.

A two-dimensional straight line in Rz-space is constructed for each combination of R hits from two sensors, where those sensors are required to be separated by either one or two stations. Hits in the intermediate stations are added, provided they are located within 0.9 of a strip-pitch from the straight line. The resulting collection of R hits form the basis of a Velo seed candidate. This candidate is linearly extended both upstream and downstream, and hits within 4.4 strip-pitches are incorporated to augment the seed. Hits from sensors of the other detector-half have an additional 0.6 strip-pitches tolerance for being included in the seed. The resulting Rz track offers a crude estimate of the azimuth, based on the geometrical extend of an R sector, being about 45°. Backward pointing candidates using the pile-up sensors are used in the L0 trigger, as detailed in subsection 3.5.1.

Next, an Rz track has its azimuth angle information improved. This is achieved by adding compatible ϕ hits to the Rz track. As a starting point, the most downstream station, that contributes an R hit to the Rz track, is chosen. Its hit ϕ sensor and the more downstream neighbour have a 45° region, determined by the Rz track, searched for hits. This process is continued upstream until two sensors with ϕ hits within this 45° region are found. Those hits are then added to the Rz track to form a three-dimensional seed candidate called a 3D track. More than one candidate may be constructed, as all hits within the same 45° sector of all encountered ϕ sensors are compatible. These 3D tracks are extrapolated towards the interaction region, up to one station further than the last one with an R hit on the Rz track. ϕ Hits of the intersected stations are located within $(0.15\Delta z/60)^2$ radians [100] and added to augment the 3D track.

At least three R and three ϕ hits are required to be assigned to the straight line for it to be considered a valid seed candidate. In addition, a minimum fraction of 0.35 of the traversed stations must have contributed a hit to the 3D track. A straight line is fitted through the R and ϕ hits, and 3D tracks with a χ^2 per degree of freedom (n_{DOF}) larger than 4 are discarded. The seed candidate with the most ϕ hits or, in case of a tie, the one with the smallest χ^2/n_{DOF} value, is kept.

Not all Velo seeds need to originate from the interaction region, as assumed up till now. A second search strategy is used to find those seeds that do not. They are reconstructed from the hits which have not been used up to this point. Those remaining R and ϕ hits are paired in each module, to make space-points. Two space-points that are separated by a station, have a compatible space-point searched for in the intermediate module, with which they form a triplet. Starting with the triplet with the best χ^2 value of a straight line fit through its space points, an extension is made to match it with other triplets and form a Velo seed.

5.2.2 T-station seed

A T-station seed consists of hits from the Inner and Outer tracker sub-detectors, that are located downstream of the magnet [101, 102]. It represents the path of a particle going through the T stations. This path is described using a straight line in the yz plane, and motivated by the size of the magnet's fringe field as discussed in 4.3, it is parameterised as a parabola in the xz-projection. A combination of two techniques is used, as described next.

At some locations, the density of hits can occasionally be such that an unpractically high amount of possible combinations of hits arises. It has been determined that the hits in those regions can be ignored without significantly affecting the seeding performance [101]. In case of the Outer Tracker, groups exceeding seven neighbouring hits are removed, as they are observed to be caused by particles with too large an angle to be reconstructed. In addition, all hits from modules with an occupancy exceeding 40% are discarded. Concerning the Inner Tracker, hits from readout chips with more than 48 out of 128 hit channels are not used in the seeding. Together, the removed hits amount to 10% of the total number of T-station hits in an event.

A first seeding strategy separates the T stations into five sectors. The first four are formed by the upper and lower halves of the IT and OT respectively, with the fifth being composed of the left and right boxes of the IT stations. Per sector, all hits in the x layers of the three OT tracking stations are indexed. They form the basis of the xz-projection of a particle's path. Pairs of hits from the two outermost x layers are connected by straight lines, that are required to have an x slope smaller than 0.8. Additional hits are searched for inside a 20 mm wide window, centred around such a straight line. A pair of hits becomes a seed candidate if hits in at least half of the intermediate x layers are found. One of the selected hits from the middle station is used together with the starting hits to form a parabola. Stereo hits that are encountered by the xz-line, supply y coordinate information. A straight line in the yz plane is constructed in an analogous way as the parabola in xz.

A second T-station seed finding strategy is applied on the remaining unused OT and IT hits. Of those hits, the ones in the Inner Tracker are formed into so-called stubs. These are straight lines, consisting of four hits from a single IT station. Stubs from the first and second stations are compared at their central z coordinate and linked together if their x and y coordinates differ less than three mm each. This is followed by a search for a matching stub in the third station. The same procedure is followed when starting with stubs from the second and third stations. Triplets of stubs are fitted with a parabola in xz and a straight line in yz. Any remaining stubs are extrapolated into the Outer Tracker, where a sufficient number of compatible hits is searched for. Again, a parabola is used in the xz plane and a straight line, from the interaction point through the stub, in the yz plane.

The sample of found T-station seeds is reduced by applying quality selection criteria. Each OT seed is required to contain a minimum of 15 hits, of which at least five originate from the stereo layers. For the remaining seeds, a likelihood value is calculated. This value is based on the number of expected hits, taking into account gaps between sensitive detector components, see [101]. Once sorted by likelihood, a seed is discarded if it shares more than three hits with a previous track or has a likelihood value smaller than -30. In effect, this allows for more than one T-station seed to be found for each particle which traverses the T stations.

5.3 Track finding

The Velo and T-station seeds are used as the basis for four track finding strategies. Each strategy is specialised in finding tracks of one of three track types: Long tracks, Upstream tracks or Downstream tracks. When running the pattern recognition in filtered mode, they are executed in order, generally using only the seeds and hits that have not been used for the previous strategy. Exceptions are formed by the Forward and Match strategies both being allowed to use all seeds and hits and the Upstream and Downstream tracks, which can both use all TT hits that have not been used for Long tracks. In this approach, tracks with the largest number of contributing tracking sub-detectors are looked for first. These are the Long tracks, which are identified by two strategies.

The Forward and Match pattern-recognition strategies are complimentary in finding Long tracks, and are described in subsections 5.3.3 and 5.3.4. The overlap between the Long tracks found by these two methods is determined from MC information in subsection 5.4.2, and, based on the fraction of common hits, removed during the track fit, see section 7.1. After the Long tracks have been found, a number of Velo and T-station seeds remain unused. These are used as starting points for the identification of the Upstream and Downstream tracks in an event. The Upstream tracks are based on Velo seeds, as detailed in subsection 5.3.5. T-station seeds form the first part of Downstream tracks, which is elaborated on in subsection 5.3.6. Finally, Velo and T tracks are created from the seeds that are left over at the end of the track finding process, as described in subsections 5.3.1 and 5.3.2.

Tracks can also be created by using the Monte-Carlo information of an event to determine which hits belong together, as described in subsection 5.3.7. The resulting tracks are used to determine the performance of the track finding strategies.

5.3.1 Velo tracks

A Velo seed is complemented by a momentum estimate to form a Velo track. The momentum is used in the track fit to take material effects into account, see subsection 6.3.7. The magnetic field integral in the VELO region is not sufficient to determine the momentum of the particle [100]. Therefore each Velo seed is assigned a transverse momentum of 400 MeV, an average which is obtained from inspection of the MC information of a sample of particles passing only through the VELO. The momentum vector is deduced from that and the direction of the seed.

5.3.2 T tracks

T-station seeds that are not used to form Long or Downstream tracks, become T tracks. The momentum of a T-station seed, determined from the parabolic xz-projection, has an average resolution of 24% [101]. This momentum estimate can be improved to a RMS value of 5% and a core of 1.6% by using the so-called p_T kick method.

In the p_T kick approach, the effect of the magnetic field on the path of a particle is modelled by a single change of direction of the momentum vector in the xz-plane, near the centre of the magnet. This instantaneous change is referred to as a kick in transverse momentum, and is illustrated in figure 5.2.

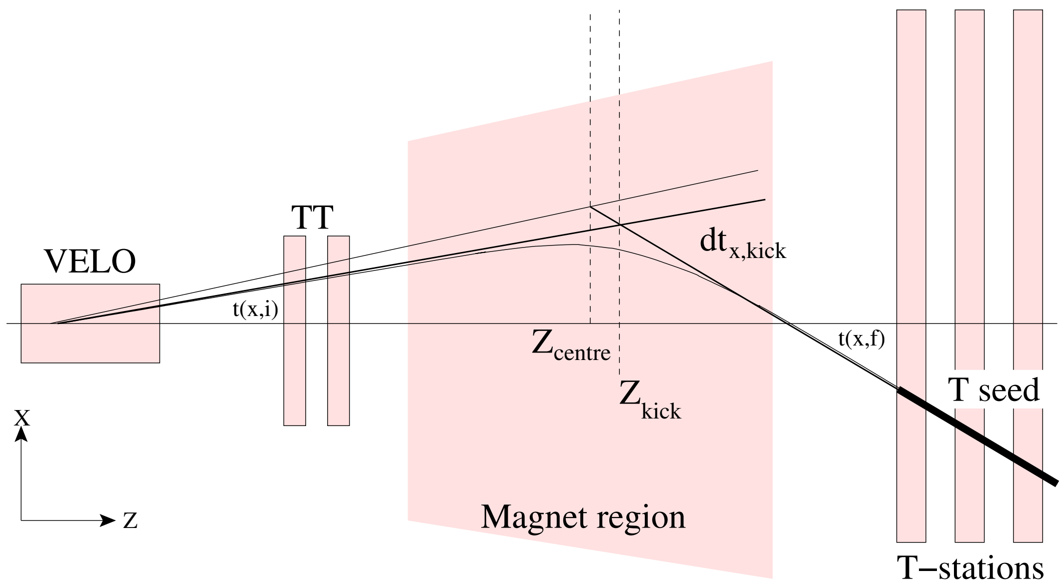

Figure 5.2: *Illustration of the application of the p_T-kick method. The main component of the magnetic field is perpendicular to the drawn plain.*

Limiting the effect to the x-component of the momentum is motivated by the main component of the magnetic field being along the y-axis. The kick is initially located at the z-coordinate z_{centre}=5150 mm, where the field integral along the beamline reaches half its total value. A straight line extrapolation of the T-station seed to this z-coordinate is made. From z_{centre} onwards upstream, the path kinks to point towards the interaction point. To improve the momentum estimation, the field integral is recalculated along these two lines, resulting in a new z-coordinate z_{kick} where the integral equals half its total value. The extrapolation of the seed is then redone. The kink that is found in this iteration corresponds to a change in the x-component of the momentum vector, as given by:

$$\Delta p_x = p\left(\frac{t_{x,f}}{\sqrt{1+t_{x,f}^2+t_{y,f}^2}} - \frac{t_{x,i}}{\sqrt{1+t_{x,i}^2+t_{y,i}^2}}\right) = q\int \left| d\vec{l}\times\vec{B}\right|_x \quad [\mathrm{MeV}]\,, \tag{5.1}$$

where t_x and t_y refer to the slopes in x and y, i and f indicate evaluation at smaller and larger z than z_{kick}, q is the particle's electric charge, and l is the distance along the two straight lines. In this equation, the momentum p is the only unknown and hence can be determined. This momentum estimate is corrected for a systematic underestimation of the momentum, which is observed in the mean of the momentum error distribution [58]:

$$< \delta p/p >= -0.04 - 0.14 t_{x,f}^2\,. \tag{5.2}$$

5.3.3 Forward

Forward pattern recognition creates Long tracks from a Velo seed, to which first T-station hits and later TT hits are added [103]. The Velo seed is extrapolated in a straight line to each x-layer in the T stations, where x hits of compatible IT strips and OT wires are sought within a y-coordinate window of $10{+}50|t_{\mathrm{y,velo}}|$ mm. These hits are projected onto a reference plane near the middle of the T stations at z=8250 mm. In that plane their distance in x to the extrapolated Velo seed must be less than $5.25|t_{\mathrm{x,velo}}|$ mm. A Hough transform [104] with momentum, charge and hits type dependent binning, selects candidate groups of hits from the various x-layers. It demands that the difference in the x-distance between the originally most upstream hit and any of the other hits, now projected onto the reference plane, is limited to:

$$\Delta x = 0.6 + 0.011|x_{\mathrm{first}} - x_{\mathrm{seed}}| \quad [\mathrm{mm}]\,, \tag{5.3}$$

where x_{first} is the x-position of the first hit, and x_{seed} is the x-position of the extrapolated Velo seed at the projection plane. In case the first hit comes from the OT, the accepted difference is increased by a factor of 1.5. The found groups must contain at least hits of five out of the six different x-planes.

A subset of hits is selected from each group, that represent each of the different x-planes with a minimal spread of the distances in x at the reference plane. This subset is fitted with a cubic parameterisation in the T stations. Additional hits from the original group are added to the subset if they are located within 0.2 mm (IT) or 2 mm (OT) in x from the fitted curve. Hits are removed from the subset when their χ^2 contribution to the cubic fit exceeds 20. Track candidates that end up with fewer than five hits in different x-layers are discarded. On average two to five candidate groups of hits are left over per Velo seed.

After the x-layer hits have been found, hits in the stereo layers, that lie within 10 mm of the fitted track candidate, have their x-component projected onto the reference plane at 8250 mm. A second Hough transform, similar to the one for x-layer hits, selects compatible groups of hits, coming from at least four different stereo layers. In the Hough transform, the maximum allowed distance in x between the hits in a group is $1.5 + 70/p^2$ mm, with p in GeV, and is scaled by a factor of 1.5 if the first hit comes from the OT. On the found groups, a second cut is made on the maximum difference in x between any of the hits. This cut is 3 mm when the first hit is an IT hit and 4.5 mm if it is an OT hit. The track candidates with stereo hits are refitted in x with a third order polynomial and fitted with a straight line in y. Hits with a χ^2 contribution over 20 as well as track candidates that represent fewer than nine out of the twelve planes are removed. Track candidates that pass through the IT region are required to contain at least seven IT hits, while a track candidates in the OT region must have a minimum of 16 OT hits. The track candidate with the largest number of hits and all track candidates with at least 22 out of the possible 24 hits are selected to have compatible TT hits added.

A search for hits in the TT layers is performed for the remaining track candidates. The candidate's Velo seed is extrapolated along a straight line to the layers of the TT. For each hit, the p_T kick method, see subsection 5.3.2, is used to create two straight lines through the Velo and the TT, which meet in between at z=1650 mm. Based on the distance in x between a TT line and a TT hit, hits that are close enough have their distance recalculated at a plane in the middle of the TT at z=2500 mm as x_{proj}. Groups of hits are searched for in a window of $2+0.25|x_{\mathrm{proj}}|$ mm around a seed hit. The groups of hits are fitted with a straight line, and of all groups that consist of hits from at least three different layers, the one with the lowest χ^2 is added to the track candidate, to form a Long track.

5.3.4 Match

The matching strategy combines Velo seeds with T-station seeds, to which TT hits are then added to create Long tracks [105, 106]. It considers T-station seeds with a minimum momentum of 2 GeV, obtained during the seeding from the fitted parabola in the xz-plane. Those seeds are extrapolated in the upstream direction, using a fifth order Runge-Kutta method [107], to a plane at the end of the VELO (z=830 mm). There they are compared to Velo seeds, that have been extrapolated along a straight line to the same plane. The matching requires the transverse momentum, determined from the Velo seed angles and T-station seed momentum estimate, to be at least 80 MeV. A matching χ^2 of a pair of seeds is determined from the parameters $\vec{x} = (x, y, t_x, t_y, q/pc)$ and covariances C of those seeds as:

$$\chi^2 = (\vec{x}_{\mathrm{Velo}} - \vec{x}_{\mathrm{T}})^T (C_{\mathrm{Velo}} + C_{\mathrm{T}})^{-1} (\vec{x}_{\mathrm{Velo}} - \vec{x}_{\mathrm{T}})\,. \tag{5.4}$$

A pair of seeds is considered a track candidate when the matching χ^2 is smaller than 900. As multiple scattering is not taken into account during the upstream extrapolation of the T-station seed, this cut needs to be set high in order to efficiently find low momentum tracks [106]. For a seed that is paired with multiple other seeds, the combination with the lowest matching χ^2 is retained.

Each of the resulting track candidates has their Velo seed parabolically extrapolated into the TT, using the momentum estimate of its T-station seed. A TT hit is added when its distance to the track candidate is less than 3 mm. One TT hit is allowed to be added per layer and at least three layers need to contribute to the track candidate for the TT part to be valid. The difference in the distances of hits to the track candidate is allowed to be 1 mm within a station and 2 mm between the two different stations. Multiple candidate groups of TT hits can be found by this procedure. The group of TT hits that is assigned to the final matched track, is the one with the smallest value of q^2:

$$q^2 = \bar{d}^{\,2} + 49 s_d^2 . \tag{5.5}$$

In this equation, $\bar{d}$ is the mean distance of the hits to the track and s_d is the RMS of the distribution of the distances.

5.3.5 Upstream

Tracks passing only through the VELO and TT detectors, are called Upstream tracks and are found using the pattern recognition method documented in [108]. It finds low momentum as well as high $\mathrm{p_T}$ tracks before they leave the detector volume in the magnet region.

Velo seeds are extrapolated along a straight line to the central z-coordinate of the TT, at z=2470 mm. An initial search window is opened to locate candidate TT hits. The size of this window is proportional to the inverse momentum of the track candidate, with the momentum determined as for Velo tracks, see subsection 5.3.1. A candidate hit has its distance in x to the straight line extrapolation calculated, which is subsequently rescaled to the value Δx^{norm} that it would have at the central z-coordinate of the TT.

The candidate TT hits are searched for compatible collections. Each collection consists of an initial TT hit and additional hits from other layers that differ in Δx^{norm} by a layer-dependent maximum amount. A straight line is fitted through each candidate set of TT hits. In the xz plane, this line is extrapolated back to a point at $(x_{\mathrm{Bdl}}, z_{\mathrm{Bdl}})$, where the magnetic field integral from the interaction point to the last TT station reaches half its total value. This is a version of the p_T kick method of subsection 5.3.2, and produces a second straight line from $(x_{\mathrm{Bdl}}, z_{\mathrm{Bdl}})$ to the interaction point. The difference in slope in the xz plane between that line and the original extrapolated Velo seed is noted as $\Delta t_x^{\mathrm{velo}}$, where $t_x \equiv dx/dz$. Each TT hit has a deviation Δx in x with the straight line that was fitted through their set of compatible TT hits. These quantities form the bases for a χ^2, which is given by:

$$\chi^2 = \left(\frac{\Delta t_x^{\mathrm{velo}}}{\sigma_{t_x^{\mathrm{velo}}}}\right)^2 + \sum_{i=1}^{n}\left(\frac{\Delta x_i}{\sigma_{x_i}}\right)^2 \equiv f_1(x_{\mathrm{Bdl}}) + f_2(x_{\mathrm{Bdl}}, t_x^{\mathrm{tt}}) , \tag{5.6}$$

where σ denotes the errors of the stated parameters and the summation is over the TT hits. Minimising the χ^2 with respect to the parameters x_{bdl} and t_x^{tt}, produces the final χ^2 value for the fitted candidate. Per Velo seed, the three track candidates with the lowest χ^2 values are refitted by a Kalman filter, see chapter 6, and the one with the lowest χ^2 per degree of freedom is selected as the final Upstream track.

5.3.6 Downstream

A Downstream track is created from a T-station seed and TT hits [109]. It might represent a long-living particle, that has decayed outside of the VELO. For each T-station seed, TT hit candidates are identified, using a variation on the p_T kick method of subsection 5.3.2. It uses a parameterisation, as in the Forward pattern recognition, to determine the z-coordinate z_{magnet} where the TT segment and T-station seed intersect [109]:

$$z_{\mathrm{magnet}} = 5368.54 - 2155.88t_y^2 + 595.27t_x^2 - 0.00001455x^2 \quad [\mathrm{mm}]\,. \tag{5.7}$$

This parametrisation is a function of the x-position (x) and the x and y slopes ($\mathrm{t_x}$ and $\mathrm{t_y}$) of the T-station seed at z=9450 mm. The coefficients of this parameterisation have been determined from a fit to Monte-Carlo information.

Along a straight line from the intersection back to the interaction point, a momentum (p) dependent search window of $100/p + 10$ mm, with p in GeV, is opened. This window is wide, as it takes into account the fact that decay products of long-lived particles do not point straight back to the interaction point. It's value has been determined by inspecting the worst-case scenario of a 2 GeV pion, originating from a decayed K_s^0 [109]. All hits that fall within this window together form the group of candidate hits. Looping over all x-hits in this group as starting points, TT hits in the other x-layer that lie within 3.5 mm from the straight line, are identified. For each pair of x-hits, stereo hits that are located within 3 mm of the straight line, are added to form a track candidate. Hits may be removed from the candidate to improve the χ^2 value of the straight line fit to below 10. In total a minimum of three layers must contribute hits to a valid track candidate. X-hits that are included in the candidate, are not used in searches that are based on other x-hits as seeds, thereby reducing combinatorics. Of all the resulting track candidates, the one with the highest number of contributing layers out of the possible four is selected. In case of multiple equal candidates, the one with the lowest χ^2 per degree of freedom is used to create the Downstream track.

The momentum error distribution of the final Downstream tracks is fitted by a sum of two Gaussian functions, where the width of the inner Gaussian quantifies a momentum resolution of 1%. This is done by using a parameterisation as a function of the TT segment slopes, and the angle ($dt_{\mathrm{x,kick}}$) in the x-plane between the TT segment and T-station seed at the kink of the p_T kick method:

$$p = \frac{1190.86 + 605.67t_x^2 + 2656.55t_y^2}{dt_{\mathrm{x,kick}}} \quad [\mathrm{MeV}]\,. \tag{5.8}$$

The difference in momentum with the estimate of the T seed (see subsection 5.3.2), divided by the track momentum must be less than 0.7, otherwise the track is discarded as not originating from the interaction point.

5.3.7 Ideal pattern recognition

It is possible to use the Monte-Carlo information of simulated events to determine which hits belong to a particle. Tracks made out of these hits represent the ultimate performance that can be obtained by the pattern recognition. These tracks are mainly used for performance studies of the track fitting in chapter 7.

The creation of these ideal tracks begins by inspecting each Monte-Carlo particle individually. A particle is considered reconstructible when it meets the various criteria specified in subsection 5.4.3. This will determine as which type of track the particle will be reconstructed. The simulation creates tables that couple the particles to the hits that they created, and these hits are assigned to the ideal track.

5.4 Performance

Tracks found by the pattern recognition form the starting point for the track fitting process. In order to be able to put the performance of the track fitting into perspective, it is necessary to know a number of properties of the tracks before fitting. These properties are quantified and discussed in this section. Two different types of averaging procedures are used, depending on the track or event property under consideration. These procedures are named event-averaged (EA), and track-averaged (TA). In case of MC particles, TA becomes particle-averaged (PA). These procedures are defined as follows:

EA A quantity can be determined for each event. Summing the quantity's values over all events, and dividing that sum by the total number of events, results in the event-averaged value of the quantity.

TA A quantity can be determined for each track. Summing the quantity's values over all tracks in an event sample, and dividing that sum by the total number of tracks, results in the track-averaged value of the quantity.

A concentration of tracks that contribute to the outer percentiles of the distribution of a quantity, is observed in some events. This can for instance be caused by multiple primary interactions and a high particle multiplicity in the detector. Such events can be chosen to be excluded from study in a physics analysis. As each event is assigned the same weight in the event-averaging procedure, the impact of those tracks on the total average is reduced, compared to track-averaging. A quantity with a track-average around 10% is therefore expected to have a lower event-average in this scenario. The event-average is expected to be higher than the track-average, in case the latter is around 90%.

Each of the pattern recognition strategies, described in sections 5.2 and 5.3, produce a number of seeds or tracks. The seeds are used in the various types of tracks, and only the tracks are fitted and used in physics analyses. In total, an average of 104.8 ± 0.05 tracks are found per event. The event-averaged number of seeds and tracks is split by strategy, and listed in table 5.1. Subsections 5.4.1 and 5.4.2 discuss the correctness and uniqueness of the tracks that are found by the pattern recognition. The efficiencies with which the tracks corresponding to charged particles are found are detailed in subsection 5.4.3. Finally, the average number of each type of hit in the various types of tracks, as well as the efficiency and purity with which those hits are found, is discussed in subsection 5.4.4.

Table 5.1: *Average number of seeds and tracks found in an event by the pattern recognition, split by strategy. The uncertainty on these numbers is smaller than the last presented digit.*

strategy	EA number
Velo seeding	62.9
T-station seeding	42.9
Velo PR	31.3
Upstream PR	7.4
Forward PR	23.2
Match PR	19.8
Downstream PR	9.4
T PR	13.7

The Velo seeds are used by the Forward, Match, Upstream and Velo track finding strategies. As the pattern recognition is performed in filtered mode, see section 5.3, the numbers in table 5.1 show that 24.2 Velo seeds per event are used as part of Long tracks. The Match strategy uses an event-average of one Velo seed that is not used by the Forward strategy. Executing the Match strategy in addition to the Forward strategy therefore increases the Long track finding efficiency, as discussed in subsection 5.4.3. Of the 38.7 Velo seeds which are not used in the Long tracks, the Upstream pattern recognition finds extensions in the TT for 7.4 seeds. All of the remaining Velo seeds become Velo tracks.

T-station seeds are used in tracks by the Match, Downstream and T pattern recognition strategies. Around 46% of those are matched to Velo seeds by the Match strategy. Downstream tracks are created from some 41% of the remaining T-station seeds, by finding compatible hits in the TT. Those T-station seeds which are not part of Long or Downstream tracks, are converted into T tracks.

5.4.1 Ghosts

Inspecting the Monte-Carlo information available for the simulated events, it is observed that not all hits on a given track belong to the same MC particle. Some hits originate from other particles and are assigned to the track due to coincidental compatibility. In addition, some included hits are due to simulated detector noise. The inclusion of these incorrect hits does not invalidate a found track, but their presence does influence the reconstructed path that the track represents after fitting.

To be an acceptable track, a limit is defined on the presence of incorrect hits in the collection of hits that form the track. Exceeding this limit results in the track to be considered as due to a chance combination of hits. Such tracks are referred to as ghosts. For simulated events, the hits of a track can be traced back to the Monte-Carlo particles which created them. Each track in an event can be inspected to determine the fraction of correct hits. This information is available separately for each tracking sub-detector. A track must satisfy each of the following three requirements, or it is labelled as being a ghost.

1. The track contains more than two VELO hits and at least 70% of those VELO hits relate back to a single MC particle. Alternatively, the track contains less than three VELO hits.
2. The track contains more than 2 T-station hits and at least 70% of those T-station hits relate back to a single MC particle. Alternatively, the track contains less than three T-station hits.
3. The track contains more than two VELO hits and more than two T-station hits. Alternatively, the Monte-Carlo particle created at least all but one of the TT hits.

Utilising these criteria to identify ghosts, all tracks found by the pattern recognition strategies are inspected. In the discussion of ghosts, the ghost rate g of a collection of tracks is used, which is defined as:

$$g = \frac{N_{\text{tracks}} - N_{\text{associated}}}{N_{\text{tracks}}}, \tag{5.9}$$

where N_{tracks} is the number of found tracks and $N_{\text{associated}}$ is the number of tracks that are associated, through the above specified requirements, to a MC particle.

In table 5.2, the event-averaged and track-averaged ghosts rates are listed by pattern recognition strategy. Consistent with the prediction at the beginning of this section for quantities with low track-averages, the event-averaged numbers are smaller than the track-averaged ones. The Forward and Match strategies are optimised for track finding efficiency, and not to minimise the ghost rate. As they form the dominant input for physics analyses, the basic measures to reduce their ghost rates are discussed after this paragraph. The Upstream strategy suffers from a higher fraction of ghosts than the Forward and Match strategies, as it uses wider cuts to efficiently find hits for tracks representing low momentum particles. The Downstream ghost rate is around 25%, indicating that the strategy should be improved, as is noted in [109]. It is due to the considerable width of the momentum-dependent selection window for TT hits, as described in subsection 5.3.6, which allows for multiple groups of TT hits to be compatible with a T-station seed, of which an incorrect group is selected too often. Velo tracks show the lowest ghost rate of all track types, as they contain many hits with relatively small interspacing within a low magnetic field region, allowing for tight selection cuts. All of the unused T seeds become T tracks. As the Match strategy is more likely to find matches with Velo seeds for correct T seeds, the T tracks are expected to contain a higher fraction of ghosts than Long Match tracks, as is observed.

The ghost rate of the Long track collections, found by the Forward and Match strategies, are determined for a number of ranges in transverse momentum. In figure 5.3, the resulting event-averaged and track-averaged ghost rates are shown, for different cut-off values of the p_T of the tracks. Long tracks found by the Forward pattern recognition have, over the entire p_T range, a higher ghost rate than found for tracks from the Match strategy.

Table 5.2: *The event-averaged and track-averaged ghost rates, split by pattern recognition strategy. The uncertainty on these numbers is smaller than the last presented digit.*

strategy	EA ghost rate [%]	TA ghost rate [%]
Velo PR	5.9	7.4
Upstream PR	13.8	16.0
Forward PR	9.1	11.4
Match PR	7.2	8.5
Downstream PR	25.0	35.3
T PR	11.5	14.6

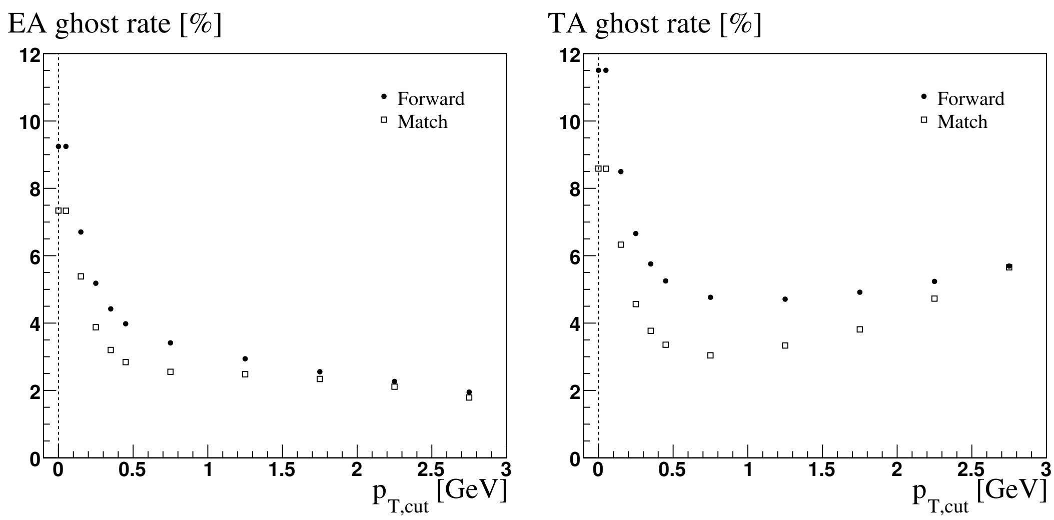

Figure 5.3: *Event-averaged (left) and track-averaged (right) ghost rates of Long tracks from the Forward and Match pattern recognition strategies, as a function of the transverse momentum cut-off value.*

When averaging over events, the ghost rates decrease for increasing values of the p_T cut-off value. This shows that tracks with a higher transverse momentum are found at a lower ghost rate than tracks with a lower p_T. The track-averaged ghost rates show the same behaviour for the first half of the p_T cut range, after which the rate increases. Combining the results of the two averaging procedures leads to the conclusion that ghosts in the second half of the p_T cut range tend to be concentrated in a limited fraction of events. Based on these observations, the concentration of ghost tracks in a Long track sample used for physics analyses, can be reduced by applying a cut on p_T.

A p_T cut is part of the standard track selection procedure for the $B_s^0 \to D_s^- \pi^+$ channel, which uses Long tracks from events like those studied here. It selects tracks with a minimum momentum of 2 GeV and a transverse momentum over 300 MeV [110]. This results in EA ghost rates of 4.4% and 3.1%, and TA ghost rates of 5.8% and 3.9%, for track collections from the Forward and Match pattern recognition strategies, respectively. These constitute a 49–60% reduction in the inspected ghost rates. Further reduction is expected when performing a mass-constrained vertex fit as described in [58]. This because a ghost track is less likely to have the proper momentum to result in the known mass of for instance the D_s^-, when combined with two other tracks. It is observed that ghost tracks are not a limiting factor in most B-decay event selections [111]. A number of ghost tracks meet the trigger criteria, allowing for a non-B decay event to be selected. This occurs at the expense of the available bandwidth for selecting events which are interesting for physics analyses, which is currently under investigation [112].

5.4.2 Clones

A particle can be reconstructed as different types of tracks, either if it has created hits in more than one tracking sub-detector or when incorrect hits are ascribed to the particle by the pattern recognition. Finding the same particle more than once without offering an improvement of the pattern recognition performance, as subsection 5.4.3 shows the Forward and Match combination does do, is wasteful of computing resources. In order to limit the occurrence of a particle being found more than once, the seeds and hits that are used by one strategy are not made available to subsequent pattern recognition strategies. An exception is made for the Forward and Match strategies, those both have all seeds and hits available for finding tracks. In addition, Upstream and Downstream tracks can both use all of the TT hits that have not been used in Long tracks. This approach requires the track types to be found in decreasing order, beginning with the one that includes the highest number of different tracking sub-detectors. As not all of the hits belonging to a particle need to be found when creating a track, it is still possible for another pattern recognition strategy to find the same particle again.

Two tracks that are both based on hits from the same particle are called clones. As a part of the track fitting process, a choice is made after fitting the tracks, which track of a pair of clones is removed, see section 7.1. A track has its hit content compared with the hits of each Monte-Carlo particle separately. The hits must meet the criteria stated in subsection 5.4.1 for the track to be coupled to the particle. Tracks are determined to be clones when they are both coupled to the same Monte-Carlo particle. The percentage of tracks that are clones are stated in table 5.3. All of the event-averaged values are higher than the track-averaged ones. This is consistent with the expectation stated at the beginning of section 5.4, when taking into account that the strategies after Forward and Match have their clone rates suppressed by running in filtered mode.

Table 5.3: *The event-averaged and track-averaged percentages of clones, split by pattern recognition strategy. The uncertainty on these numbers is smaller than the last presented digit.*

	EA clones [%]	TA clones [%]
Velo PR	0.8	0.7
Upstream PR	0.4	0.3
Forward PR	77.3	74.7
Match PR	89.2	87.7
Downstream PR	17.0	14.2
T PR	0.5	0.4

Long tracks found by the Forward and Match strategies are compared to each other to determine their clone fractions. As they search for the same tracks, their clone rates are expected to be high. It is calculated to be around 80%, indicating that there remains a use for running both of them. Upstream and Downstream tracks are compared to Long type tracks, and those which have already been found as Long tracks are considered to be clones. Velo tracks can be clones of Upstream or Long tracks and T tracks can be clones of Downstream or Long tracks. Both Upstream and Velo clones are due to clones among the Velo seeds, and therefore amount to negligible fractions. Analogously, the Downstream and T clones rates are expected to be low. The reason why Downstream tracks still contain a sizeable fraction of clones, is that some of the T-station seeds that it uses, which are not used by the Match strategy, do overlap with the T-station hits that have been used by the Forward strategy. As the Forward and Match strategies both use Velo seeds, a similar effect does not occur for Upstream tracks. Clones will be removed at the end of the track fit, as described in section 7.1.

5.4.3 Track finding efficiency

The efficiencies with which the pattern recognition strategies create tracks that represent particles are detailed in [100, 101, 102, 103, 105, 106, 108, 109]. These numbers are obtained while running in concurrent mode, which makes all seeds and hits available to each strategy. For determining the efficiencies in filtered mode, the following selection criteria are applied to the MC particles:

- The MC particle is reconstructible, see 5.1;
- The MC particle has a minimum momentum of 1 GeV;
- The MC particle has a non-zero electric charge;
- The MC particle does not interact hadronically downstream of the vertex;
- The MC particle is not an electron.

In filtered mode, particles that are found by the Forward or Match strategies, are not sought by the subsequent strategies, and are therefore not included in the determination of the efficiencies of those latter strategies. The same is the case for particles, found by the Upstream or Downstream strategies. The efficiency numbers for both the seeding and the track finding strategies are listed in table 5.4. The event-averaged efficiencies are higher than the particle-averaged efficiencies, as the first method assigns relatively less weight to the content of inefficient events, compared to the second method. Velo and T seeding predominantly loose their efficiency in finding low momentum particles, predominantly below 2 GeV [100, 102]. They reach their respective efficiency plateaus of 97.4±0.05%(PA) and 96±0.5%(EA) at 5 GeV [100, 102]. The seeding efficiencies can be increased by opening up the selection windows used by the seeding strategies, at the cost of creating more ghosts. This is not considered to be useful, as tracks with momenta below 2 GeV are rejected by the track selection criteria of physics analyses, as was seen in subsection 5.4.1. The inefficiencies of the track finding strategies have a number of causes, as discussed next.

Table 5.4: *The event-averaged and particle-averaged efficiencies of the seeding and track finding strategies, based on reconstructible MC particles, while running the pattern recognition in filtered mode. The last row states the efficiency for finding Long tracks when combining the Forward and Match track collections. The uncertainty on these numbers is smaller than the last presented digit.*

strategy	EA efficiency [%]	PA efficiency [%]
Velo seeding	94.6	93.9
T-station seeding	85.7	84.9
Velo PR	73.4	73.3
Upstream PR	62.5	60.4
Forward PR	91.2	90.6
Match PR	85.9	85.4
Downstream PR	61.6	57.0
T PR	75.8	74.1
Long (F∪M)	94.5	93.7

First, all of the track finding strategies use seeds, and therefore cannot find particles for which no seed has been found. Long particles which are not found as Long tracks due to seeding inefficiencies, are therefore also not found by any of the other track finding strategies. The efficiency of each strategy depending on those seeds is thus lowered. For the same reason, Upstream particles with no Velo seed reduce the efficiency of the Velo strategy. Analogously, the T track finding efficiency is lowered by Downstream particles without T seeds.

Second, ghosts use seeds in tracks which do not correspond to a MC particle, and thereby some ghosts prevent a seed to be used to find the correct track. For example, the T seeds of Match ghosts are no longer available to the Downstream and T strategies, reducing their efficiencies. Analogously, a Velo seed which is a part of both a Forward ghost and a Match ghost, lowers the efficiencies of all other pattern recognition strategies. Similarly, Velo seeds used in Upstream ghosts reduce the Velo track finding efficiency, and T seeds used in Downstream ghosts lower the efficiency of finding T tracks.

Third, the Upstream and Downstream strategies reject track candidates which contain less than three TT hits. Upstream and Downstream particles are only required to have two TT hits associated to them. Therefore the Upstream and Downstream strategies are fully inefficient for all Upstream and Downstream particles with only two TT hits.

These three sources of track finding inefficiencies result in the pattern recognition strategies obtaining the efficiencies which are shown in table 5.4. As Long tracks are the dominant input for physics analyses, their efficiency is increased by combining the Forward and Match strategies. The resulting Long track finding efficiency is listed in the final row of table 5.4. Since these numbers are 3.1–3.3% higher than those of the Forward strategy, running the Match strategy in parallel with it is useful.

The efficiencies of the Forward and Match strategies for finding Long tracks have been determined as a function of the particle momentum and are shown in figure 5.4. The Forward strategy is more efficient than the Match pattern recognition, over the entire inspected momentum range. In general, the efficiencies increase with the momentum of the particle and reach plateau values. The Match PA efficiency becomes lower after its peak near 8 GeV. This is due to events with a high detector occupancy and with high momentum seeds, an issue which remains to be further investigated. In the momentum range from 1 to 5 GeV, the efficiency is notably lower than in the remaining momentum range, which is consistent with the Velo and T seeding efficiencies. The combined performance is also plotted, showing an overall improvement in efficiency, illustrating the benefit of executing both strategies.

A subset of the Long tracks represent particles which are decay products in B physics channels, such as those discussed in section 2.4. The reconstruction efficiency of such decays depends on the track finding efficiency to the power of the number of decay products. Table 5.5 lists the reconstruction efficiencies for the channels of section 2.4 in its first column [55]. These depend upon the Long track finding efficiency to the second or fourth power. In case of $B_s^0 \to J/\psi\eta$ decays, the efficiency is further reduced because of the requirement of finding the two photons in which the η decays. From these numbers, the average efficiency for finding B decay products is 95.4 ± 0.05%, which is a percent higher than for all Long tracks,

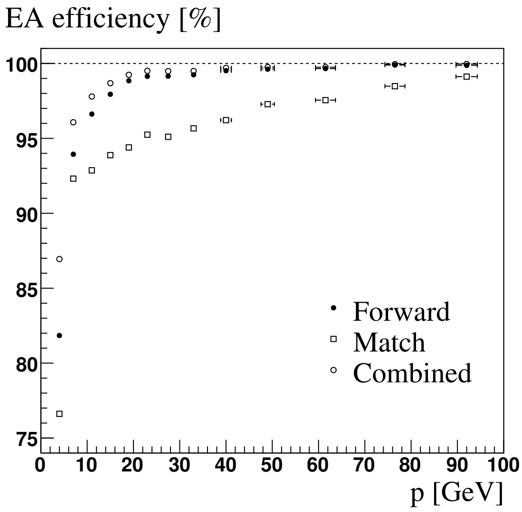

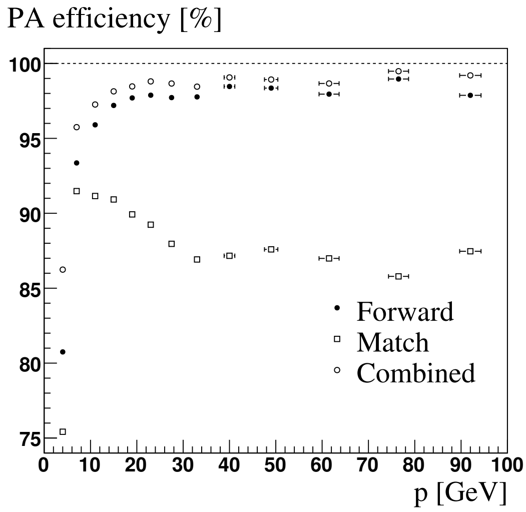

Figure 5.4: *Event-averaged (left) and particle-averaged (right) efficiencies for finding Long tracks of the Forward and Match pattern recognition strategies, as well as their combined performance, as a function of the momentum of the particle.*

Table 5.5: *The efficiencies of the track reconstruction software and the LHCb detector for finding the tracks corresponding to the listed decay channels [55]. The uncertainty on these numbers is smaller than the last presented digit.*

channel	$\epsilon_{\rm rec}$ [%]	$\epsilon_{\rm det}$ [%]
$B_s^0 \to D_s^- \pi^+$	80.6	5.4
$B_s^0 \to D_s^{\mp} K^{\pm}$	82.0	5.4
$B_s^0 \to J/\psi \phi$	82.5	7.6
$B_s^0 \to J/\psi \eta$	69.6	10.1
$B_s^0 \to K^+ K^-$	92.5	12.0
$B^0 \to \pi^+ \pi^-$	91.6	12.2

as seen in table 5.4. In the second column of table 5.5, the efficiency with which LHCb detects all final state particles of the listed decay channels. These are dominated by the detector acceptance, as the LHCb detector is a single-arm spectrometer. It is clear from those numbers that the reconstruction of B physics channels is not limited by the track finding efficiency.

5.4.4 Hit efficiency and purity

The number of hits on a track has been determined for all tracks. A separation of the tracks is made by pattern recognition strategy. The found hits are split by the tracking sub-detectors that recorded them, and the resulting track-averages are stated in table 5.6. Tracks contain fewer VELO hits on average as their pseudorapidity decreases, as seen from the VELO layout in figure 3.7. Since a fraction of the Upstream tracks have sufficient transverse momentum to leave the detector in

Table 5.6: *Track-averaged number of hits for all types together and for each type separately, split by pattern recognition strategy. The uncertainty on these numbers is smaller than the last presented digit.*

strategy	total	VELO R	VELO ϕ	TT	IT	OT	IT&OT
Velo PR	8.4	4.4	4.0	···	···	···	···
Upstream PR	14.7	5.5	5.4	3.8	···	···	···
Forward PR	36.3	6.6	6.2	3.4	12.3	21.4	20.1
Match PR	34.9	6.6	6.3	3.3	11.6	21.0	18.4
Downstream PR	23.0	···	···	3.7	10.8	20.2	15.3
T PR	15.7	···	···	···	11.1	19.1	14.6

the magnet region, see subsection 5.3.5, their mean number of VELO hits is lower than that of Long tracks, which must reach the T stations. Similarly, Velo tracks can occupy an even lower pseudorapidity region, reducing their hit content compared to Upstream tracks.

All strategies which use TT hits, require a minimum of three TT hits to be part of a found track. Therefore all of the TT hit averages in table 5.6 are between three and the maximum of four, given by the four layer physical layout of the TT. In contrast to Upstream and Downstream tracks, Long tracks have hits on both sides of the TT. Those restrict the search window for compatible TT hits more than the Velo seed or T seed by themselves do. That is why Long tracks contain fewer TT hits than Upstream and Downstream tracks.

Tracks with exclusively IT(OT) hits in the T stations contribute only to the statistics of the column that is labelled IT(OT). No difference in the mean T-station hit content is expected between track types, as all but one strategy uses T seeds. The exception is formed by the Forward strategy, which imposes similar demands on the T-station hit content as the T seeding. For tracks with only IT or OT hits, no significant difference in the means is observed. In case a track has both IT and OT hits, it contributes to the IT&OT column. That column shows a decreasing average number of T-station hits, which is consistent with the hit finding efficiencies of their respective pattern recognition strategies. Those efficiencies are discussed next.

A track that is not a ghost track, will have at least one Monte-Carlo particle associated to it. In that case, the hits forming the track can be checked to be created by that associated particle. The number of hits on the track that have been created by the associated Monte-Carlo particle (N_{correct}), divided by the total number of hits that the particle has created (N_{MC}), defines the hit efficiency ϵ:

$$\epsilon = \frac{N_{\text{correct}}}{N_{\text{MC}}} \, . \tag{5.10}$$

The number of hits on the track that have been created by the associated Monte-Carlo particle (N_{correct}), divided by the total number of hits on the track (N_{found}), defines the hit purity ρ:

$$\rho = \frac{N_{\text{correct}}}{N_{\text{found}}} \, . \tag{5.11}$$

The hit efficiencies are shown for tracks from each pattern recognition strategy in table 5.7. All of the VELO hits are found by the Velo seeding, which is less efficient at low momenta, as seen in subsection 5.4.3. Low momentum particles scatter more in the material of the VELO, possibly preventing them from being found on a straight line by the seeding algorithm. This implies that a low momentum Velo seed is less likely to contain all of the hits. Low momentum particles are found as Upstream and Velo tracks, which lowers their average hit efficiency, as seen in the first column.

Table 5.7: *Track-averaged hit efficiency for each strategy, shown for all hits together and for each hit type separately. The uncertainty on these numbers is smaller than the last presented digit.*

strategy	total ϵ [%]	VELO ϵ [%]	TT ϵ [%]	IT ϵ [%]	OT ϵ [%]
Velo PR	85.8	85.8	$\cdots$	$\cdots$	$\cdots$
Upstream PR	92.0	88.0	96.0	$\cdots$	$\cdots$
Forward PR	94.0	96.0	90.8	96.9	94.4
Match PR	90.3	96.7	89.9	89.2	83.5
Downstream PR	88.8	$\cdots$	94.9	74.4	84.4
T PR	79.4	$\cdots$	$\cdots$	85.9	73.9

The difference in efficiencies of finding TT hits are a direct result of the aforementioned reasons for which the Forward and Match strategies find fewer TT hits than the Upstream and Downstream pattern recognition strategies. Concerning the T-station hit finding efficiencies, the Forward strategy is superior to the T seeding. This is ascribed to the Forward approach of using a wide selection window to prevent excluding correct hits. Out of the hits which are selected, the correct ones are identified by means of a Hough transform. The T seeding uses narrower selection windows, thereby reducing its hit finding efficiency, and also ignores hits from high occupancy regions, see subsection 5.2.2. Since IT hits have a better resolution than OT hits, the former might result in larger χ^2 contributions to Downstream track candidates. As the Downstream strategy allows for the removal of some hits, see subsection 5.3.6, it are predominantly IT hits which are removed. This is reflected in the lower IT hit efficiency of Downstream tracks, compared to Match and T tracks. The cause for the lower OT hit efficiency of T tracks, compared to those of the Match and Upstream strategies, has not been identified.

The hit purities as listed in table 5.8 show that the pattern recognition strategies effectively find the correct hits for a track. Impurities are formed by hits which are compatible with a group of correct hits through chance. They are taken into account when fitting the track and thereby do influence the reconstructed path of a particle, but at this purity level that influence is negligible. A possible exception is formed by the T track OT hit purity, which is lower than the other purities. In part, this accounts for the lower OT hit efficiency observed for T tracks in table 5.7.

Table 5.8: *Track-averaged hit purity for each strategy, shown for all hits together and for each hit type separately. The uncertainty on these numbers is smaller than the last presented digit.*

strategy	total ρ [%]	VELO ρ [%]	TT ρ [%]	IT ρ [%]	OT ρ [%]
Velo PR	99.0	99.0	···	···	···
Upstream PR	99.0	99.4	98.7	···	···
Forward PR	98.8	99.4	98.8	99.5	98.1
Match PR	99.0	99.5	98.8	99.7	98.4
Downstream PR	97.9	···	97.8	99.7	97.8
T PR	97.3	···	···	99.1	95.7

5.4.5 Track efficiency and alignment

The LHCb detector geometry is described in a database for use by the simulation and reconstruction software. Each detector component is located at its design position and in its design orientation, which is referred to as the ideal geometry. This level of accuracy is not realistic for the physical LHCb detector components, despite being installed as precisely as possible. An alignment mechanism exists for determining the positions and orientations of the detector elements [113], which will be used to align the detector. It is of interest to see what effects are visible in the track finding efficiency in case of misalignments.

Here, two scenarios are inspected. The first is a detector whose elements are located close to their ideal positions. Only translations in the principal bending direction (x) are implemented in this database, and the widths of the Gaussian distributions from which they were drawn are stated in table 5.9. These widths equal about a third of the track resolution of each sub-detector. This geometry is chosen to represent the result of the alignment procedure, and is referred to as the aligned geometry. A second scenario uses the geometry database of a misaligned detector, which contains both translations and rotations. The Gaussian widths which it contains are larger than those of the aligned geometry, and are listed in table 5.10.

Table 5.9: *Deviations from the ideal geometry as included in the aligned geometry. The listed numbers are the widths of Gaussian distributions from which the actual translations in x of the sub-detector modules and ladders are drawn.*

sub-detector	σ_x [µm]
VELO module	3
TT module	15
IT ladder	15
OT module	60

The track finding efficiencies, obtained when using the aligned and misaligned geometry descriptions, are given in table 5.11. Comparing these numbers to those in

Table 5.10: *Deviations from the ideal geometry as included in the misaligned geometry. The listed numbers are the widths of Gaussian distributions from which the actual translations and rotations are drawn [114].*

sub-detector	trans. σ_x [µm]	trans. σ_y [µm]	trans. σ_z [µm]	rot. σ_x [mrad]	rot. σ_y [mrad]	rot. σ_z [mrad]
VELO module	9	9	30	3	3	0.6
VELO sensor	9	9	30	3	3	0.6
TT module	50	100	50	0.05	0.5	0.3
IT box	45	45	150	0.3	0.3	0.3
OT layer	150	0	300	0.15	0.15	0.15

table 5.4 shows that the efficiencies remain almost the same when using the aligned geometry in stead of the ideal geometry. This robustness is also observed when using the misaligned geometry, with the Forward strategy being an exception. The Forward strategy is tuned to give the highest efficiency in the aligned geometry for Long tracks, while the Match algorithm is more robust against misalignments.

Table 5.11: *The event-averaged and particle-averaged efficiencies of the seeding and track finding strategies, based on reconstructible MC particles, while running the pattern recognition in filtered mode and using the aligned and misaligned detector description databases. The last row states the efficiency for finding Long tracks when combining the Forward and Match track collections. The uncertainty on these numbers is smaller than the last presented digit.*

strategy	al. EA eff. [%]	al. PA eff. [%]	misal. EA eff. [%]	misal. PA eff. [%]
Velo seeding	94.2	93.4	90.6	89.2
T-station seeding	85.7	84.9	85.4	84.6
Velo PR	70.5	70.4	62.9	62.2
Upstream PR	62.1	60.0	64.9	63.3
Forward PR	91.1	90.6	12.5	12.1
Match PR	85.9	85.4	83.3	82.7
Downstream PR	61.7	57.2	62.5	57.5
T PR	74.8	72.9	74.3	72.9
Long (F$\cup$M)	94.4	93.7	86.0	84.8

Chapter 6

Track fitting

The pattern recognition results in collections of hits, which provide the basic information from which the path of a particle is reconstructed. The hits are fitted to a model for the path, using a least-squares method called a Kalman filter, as introduced in section 6.1. First, the value of the model's parameters are estimated at the point where a particle is closest to a hit. This estimation procedure is discussed in section 6.2. The mathematical tools used for the estimation are detailed in sections 6.3, 6.4 and 6.5. Second, the hit is used to improve the values of the model's parameters, see section 6.6. These estimation and improvement operations are repeated until all hits have been processed from the first one to the last one. Identically, these operations are preformed starting from the last hit and ending at the first hit. Third, the two series of model parameter values are combined at each hit, as described in section 6.7. The resulting collection of model parameter values represent the best estimate of the path of a particle at discrete points in the LHCb detector. Finally, the free parameters of the fit are tuned, using Monte-Carlo data, as elaborated on in section 6.8.

6.1 Kalman filter fit

The hits of a track are fitted to a track model by a least-squares method. The Kalman filter formulation of a least-squares fit takes multiple scattering and energy loss into account more natural than a global least-squares fit [115]. It is therefore commonly used in high-energy physics. In filtering theory, from which the Kalman filter originates, the least-squares problem is formulated by equations which are referred to as a dynamical system. In LHCb, this dynamical system describes the position of a particle along its path through the detector. A track represents the dynamical system by a collection of states, as required by the Kalman filter. Each state parameterises the path of the particle at a specific z coordinate in the detector. The use of z as an ordering parameter is justified by the geometry of the LHCb detector, which ensures that a traversing particle results in hits at either continually increasing or continually decreasing z.

A state is composed of a state vector $\vec{x}$ and a state covariance matrix $\mathbf{C}$. The state vector contains track parameters, which specify the path of a particle around the z-position of the state:

$$\vec{x} = \begin{pmatrix} x \\ y \\ t_x \\ t_y \\ q/pc \end{pmatrix}. \tag{6.1}$$

In this equation, x and y are Cartesian coordinates, $t_x = dx/dz$ and $t_y = dy/dz$ are the track slopes, q is the charge of the particle, p is its momentum and c is the speed of light. The state covariance matrix quantifies the uncertainty in each of the track parameters and their covariance.

The Kalman filter uses the estimated values of the parameters of a state. These are based on those of one of its neighbours by the prediction operation, as detailed in the next section. In LHCb, the hits of a track are one-dimensional measurements of the path of a particle. They form the input information to the dynamical system at a number of z coordinates. Therefore, a state is predicted at the nominal z-coordinate of the layer which recorded the hit. A state and a hit are combined in a node, labelled with the z coordinate of the state. The information formed by a hit is used to improve on the predicted parameters. This process is called filtering and is detailed in section 6.6. Performing the prediction in one direction, filtering the states, performing the prediction in the opposite direction, and averaging that prediction with the filtered state parameters, see section 6.7, constitutes a fit iteration. After a number of fit iterations, as determined in section 6.8, the estimated state parameters are optimal in the sense that the Kalman filter has minimised the estimated parameter error covariances.

6.2 Prediction

A Kalman filter fit begins by predicting a state at coordinate z_k. A state at z_{k-1} is needed as input information for this prediction. Upon initialising the fit, the state at z_{k-1} is called the seed state, and is obtained from the pattern recognition procedure.

As described in the previous chapter, the pattern recognition strategies use simplified track models to group hits into tracks. In doing so, the parameters of those models are determined along the path of a particle. For tracks including Velo hits, the values of those parameters at the most upstream hit form the seed state vector. The other track types have a seed state at the most downstream T-stations hit.

As the track model used in the fit is different from those used by the pattern recognition strategies, the seed state can bias the fit. This effect is suppressed by assigning sufficiently large errors to the seed state parameters. The values of these errors are listed in table 6.1.

The predicted state vector $\vec{x}_k^{k-1}$ at z_k is obtained from a process function f evaluation of the state at z_{k-1} and is perturbed by finite variance, zero-mean process noise $\vec{w}_k$ [115]:

$$\vec{x}_k^{k-1} = f_k(\vec{x}_{k-1}) + \vec{w}_k\,. \tag{6.2}$$

Table 6.1: *Errors assigned to the seed state parameters. The error on the momentum is defined as* $\sqrt{(Aq/pc)^2 + B^2}$, with the values of A and B listed in the final two columns.

strategy	x [mm]	y [mm]	t_x	t_y	A [MeV^{-1}]	B [MeV^{-1}]
Velo PR	2	6.3	7.7 10^{-3}	1 10^{-2}	0.01	5 10^{-8}
Upstream PR	2	6.3	7.7 10^{-3}	1 10^{-2}	1.2	5 10^{-7}
Forward PR	6.3	6.3	3.2 10^{-2}	4.5 10^{-2}	0.15	5 10^{-7}
Match PR	6.3	6.3	3.2 10^{-2}	4.5 10^{-2}	0.15	5 10^{-7}
Downstream PR	6.3	6.3	3.2 10^{-2}	4.5 10^{-2}	0.15	5 10^{-7}
T PR	2	6.3	7.7 10^{-3}	1 10^{-2}	0.04	5 10^{-8}

State vector prediction and error propagation are treated in separate steps, moving the process noise term to the state covariance matrix calculation (6.5).

The process function is determined by extrapolation models, as described is section 6.3. Traversing the non-homogeneous magnetic field and material layers results in a non-linear process function. However, the original Kalman filter formulation [116] requires the process function to be linear. An extended Kalman filter addresses this issue by linearising the process function, using a first order Taylor expansion around a reference state vector $\vec{x}_{k-1}^{\text{ref}}$:

$$\vec{x}_k^{k-1} = f_k\left(\vec{x}_{k-1}^{\text{ref}}\right) + \mathbf{F}_k\left(\vec{x}_{k-1} - \vec{x}_{k-1}^{\text{ref}}\right), \tag{6.3}$$

$$\mathbf{F}_k = \frac{\partial f_k\left(\vec{x}_{k-1}^{\text{ref}}\right)}{\partial \vec{x}_{k-1}^{\text{ref}}}. \tag{6.4}$$

The reference state is chosen to be the seed state, predicted to and filtered at the previous node, with filtering defined in section 6.6. For stability and speed, both the value of the process function given the reference state and the transport matrix $\mathbf{F}$ are taken to be constants under fit iterations. They are calculated during the first fit iteration and reused for all subsequent iterations.

State prediction is an estimation of the true state vector $\vec{x}_{k,true}$. The uncertainty in the prediction is quantified by the state covariance matrix. For a predicted state vector, the covariance matrix is determined by a similarity transformation of the transport matrix and the covariance matrix of the previous state, added to the covariance matrix $\mathbf{Q}$ of the process noise $\vec{w}_{k-1}$, which consists of multiple scattering and energy loss, as calculated in subsections 6.3.6 and 6.3.7.

$$\mathbf{C}_k^{k-1} = \mathbf{F}_k\mathbf{C}_{k-1}\mathbf{F}_k^T + \mathbf{Q}_k. \tag{6.5}$$

In case there is a hit near the z-coordinate of the predicted state, the difference between the hit and the state can be determined. As the hits are one-dimensional, the state vector needs to be projected onto the hit space. The transformation of the state vector into a projected state vector or predicted hit m_k^{k-1} is given by:

$$m_k^{k-1} = h_k(\vec{x}_k^{k-1}) + \epsilon_k, \tag{6.6}$$

where h is the projection function and ϵ is the finite-variance, zero-mean hit noise.

The projection function h is determined in section 6.5 and observed to be non-linear. As done for the process function, the projection function is linearised by constructing a first-order Taylor expansion around a reference state:

$$h_k\left(\vec{x}_k^{k-1}\right) = h_k\left(\vec{x}_k^{\mathrm{ref}}\right) + \mathbf{H}_k\left(\vec{x}_k^{k-1} - \vec{x}_k^{\mathrm{ref}}\right) , \tag{6.7}$$

$$\mathbf{H}_k = \frac{\partial h_k\left(\vec{x}_k^{\mathrm{ref}}\right)}{\partial \vec{x}_k^{\mathrm{ref}}} , \tag{6.8}$$

where $\mathbf{H}$ is called the projection matrix.

In the first fit iteration, the reference state is the seed state, predicted at z_k. Subsequent iterations use the averaged state of the previous fit iteration. State averaging is explained in section 6.7.

The difference between the hit m_k and the projected state vector is called the residual $\vec{r}_k^{k-1}$ of the prediction. This is a number, as hits are one-dimensional in LHCb.

$$r_k^{k-1} = m_k - h_k\left(\vec{x}_k^{k-1}\right) . \tag{6.9}$$

This residual has uncertainties due to the process and hit noise, which for LHCb are quantified by the one-dimensional covariance matrix $\mathbf{R}$ of the residual. It is given by the sum of the covariance matrix $\mathbf{V}$ of the hit noise ϵ, and a similarity transformation of the predicted state covariance matrix and the projection matrix.

$$\mathbf{R}_k^{k-1} = \mathbf{V}_k + \mathbf{H}_k\mathbf{C}_k^{k-1}\mathbf{H}_k^T . \tag{6.10}$$

The compatibility of a predicted state at the location of a hit with the track model is quantified by the squared-error loss function χ^2. It is defined as the squared residual, normalised by the error of the residual:

$$\left(\chi^2\right)_k^{k-1} = \left(r_k^{k-1}\right)^T \left(\mathbf{R}_k^{k-1}\right)^{-1} r_k^{k-1} . \tag{6.11}$$

Since there is a set of hits for each track, the sum of the χ^2 values at those hits is used as a measure of the compatibility between the track and the track model. This compatibility is discussed in section 6.8 and chapter 7.

6.3 Extrapolation models

The prediction of a state through the inhomogeneous magnetic field of LHCb makes use of four approximate solutions of the equations of motion of subsection 6.3.1. These are the models described in subsections 6.3.2 to 6.3.5. Besides for track fitting, these models are also used for pattern recognition and in physics analyses. As the magnetic field is inhomogeneous over the detector volume, computing time can be reduced by choosing the appropriate extrapolation model for a specific task. Calculating the change of the track parameters in a region of sufficiently weak and homogeneous magnetic field, is possible with a less complicated and consequently less time-consuming model at a comparable accuracy as provided by a model which takes magnetic field effects into account in a more detailed way. Also, for short distances a more accurate model does not provide a significantly different result. Four approximations to the solution of the equations of motion are available. The track fit uses the parabolic model for extrapolations over a total distance which is less than 100 mm and otherwise the Runge-Kutta one. The effects of materials are separated into multiple scattering and energy loss, as treated in subsections 6.3.6 and 6.3.7.

6.3.1 Equations of motion

The path of a charged particle through a static magnetic field is described by equations of motion. In the absence of material effects, these are fully determined by the Lorentz force. Formulated in terms of geometrical quantities and as a function of the z-coordinate, the equations of motion are [117]:

$$
\begin{aligned}
\frac{d^2x}{dz^2} &= \frac{q}{p}\frac{ds}{dz}\left[\ \frac{dx}{dz}\frac{dy}{dz}B_x - (1+\left(\frac{dx}{dz}\right)^2)B_y + \frac{dy}{dz}B_z\right], \\
\frac{d^2y}{dz^2} &= \frac{q}{p}\frac{ds}{dz}\left[-\frac{dx}{dz}\frac{dy}{dz}B_y + (1+\left(\frac{dy}{dz}\right)^2)B_x - \frac{dx}{dz}B_z\right],
\end{aligned}
\tag{6.12}
$$

where q is the charge of the particle, p is its momentum, s is the path length and $\vec{B}$ is the local magnetic field vector.

Rewriting these equations using the track parameters results in the x and y directions and curvatures:

$$
\begin{aligned}
\frac{dx}{dz} &= t_x, \\
\frac{dy}{dz} &= t_y, \\
\frac{dt_x}{dz} &= \frac{q}{p}\sqrt{1+t_x^2+t_y^2}\left[\ t_y(t_xB_x + B_z) - (1+t_x^2)B_y\right], \\
\frac{dt_y}{dz} &= \frac{q}{p}\sqrt{1+t_x^2+t_y^2}\left[-t_x(t_yB_y + B_z) + (1+t_y^2)B_x\right].
\end{aligned}
\tag{6.13}
$$

These equations need to be integrated in order to determine the track parameters x, y, t_x and t_y at the end of a prediction step. Four approximations to that integral are detailed below and result in the process function f of equation (6.3).

6.3.2 Linear

The magnetic field integral over an extrapolation range depends on both the magnitude of the field in that region and the length of the range. In regions of negligible magnetic field strength or for sufficiently short extrapolation distances, a particle is assumed to traverse the detector in a straight line. This assumption forms the basis of the linear extrapolator. It calculates the changes in x and y, leaving the momentum and slopes t_x and t_y unchanged. The solution of the equations of motion for the geometrical track parameters in this scenario is given by:

$$
\begin{aligned}
x(z_e) &= x_0 + t_{x0}\Delta z \quad [\mathrm{mm}]\,, \\
y(z_e) &= y_0 + t_{y0}\Delta z \quad [\mathrm{mm}]\,, \\
t_x(z_e) &= t_{x0}\,, \\
t_y(z_e) &= t_{y0}\,.
\end{aligned}
\tag{6.14}
$$

The subscript 0 refers to the parameter values before propagation and $\Delta z = z_e - z_0$ is the difference between the z-position at the end and the beginning of the propagation step.

6.3.3 Parabolic

In the presence of a homogeneous magnetic field, the path of a particle is a circle. The mathematical model of a parabola is an adequate approximation of the particle's path in case of LHCb's inhomogeneous magnetic field, when dealing with relatively short propagation distances or propagation outside of the magnet, see section 4.3. The equations of motion describing a parabolic path are formulated as follows:

$$
\begin{aligned}
x(z_e) &= x_0 + t_{x0}\Delta z + \frac{1}{2}\frac{dt_{x0}}{dz}(\Delta z)^2 \quad [\mathrm{mm}]\,, \\
y(z_e) &= y_0 + t_{y0}\Delta z + \frac{1}{2}\frac{dt_{y0}}{dz}(\Delta z)^2 \quad [\mathrm{mm}]\,, \\
t_x(z_e) &= t_{x0} + \frac{dt_{x0}}{dz}\Delta z\,, \\
t_y(z_e) &= t_{y0} + \frac{dt_{y0}}{dz}\Delta z\,,
\end{aligned}
\tag{6.15}
$$

where dt_{x0}/dz_0 and dt_{y0}/dz_0 are evaluated using equation (6.13).

6.3.4 Runge-Kutta

A considerable, non-homogeneous magnetic field influences the path of a charged particle in a way that has no analytic expression of the exact solution. As seen in figure 4.4, the LHCb magnetic field inside the magnet region is non-homogeneous and strong enough to disfavour the use of a parabolic propagation model. This situation calls for a numerical solution of the track propagation equations. An iterative method using numerical integration by Runge [118] and Kutta [119] is a commonly used technique, suitable for dealing with this problem. The classical implementation is a fourth-order formulation of the approximation to an exact solution [120]. An appropriate solution for the LHCb track propagation purposes is the fifth-order Runge-Kutta method [107]. In this formulation, the track parameter vector $\vec{x}$ is complemented by the z-coordinate to from the vector $\vec{v} = (z, x, y, t_x, t_y, q/p)$, which is expanded as:

$$\begin{aligned} \vec{v}(z_e) &= \vec{v}_0 + \sum_{m=1}^{6} c_m \vec{k}^m \,, \\ \vec{k}^m &= \Delta z \frac{d}{dz}\left(\vec{v}_0 + \sum_{n=1}^{m-1} b_{mn}\vec{k}^n\right) . \end{aligned} \tag{6.16}$$

The coefficients c_m and b_{mn} are the Cash-Karp parameters [121], listed in table 6.2. The values of the coefficients are determined by matching equation (6.16) to a fifth-order Taylor expansion. This results in an accumulated error which is proportional to $(\Delta z)^6$, making this a fifth-order method. The method improves the initial estimate from a step of length Δz, by evaluating the derivatives at three other points within this interval and one point at z_e, and using those results as corrections of the initial estimate.

Table 6.2: *The Cash-Karp parameters for the adaptive fifth-order Runge-Kutta method.*

m	b					c	e
1						$\frac{37}{378}$	$\frac{2825}{27648}$
2	$\frac{1}{5}$					0	0
3	$\frac{3}{40}$	$\frac{9}{40}$				$\frac{250}{621}$	$\frac{18575}{48384}$
4	$\frac{3}{10}$	$-\frac{9}{10}$	$\frac{6}{5}$			$\frac{125}{594}$	$\frac{13525}{55296}$
5	$-\frac{11}{54}$	$\frac{5}{2}$	$-\frac{70}{27}$	$\frac{35}{27}$		0	$\frac{277}{14336}$
6	$\frac{1631}{55296}$	$\frac{175}{512}$	$\frac{575}{13824}$	$\frac{44275}{110592}$	$\frac{253}{4096}$	$\frac{512}{1771}$	$\frac{1}{4}$
n	1	2	3	4	5		

The situation can require an accuracy that may not be achieved when taking a step of length Δz. The error $\vec{\delta}$ on $\vec{x}(z_e)$ is estimated from the difference in the fifth (c_m) and fourth (e_m) order R-K results:

$$\vec{\delta} = \sum_{m=1}^{6}(c_m - e_m)\vec{k}^m \,. \tag{6.17}$$

The x and y components of the predicted state vector are to differ less than 5 μm between fifth and fourth order, otherwise the step is redone, using half the step-length.

6.3.5 Kisel

An alternative approach to the numerical Runge-Kutta method is described in [122]. As their results are similar, only the Runge-Kutta method is used in the track reconstruction. The solution of Kisel is based on the possibility to expand the track parameters that are being propagated in a power series of the magnetic field components. Like the Runge-Kutta formulation, this approach is valid in the presence of an inhomogeneous magnetic field. The inhomogeneity is taken into account by the coefficients of the power series expansion.

The magnetic field components are observed to be small parameters in the expansion [122], resulting in little dependence on the field shape. This feature also allows for higher-order terms of the power series to be neglected without it having a significant impact on the obtained result. In the expansion, same-order terms have vastly different weights. This implies that for a specific order of the expansion, using the few terms with a relatively high weight is sufficient to represent the contribution of that order to the result of the propagation. The desired precision of this model can be controlled by the number of orders taken into account.

The slopes t_x and t_y can be obtained to any order (n) from the following equation, constructed by expressing the derivatives of the slopes as power series expansions of the magnetic field components with the previous order derivative as coefficient, when substituted for T [122]:

$$\begin{aligned} T(z_e) = T(z_0) + \sum_{k=1}^{n} \sum_{i_1,\ldots,i_k} & T_{i_1,\ldots,i_k}(z_0) \\ & \cdot \left(\int_{z_0}^{z_e} B_{i_1}(z_1) \ldots \int_{z_0}^{z_{k-1}} B_{i_k}(z_k) dz_k \ldots dz_1 \right) \\ & \qquad + O\left(\frac{(B(q/p)\Delta z)^{n+1}}{(n+1)!} \right), \end{aligned} \tag{6.18}$$

where the last term in this equation provides an estimate of the propagation error in t_x and t_y, being of order $(n+1)$.

Once the track slopes have been determined, the change in the x and y parameters can be calculated by respectively integrating t_x and t_y, given by (6.18), over the propagation range in z:

$$\begin{aligned} x(z_e) &= x(z_0) + \int_{z_0}^{z_e} t_x(z) dz + O\left(\frac{(B(q/p)\Delta z)^{n+1}}{(n+1)!} \right) \Delta z \,, \\ y(z_e) &= y(z_0) + \int_{z_0}^{z_e} t_y(z) dz + O\left(\frac{(B(q/p)\Delta z)^{n+1}}{(n+1)!} \right) \Delta z \,. \end{aligned} \tag{6.19}$$

6.3.6 Multiple scattering

A particle experiences multiple scattering in a material layer, as discussed in section 4.4. In case of a thin material layer, the scattering changes the angles without significantly affecting the particle's displacement. This is due to the limited distance that it travelled, which does not allow the angular changes to significantly influence the x and y coordinates. This scenario is modelled by adding contributions to the t_x and t_y variances and their covariance in the state covariance matrix, reflecting the reduced knowledge of the particle's direction. These additions are made in the middle of a material layer [123], which results in a prediction step being split into several steps. The steps which traverse a material layer include process noise, see equation (6.5):

$$\begin{aligned}
\mathbf{Q}(2,2) &= (1+t_x^2)(1+t_x^2+t_y^2)\theta_0^2\,, \\
\mathbf{Q}(3,3) &= (1+t_y^2)(1+t_x^2+t_y^2)\theta_0^2\,, \\
\mathbf{Q}(2,3) &= t_x t_y(1+t_x^2+t_y^2)\theta_0^2\,.
\end{aligned} \tag{6.20}$$

The angular distribution corresponding to multiple Coulomb scattering is taken to be the one derived by Molière [87]. Its approximate projected angle distribution is fitted by a Gaussian. The quantity θ_0 is the root-mean-squared of that fit, and is given by the Highland-Lynch-Dahl formula [91]:

$$\theta_0 = \frac{13.6\text{ MeV}}{\beta pc}\sqrt{\frac{\Delta z\sqrt{1+t_x^2+t_y^2}}{X_0}}\left[1+0.038\ln\left(\frac{\Delta z\sqrt{1+t_x^2+t_y^2}}{X_0}\right)\right]\,. \tag{6.21}$$

The variable $\beta = v/c$ refers to the particle's velocity, p to its momentum, Δz is the distance in z and X_0 is the radiation length of the traversed material.

In case of an extended material layer, the effect of the change of angles on the propagated position of the particle can no longer be ignored. For a thick scatterer, the covariance matrix of equation (6.5) gets additions as defined by the following [123]:

$$\mathbf{Q} = \begin{pmatrix}
\mathbf{Q}(2,2)\frac{(\Delta z)^2}{3} & \mathbf{Q}(2,3)\frac{(\Delta z)^2}{3} & \mathbf{Q}(2,2)\frac{D\Delta z}{2} & \mathbf{Q}(2,3)\frac{D\Delta z}{2} & 0 \\
\mathbf{Q}(2,3)\frac{(\Delta z)^2}{3} & \mathbf{Q}(3,3)\frac{(\Delta z)^2}{3} & \mathbf{Q}(2,3)\frac{D\Delta z}{2} & \mathbf{Q}(3,3)\frac{D\Delta z}{2} & 0 \\
\mathbf{Q}(2,2)\frac{D\Delta z}{2} & \mathbf{Q}(2,3)\frac{D\Delta z}{2} & \mathbf{Q}(2,2) & \mathbf{Q}(2,3) & 0 \\
\mathbf{Q}(2,3)\frac{D\Delta z}{2} & \mathbf{Q}(3,3)\frac{D\Delta z}{2} & \mathbf{Q}(2,3) & \mathbf{Q}(3,3) & 0 \\
0 & 0 & 0 & 0 & 0
\end{pmatrix}, \tag{6.22}$$

where the error matrix elements $\mathbf{Q}(\cdots,\cdots)$ are given by equations 6.20 and D is a sign signifying the track direction, being positive for tracks propagating in increasing z. By default, all material layers in LHCb are considered to be thick scatterers.

6.3.7 Energy loss

In addition to scattering, a particle traversing material also loses energy, as detailed in section 4.5. This energy loss by ionisation is accurately described by the Bethe-Bloch equation (4.12). When all particles are considered to be minimum ionising particles, the β dependence in the Bethe-Bloch equation can be ignored. In that case the energy loss is given by:

$$\Delta E = -c_{\text{ion}}\frac{Z}{A}\rho l \quad [\text{MeV}]\,, \tag{6.23}$$

where c_{ion} is an energy loss factor, representing the constants of the Bethe-Bloch equation, Z and A are the atomic number and mass of the material, ρ is the material's density and l is the distance traversed through the material.

Landau fluctuations in the energy loss are small compared to the momentum resolution of the detector, eliminating the need to apply corrections to the track covariance matrix [58]. The change in the particle's energy is taken into account by correcting the track's momentum parameter:

$$\begin{array}{lc} \dfrac{q}{p}(z_e) = \dfrac{1}{(p/q)_0 \pm \delta} & \begin{array}{c} \left(\frac{q}{p}\right)_0 > 0 \rightarrow + \\ \left(\frac{q}{p}\right)_0 \leq 0 \rightarrow - \end{array} \\ \delta = \pm c_{\text{ion}} \frac{Z}{A} \rho \Delta z \sqrt{1 + t_{x0}^2 + t_{y0}^2} & \begin{array}{c} \text{step opposite to particle's direction} \rightarrow + \\ \text{step in particle's direction} \rightarrow - \end{array} \end{array} . \tag{6.24}$$

The energy loss of electrons is treated with a separate model. Rather than ionisation, bremsstrahlung is the dominant cause of energy loss for electrons. This is described by the Bethe-Heitler equation (4.10). The average change in energy from a starting energy E_0, when traversing a material layer is given by:

$$< \Delta E >= -E_0 \left(1 - e^{-l/X_0}\right) \quad [\text{MeV}] . \tag{6.25}$$

where l is the distance travelled through a material layer and X_0 is the radiation length.

For electrons, both the momentum and its variance are updated at the end of a prediction step through material [123]:

$$\begin{array}{lc} \dfrac{q}{p}(z_e) = \left(\dfrac{q}{p}\right)_0 \cdot e^{\pm \frac{\Delta z}{X_0} \sqrt{1 + t_{x0}^2 + t_{y0}^2}} & \begin{array}{c} \text{z decreasing} \rightarrow - \\ \text{z increasing} \rightarrow + \end{array} \\ \mathbf{Q}(4,4) = \left(\dfrac{q}{p}\right)_0^2 \cdot \left(e^{\pm \frac{\Delta z}{X_0} \frac{\ln 3}{\ln 2} \sqrt{1 + t_{x0}^2 + t_{y0}^2}} - e^{\pm 2 \frac{\Delta z}{X_0} \sqrt{1 + t_{x0}^2 + t_{y0}^2}} \right) & \end{array} . \tag{6.26}$$

6.4 Trajectories

In tracking studies before those presented in this thesis, an idealised detector geometry was used, as discussed in subsection 5.4.5. It assumed that all detector layers were positioned vertically, while in reality the detectors upstream of the magnet are under a 3.6 mrad angle with the vertical, placing them orthogonal to the beamline. The assumption of vertical detectors was used when propagating a state to the next node, effectively propagating to the nominal z-coordinate of a detector layer. The present fit propagates to the detector layer of the next hit, irrespective of its positioning. Upon combining a hit with a predicted state, described as filtering in section 6.6, the detector geometry is used when projecting a state onto the one-dimensional space of a hit. Assumptions were made on the geometry, for instance the OT modules were taken to be flat, while in reality they are observed to be somewhat curved [124]. Also, the silicon sensors of the TT and IT are warped to some degree. These and future deviations from the design detector geometry could not be taken into account by the track fit up to now. The present track fit makes none of the described assumptions on the detector geometry and is able to take all detector layer shapes into account. It uses an interpretation layer to separate the track fit mathematics from the specific detector geometry, preventing the need to change the former when alterations are made to the geometry. The interpretation layer is based on the concept of trajectories, as introduced in the BaBar experiment software [125].

Trajectories [126] are objects that serve to decouple the track reconstruction software from the specific implementation of the detector geometry description. To this end, a trajectory contains geometrical information regarding the detector element, being its location, size and shape. A trajectory can thus be visualised as a curve in global coordinate space. Using the information it contains, a trajectory can determine a second-order Taylor expansion at any point along its length. This expansion is used as the input of geometry information to the track fit. As it is always a parabolic approximation, the fit becomes effectively independent of reasonable changes in the shape and orientation of detector elements.

The track fit predicts a state at the nominal z-coordinate of the detector element that recorded the hit which will be filtered. This hit is a one-dimensional measurement, so without additional information it is not known where along the strip or wire the hit was created. In addition, the strip or wire in general does not reside in a plane at a single z-position. A hit can therefore be geometrically seen as a curve in space with the shape of the hit strip or wire, which is the definition of a trajectory. The predicted state can be viewed as a local tangent to the path of the particle, combined with momentum and charge information. This allows for the state also to be considered as a trajectory, containing the shape of the path of the particle.

Currently, VELO ϕ, TT and IT strips as well as the OT wires are currently modelled as straight lines. VELO R strips are currently described as circle sections. For the silicon sensors, the hit-trajectories are shaped as a strip, and located at the centre of charge of the hit. The OT hits have their trajectories represent the wires themselves, as the drift distance is determined at a later point during the fit. A state has the track locally represented by a parabola in a state-trajectory.

A trajectory contains an inherent shape, being a straight line, a circle section or a parabola. Each trajectory has a point of origin in space, from which the length along its shape is referred as the arc-length[1] s. The arc-length can have a positive or negative value and may be limited within a range, for example for the length of an OT wire. At any value of the arc-length, the position, direction and curvature vectors of the shape are available. These are the zeroth-, first- and second-order derivatives of the shape with respect to the arc-length.

6.4.1 Distance minimisation

The trajectories of states and of hits are used to project the state onto the hit space, as described in section 6.5. As part of that calculation, the arc-lengths s_s and s_m along the state- and hit-trajectories are used. These arc-lengths specify the locations where the trajectories are closest to each-other. These points of closest approach are determined in a generic way, as all trajectories provide parabolic approximations to their

[1]Post DC06, state trajectories are parameterised using the z-coordinate, not the arc-length.

shapes. The arc-lengths to the points of closest approach are found by a distance minimisation in three dimensions. This minimisation is an iterative procedure, initialised by obtaining parabolic expansions at the starting values of the arc-lengths. The minimal distance a between these parabolas is calculated, resulting in two arc-lengths s_1 and s_2 travelled along the parabolas. The distance vector $\vec{l}$ between the shapes contained within the state- and hit-trajectories is then determined between points on the shapes at $s_s = s_1$ and $s_m = s_2$. This process is illustrated in figure 6.1.

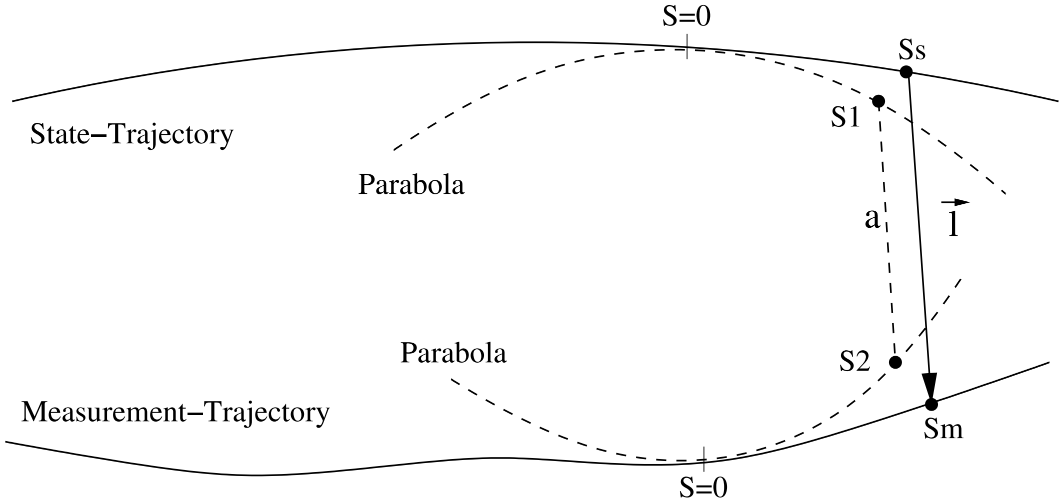

Figure 6.1: *Determination of the distance of closest approach $|\vec{l}|$, between points at arc-lengths $s_s = s_1$ and $s_m = s_2$. The difference between the parabolic expansion and the trajectory's shape is exaggerated for visibility.*

The minimum distance is found when the change in s_s and s_m over an iteration is less than a hit-dependent tolerance, as specified in section 6.5. The parabolic approximations describe shapes sufficiently accurate to have the minimum located in typically one iteration.

During the minimisation process, sanity checks are performed on the results as self-monitoring. These checks are aimed at intercepting minimisation attempts involving trajectories that are (almost) parallel. Minimisations that are diverging are stopped automatically as well. In case of oscillations around a minimum, the pair of arc-lengths resulting in the shorter distance $|\vec{l}|$ of the two, is selected as the proper result.

6.5 Projection

Hits are one-dimensional measurements of the path of a charged particle. In order to combine a five-dimensional state vector with a hit, the state vector must first be projected as given by equation (6.6). The determination of the required projection matrix **H** is discussed in this section.

A node with both a state and a hit also contains the associated residual r and residual covariance matrix R. The tracking sub-detectors provide one-dimensional measurements of a particle's path, which makes the residual and its covariance matrix scalars. Their values are determined by using trajectories.

A state-trajectory is constructed from the parameters of a state and the local magnetic field vector, which determines the curvature. Each hit can provide a trajectory which represents it. For OT hit-trajectories, the drift-distance and the propagation time along the wire can be calculated when the arc-length along the hit's trajectory has been determined.

The arc-lengths along the trajectories of the state and the hit to the points in space where the trajectories are closest to each-other are determined using the minimisation tool of subsection 6.4.1. As a starting value for the arc-length s_m of the hit-trajectory, the arc-length where it is closest to the state is used. The arc-length starting value s_s of the state-trajectory is set to zero. Given this information, the minimisation process determines the minimum distance between the trajectories and the corresponding arc-lengths s_s and s_m, as described in subsection 6.4.1. The minimum distance is identified to within an arc-length tolerance of 10 µm for the OT or 2 µm for the silicon sensor hits. The distance is made available as a vector $\vec{l}$, pointing in three dimensions from the state-trajectory to the hit-trajectory.

At first, the reference vector of equation (6.6) is projected. In that equation $\vec{x}_k^{\mathrm{ref}}$ is equal to $\vec{x}_k^{k-1}$, reducing $h_k\left(\vec{x}_k^{k-1}\right)$ to $h_k\left(\vec{x}_k^{\mathrm{ref}}\right)$. Therefore the residual of equation (6.9) is equal to $|\vec{l}|$. The subsequent projection of the predicted state uses this value, corrected by the first-order Taylor term of equation (6.6):

$$r_k^{k-1} = r_k^{\mathrm{ref}} + \mathbf{H}_k\left(\vec{x}_k^{k-1} - \vec{x}_k^{\mathrm{ref}}\right) . \tag{6.27}$$

The projection matrix $\mathbf{H}_k$ is used to determine the change in the residual, due to a difference in the state parameters of the reference state and the predicted state. It is calculated as the dot product of the direction of the residual $\hat{p}$ with the derivative of the position of the state-trajectory of the reference state at arc-length s_s with respect to the state parameters $\mathbf{D}$: $\mathbf{H} = \hat{p} \cdot \mathbf{D}$.

The projection vector $\vec{p}$, which contains the direction of the residual, is given by the cross-product of the hit-trajectory direction with the state-trajectory direction: $\vec{p} = \vec{m} \times \vec{t}$. At arc-length s_s, the derivative of the state-trajectory's shape with respect to the arc-length s is taken, resulting in the vector $\vec{t}$:

$$\vec{t} = \frac{d\mathbf{x}(s=0)}{ds} + s_s \frac{d^2\mathbf{x}(s=0)}{ds^2} . \tag{6.28}$$

The Cartesian coordinates are represented by the vector $\mathbf{x}$. Analogously, the vector $\vec{m}$ is obtained for the hit-trajectory at arc-length s_m.

The derivative matrix $\mathbf{D}$ contains the derivative of the trajectory's position, at arc-length s_s, with respect to the state parameters:

$$\mathbf{D} = \frac{d\left(\mathbf{x}(s_s) + s_s \dfrac{d\mathbf{x}(s_s)}{ds} + 0.5 s_s^2 \dfrac{d^2\mathbf{x}(s_s)}{ds^2}\right)}{d\vec{x}} . \tag{6.29}$$

For alignment purposes, the derivative in the definition of $\mathbf{D}$ can be replaced by a derivative with respect to a set of alignment parameters, whose optimal values are thereby estimated.

In case the OT drift-distance is not determined, a choice made for the prefit iterations in subsection 6.8.2, the above calculation is also used for OT hits. Otherwise, the measured time is corrected for the time the signal takes to travel along the wire from the position at arc-length s_m to the read-out electronics. The remaining time is converted into a drift-distance l_{drift}, which represents the measured distance from the path of the particle to the OT wire. A track can pass the OT wire either on the left or on the right, as seen in the xy plane. The choice for left or right is signified by a sign, called the L/R sign and quantified as $lr = \pm 1$. It is determined by the reference state of equation (6.7) being on one side of the wire. The residual r_k^{k-1} is determined from $\vec{l}$ and the drift-distance as:

$$r_k^{k-1} = -\left(|\vec{l}| - lr \cdot l_{\text{drift}}\right) , \tag{6.30}$$

where the signs take into account whether the reference state and the state that is being projected are on the same side or on opposite sides of the wire.

The error on the residual, contained within the residual covariance matrix $\mathbf{R}$ of equation 6.10, is the square-root of the hit error ϵ. Projecting a state onto the OT hit space without using the drift-time in the calculation, increases the error on the residual to the square-root of a third of the drift-tube radius squared.

6.6 Filtering

Once a state is predicted at the z-coordinate of a hit, the information of that hit is used to improve the estimate of the state. This procedure is known as filtering the state. The filtered state vector $\vec{x}_k$ is obtained by adding the weighted residual of the prediction step to the predicted state vector $\vec{x}_k^{k-1}$:

$$\vec{x}_k = \vec{x}_k^{k-1} + \mathbf{K}_k r_k^{k-1} . \tag{6.31}$$

The Kalman gain matrix $\mathbf{K}_k$ determines the weight of the predicted residual r_k^{k-1}, based on the covariance matrices of the predicted state vector ($\mathbf{C}_k^{k-1}$) and of the hit noise ($\mathbf{V}_k$). It is calculated such as to minimise the filtered covariance matrix $\mathbf{C}_k$ [116]:

$$\mathbf{K}_k = \mathbf{C}_k^{k-1}\mathbf{H}_k^T \left(\mathbf{V}_k + \mathbf{H}_k\mathbf{C}_k^{k-1}\mathbf{H}_k^T\right)^{-1} = \mathbf{C}_k^{k-1}\mathbf{H}_k^T \left(\mathbf{R}_k^{k-1}\right)^{-1} . \tag{6.32}$$

With the information contained in the hit, the uncertainty in the estimate of the state vector is reduced. The predicted state covariance matrix $\mathbf{C}_k^{k-1}$ decreases by a factor which is determined by the Kalman gain matrix $\mathbf{K}_k$, resulting in the filtered state covariance matrix $\mathbf{C}_k$:

$$\mathbf{C}_k = \left(\mathbb{1} - \mathbf{K}_k\mathbf{H}_k\right)\mathbf{C}_k^{k-1} . \tag{6.33}$$

After filtering, the state vector $\vec{x}_k$ differs from the predicted one ($\vec{x}_k^{k-1}$), and thereby the residual has changed. Similar as to the filtered state covariance matrix $\mathbf{C}_k$ of equation (6.33), the filtered residual r_k is obtained from the predicted residual r_k^{k-1} by deducting a one-dimensional gain matrix scaled factor:

$$r_k = m_k - h_k\left(\vec{x}_k\right) = \left(1 - \mathbf{H}_k\mathbf{K}_k\right) r_k^{k-1} . \tag{6.34}$$

The filtered residual covariance matrix $\mathbf{R}_k$ is determined as the hit noise covariance matrix $\mathbf{V_k}$, reduced by a similarity transformation of the projection matrix $\mathbf{H}_k$ and the filtered state covariance matrix $\mathbf{C}_k$:

$$\mathbf{R}_k = (\mathbb{1} - \mathbf{H}_k\mathbf{K}_k)\,\mathbf{V}_k = \mathbf{V}_k - \mathbf{H}_k\mathbf{C}_k\mathbf{H}_k^T\,. \tag{6.35}$$

Compared to the predicted residual covariance matrix $\mathbf{R}_k^{k-1}$ of equation (6.10), the plus sign is changed into a minus sign, as the inclusion of hits in the filtered state covariance matrix anti-correlates it.

A filtered state is on average expected to be closer to the particle's path than the predicted state and more precisely determined. This implies a reduced residual and residual error. The resulting χ^2 of the filtered state is identical to the χ^2 of the predicted one.

6.7 Averaging

A filtered state represents the particle's path at its z-coordinate as well as possible within the constraints of the chosen track and propagation models, and the hits available up to and including the one of the present node. All hit information at further z-positions is not included in the estimation of the state. As a result, the state at the final hit is a more accurate estimate of the path than the first state is. There are two ways to resolve this imbalance. First, it is possible to perform the filter in the reverse direction, using the final filtered state as a starting point. This implies that all hits downstream of a reverse filtered state are used twice in the estimation of that reverse filtered state. Therefore a correction is applied to the reverse filtered state, a procedure which is known as Kalman smoothing [116]. Second, a more efficient alternative is to execute the prediction in the reverse direction and combine its results with those of the forward filter step, as described in this section. This bi-directional filter [125] is executed by default in the LHCb track reconstruction software.

A smoothed state vector $\vec{x}_k^n$ is determined as the weighted mean of the downstream filtered state vector $\vec{x}_k$ and the upstream propagated state vector $\vec{x}_k^{k+1}$:

$$\vec{x}_k^n = (\mathbf{C}_k)^{-1}\,\mathbf{C}_k^n\vec{x}_k + \left(\mathbf{C}_k^{k+1}\right)^{-1}\mathbf{C}_k^n\vec{x}_k^{k+1}\,. \tag{6.36}$$

The smoothed state covariance matrix $\mathbf{C}_k^n$ is calculated from the downstream filtered and upstream propagated covariance matrices $\mathbf{C}_k$ and $\mathbf{C}_k^{k+1}$ as:

$$\mathbf{C}_k^n = \mathbf{C}_k\left(\mathbf{C}_k + \mathbf{C}_k^{k+1}\right)^{-1}\mathbf{C}_k^{k+1}\,. \tag{6.37}$$

Taking the weighted mean of the downstream filtered state vector $\vec{x}_k$ and the upstream propagated state vector $\vec{x}_k^{k+1}$ is intended to reduce the filtered residual r_k, resulting in the smoothed residual r_k^n:

$$r_k^n = m_k - h_k\left(\vec{x}_k^n\right) = r_k + \mathbf{H}_k\left(\vec{x}_k - \vec{x}_k^n\right)\,. \tag{6.38}$$

The smoothed residual covariance matrix $\mathbf{R}_k^n$ is determined as the difference between the hit noise covariance matrix $\mathbf{V}_k$ and a similarity transformation of the projection matrix $\mathbf{H}_k$ and the smoothed state covariance matrix $\mathbf{C}_k^n$:

$$\mathbf{R}_k^n = \mathbf{V}_k - \mathbf{H}_k \mathbf{C}_k^n \mathbf{H}_k^T \,. \tag{6.39}$$

The compatibility of a fitted track with the track model is quantified by the sum of the smoothed state χ^2 contributions[2], divided by the number of degrees of freedom. That number is equal to five times the number of states, minus the number of hits. The smoothed state χ^2 contribution is defined as:

$$\left(\chi^2\right)_k^n = r_k^n \left(\mathbf{R}_k^n\right)^{-1} r_k^n \,. \tag{6.40}$$

6.8 Tuning

The track fit procedure includes a number of free parameters that must be tuned, in order to obtain the optimal performance. The tuned parameters are: the number of fit iterations (6.8.1), the number of prefit iterations (6.8.2), the number of hits that are allowed to be removed from the fitting process (6.8.3), and the ionisation energy value c_{ion} (6.8.4). As quality control observables, the χ^2 per degree of freedom, the fraction of correctly determined OT L/R signs, and the mean of the momentum pull distribution are used.

6.8.1 Fit convergence

The track parameter estimation process is constrained by the track model and the hits. As a measure of the compatibility between the hits and the track model, the $\chi^2/\mathrm{n_{DOF}}$ of equation (6.40) is used. Its variation from iteration to iteration of the fit reduces asymptotically, and when it changes by less than 0.1, the track fit is defined to have converged at the previous iteration. At that point, the fitted track contains the optimal estimates of the track parameters. In the LHCb track fit, the number of iterations is a separate constant for each of the track collections that are found by the pattern recognition strategies. This approach is referred to as the fixed number method, and the values of its constants are determined next.

The fraction of tracks for which the fit has converged is shown as a function of the number of executed fit iterations in figure 6.2. For tracks from each of the pattern recognition strategies, the fraction of converged fits increases at different rates towards 100%. The fixed number of iterations is determined from this as the iteration at which at least 95% of the fits have converged. This procedure results in the values shown in the first column of table 6.3, which in its second column lists the corresponding percentages of converged track fits. These numbers leave room for improvement, as discussed in the remainder of this subsection.

[2] Post DC06 the filtered χ^2 is used, as the smoothed residuals contain information from both upstream and downstream hits, making them correlated and the equation (6.39) not describe a contribution to a χ^2 distribution.

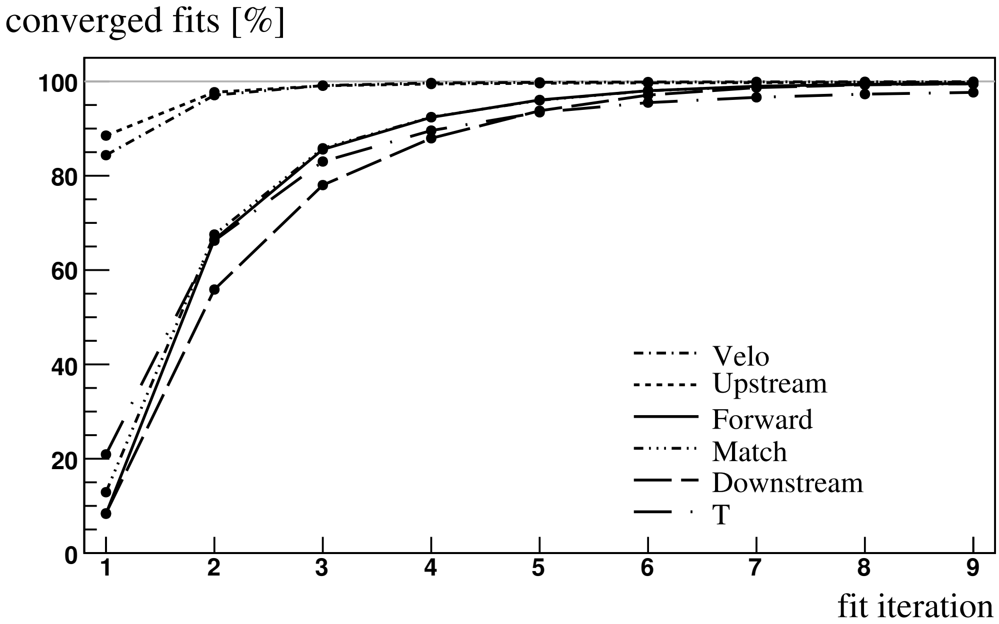

Figure 6.2: *The percentage of converged track fits as a function of the number of performed fit iterations, split by pattern recognition strategy.*

An alternative to the fixed number method is inspecting the change in χ^2/n_{DOF} of each track from iteration to iteration, in order to determine fit convergence. This approach is called the monitoring method, and is not performed by the LHCb track fit. Such an approach requires one iteration more than needed for convergence, being the one for which the χ^2/n_{DOF} changed by less than 0.1. In addition, a maximum number of iterations is needed to account for slowly converging fits and to prevent indefinite iteration for diverging fits.

For comparison with the fixed number method, the required number of fit iterations by a track fit which monitors for stability is determined. It is calculated as the sum over nine iterations, weighted by the percentages of fits which became stable at those iterations. The number nine is the maximum number of allowed fit iterations, and the percentages used as weights are deduced from those shown in figure 6.2. In addition, the iteration needed to ascertain convergence is added to the weighted mean number of required iterations.

The resulting numbers of iterations, and the corresponding fractions of converged fits, are shown in the third and fourth column of table 6.3. The monitoring method requires 30–40% fewer iterations than the fixed number method for all but Velo and Upstream tracks, which need 10% more iterations. Using the event-averaged number of tracks per pattern recognition strategy from table 5.1, the mean number of fit iterations for the fixed number method is 4.1±0.05, whereas it is 3.0±0.05 for the monitoring method. The monitoring method therefore reduces the overall amount of fit iterations by 27%. It also results in higher percentages of stable fits, as seen in table 6.3, since it allows a fraction of the track fits to exceed the number of iteration found by the fixed number method, up to a maximum of nine. These percentages are compatible with 100%, within their errors. For these rea-

Table 6.3: *The number of fit iterations and percentage of converged fits for the fixed number and monitoring methods, split by the pattern recognition strategies which found the tracks. The uncertainty on these numbers is smaller than the last presented digit.*

	fixed number		monitoring	
PR strategy	# iter.	converged [%]	# iter.	converged [%]
Velo	2	97.1	2.2	99.9
Upstream	2	97.7	2.2	99.8
Forward	5	96.1	3.5	99.6
Match	5	96.0	3.5	99.5
Downstream	6	97.1	3.8	99.5
T	6	95.5	3.5	97.7

sons, the monitoring method can be implemented as an improvement of the LHCb fit. Note that the maximum number of fit iterations, set to nine in this example, has not been optimised.

6.8.2 OT L/R sign

An Outer Tracker hit contains a drift distance and a L/R sign, the latter signifying on which side of the hit wire the particle is estimated to have passed, as introduced in section 6.5. This sign is the result of the L/R sign estimation of the fit, and can be checked for correctness using the Monte-Carlo information. As the L/R sign is determined by the averaged state of the previous iteration, a correct L/R sign at the end of n iterations indicates the need for at most $n-1$ iterations. In case $n = 1$, the L/R sign is determined by the predicted seed state, as there is no averaged state available when $n - 1 = 0$ fit iterations have been performed. An exception on this is formed by T tracks, for which the L/R sign is calculated during the T seeding, rather than being determined by the predicted seed state.

As Velo and Upstream tracks do not contain OT hits, they are not under consideration here. For the other tracks, the fraction of correct L/R sign estimates is determined for one to nine fit iterations. The fraction of correct L/R sign estimates is determined per track and then averaged over all tracks. In figure 6.3, the resulting fractions are shown, as a function of the iteration which determined the L/R signs, for tracks of the various pattern recognition strategies. For tracks from the Forward, Match and Downstream strategies, the fractions are around 64% when they are determined by the predicted seed state. Fit iterations improve these fractions, which are observed to approach asymptotes. Barred a barely visible 0.2% dip at the first iteration, the fraction for T tracks is insensitive to fit iterations. This indicates that the L/R signs which are estimated during the T seeding are not improved upon by the fit.

Based on their asymptotic behaviour, the fractions are defined to be stable when the next iteration changes them by less than 0.1%. The number of iterations needed

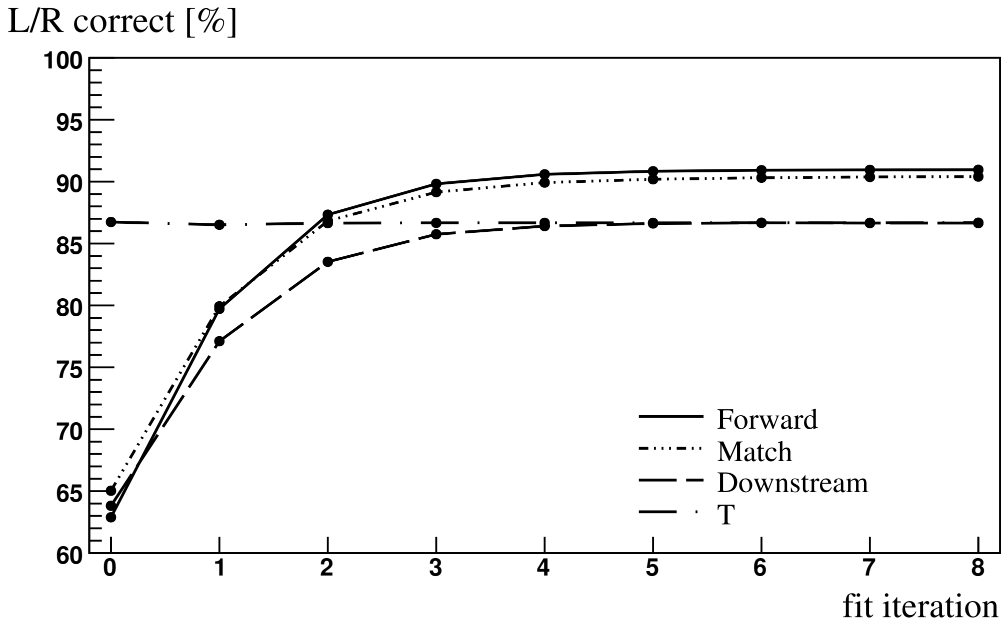

Figure 6.3: *The average percentage of correctly assigned OT L/R signs, as a function of the fit iteration which determined those signs, split by pattern recognition strategy.*

to achieve stability, as well as the values of the fractions are listed in the first column of table 6.4. The number of required iterations for the Long tracks is higher than needed for χ^2/n_{DOF} stability, which is one less, as seen from table 6.3. In addition, all of the fractions have values which are lower than expected. The 80 μm resolution of the track fit in the OT drift-tubes, see subsection 7.3, accounts for about 2% of the incorrect L/R assignments. Another 0.8–2.1% is caused by hits which are not due to the particle under consideration, see the hit purities in table 5.8. They have a 50% statistical probability of being fitted on the track with the correct L/R sign. This leaves another 6.1–10.3% unaccounted for, which is addressed by introducing prefit iterations, as described next.

The OT projection can be performed without determining the drift-time in a straw, see subsection 6.5. This increases the hit error from 200 μm to 1.44 mm (pitch/$\sqrt{12}$), making the OT hit less restrictive on the track. Effectively, the L/R sign information is not used by the fit in this scenario. As the L/R ambiguity is a non-linear element in equation 6.7, eliminating it makes the linearisation a better approximation. This results in the fraction of correct L/R signs to become stable in fewer iterations. Regular fit iterations are needed afterwards, to include the actual precision of the OT hits. Therefore, the iterations without using drift-time information are referred to as prefit iterations. In figure 6.4, the effect of one to nine prefit iterations on the fraction of correct L/R signs is shown.

All of the considered groups of tracks reach a stable fraction of correct L/R signs after one prefit iteration. In the case of T tracks, the effect of increasing the OT hit errors on the fraction is negative. This indicates that the model used by the T-station seeding is more accurate than the track model of the fit with artificially increased

Table 6.4: *Results obtained for the scenarios in which only fit iterations, only prefit iterations, and both prefit and fit iterations are performed. The number of iterations required for stability and corresponding fractions of correctly estimated L/R signs are shown, per scenario, in the same column. The uncertainty on these numbers is smaller than the last presented digit.*

PR strategy	# fit iterations	# prefit iterations	# prefit and fit iterations
Forward	6	1	1+3
Match	6	1	1+3
Downstream	5	1	1+3
T	2	1	···
PR strategy	correct fraction [%]	correct fraction [%]	correct fraction [%]
Forward	90.9	90.7	94.9
Match	90.3	93.0	95.3
Downstream	86.6	88.9	92.7
T	86.6	80.0	···

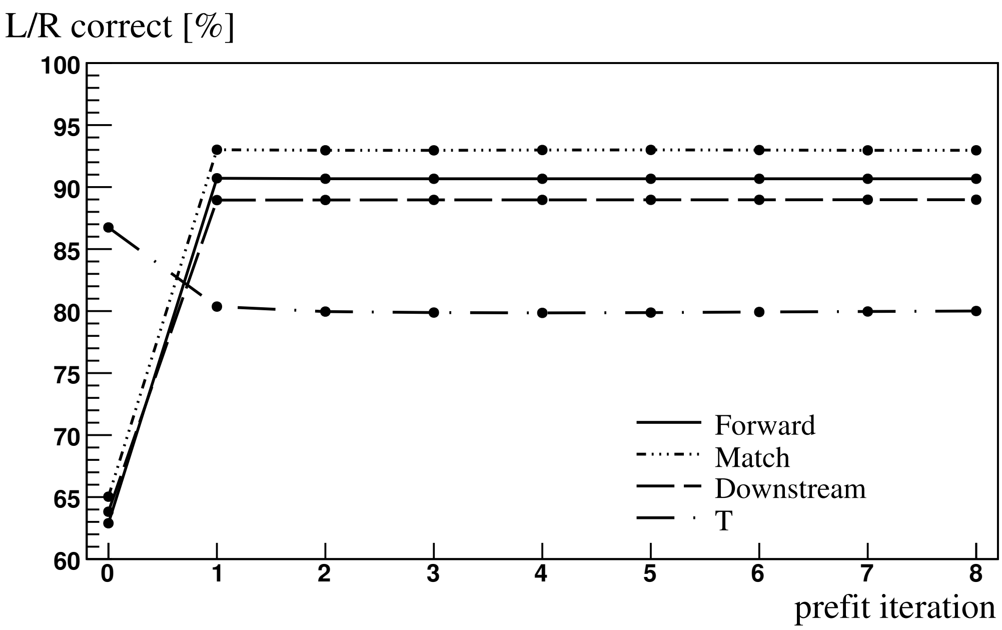

Figure 6.4: *The average percentage of correctly assigned OT L/R signs, as a function of the prefit iteration which determined those signs, split by pattern recognition strategy.*

hit errors. Prefit iterations are therefore not used for those tracks in the final track fit. The stable fractions are shown in the second column of table 6.4.

Downstream tracks have a stable fraction which is 2.3% higher than that after regular fit iterations and is obtained in four fewer iterations. Forward and Match Long tracks reach correct fractions which are respectively 0.2% and 0.3% lower than the stable fractions obtained by regular iterations, but achieved in five fewer iterations. The observed losses are compensated when performing regular fit iterations after the single prefit iteration.

The prefit iteration needs to be combined with regular fit iterations in order to make use of the accuracy of OT hits in determining the optimal estimate of the track parameters. Performing regular fit iterations after the prefit iteration results in the fractions that are shown in figure 6.5. These fractions are seen to improve up to their stable points. Those are located at a total of four iterations for all considered types of tracks, as stated in the third column of table 6.4, which also lists the fractions. The fractions are 4.0–6.1% higher than those found without using the prefit iteration, being the ones in the first column of table 6.4, and are obtained in 1–2 fewer iterations. Taking into account the 2% and 0.8–2.1% expected losses due to the OT resolution and the hit impurities, little further improvement for the fractions of the Long tracks are expected from the fit, whereas the Downstream tracks have 4.2% unaccounted for.

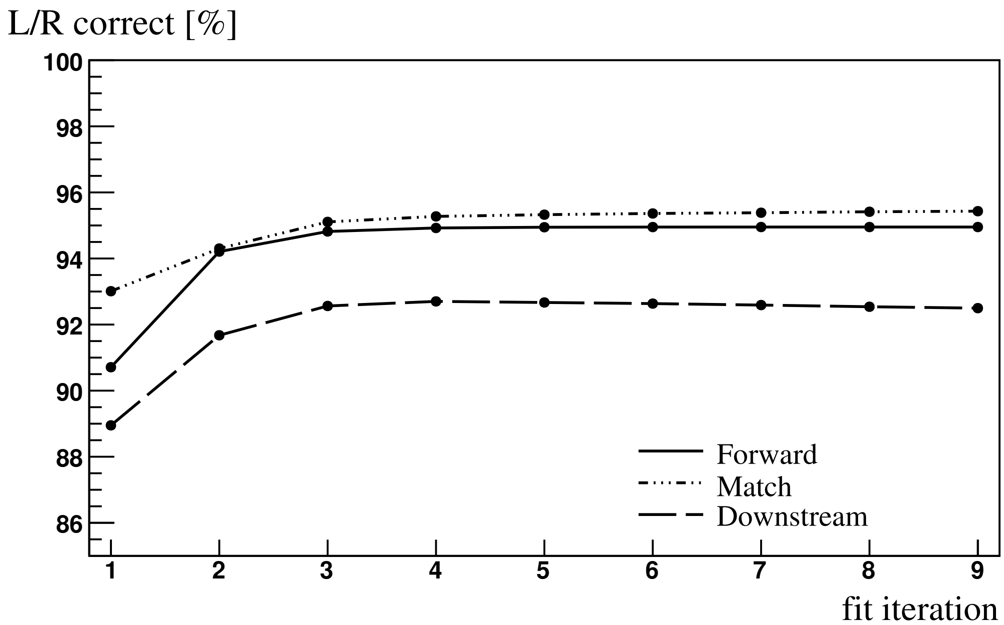

Figure 6.5: *The average percentage of correctly assigned OT L/R signs, as a function of the fit iteration, performed in addition to a single prefit iteration, which determined those signs, split by pattern recognition strategy.*

After including the prefit in the fitting procedure, the number of fit iterations that are required for a converged fit is determined by inspecting the change in χ^2/n_{DOF}, as in subsection 6.8.1. The fraction of converged track fits is shown in figure 6.6 as a function of the number of fit iterations, which are performed after the prefit iteration.

These fractions start out higher than those found without using the prefit iteration, see figure 6.2. For Long tracks, the fractions also approach their asymptote faster, as opposed to the Downstream tracks, but the values of the asymptotes are the same as in figure 6.2.

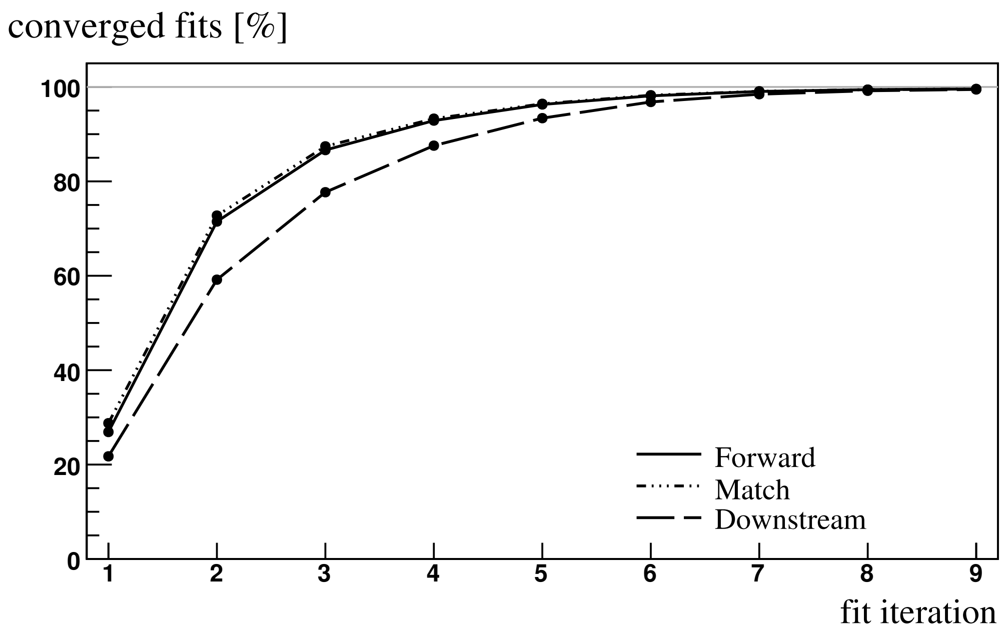

Figure 6.6: *The percentage of converged track fits as a function of the number of regular fit iterations, performed after one prefit iteration, split by pattern recognition strategy.*

The total number of needed fit iterations are listed in table 6.5, as well as the corresponding fractions of stable fits. Comparing to the numbers for the fixed number method in table 6.3, the same number of fit iterations are required. However, these are in addition to the prefit iteration, making the total increase by one iteration. The corresponding fractions of stable fits are 0.2–0.4% higher for Long tracks, whereas the fraction for Downstream tracks is 0.3% lower. Changes are not observed in the fractions found when using the monitoring method. In addition, consistent with the observed behaviour in figure 6.6, the monitoring method requires 0.2–0.3 fewer fit iterations, as shown in the second column of table 6.5, though the total number of iterations is higher due to the added prefit iteration.

Overall, the monitoring method is superior to the fixed number method concerning both the number of iterations and the stable fractions, even more so when including a prefit iteration in the fit procedure. For now, the tuned LHCb track fit uses the fixed number method with the number of iterations of table 6.3 for Velo, Upstream and T tracks, and the number of prefit and fit iterations of table 6.5 for Long and Downstream tracks.

Table 6.5: *The combined number of prefit and fit iterations, and percentage of converged fits for the fixed number and monitoring methods, split by the pattern recognition strategies which found the tracks. The uncertainty on these numbers is smaller than the last presented digit.*

	fixed number		monitoring	
PR strategy	# prefit and fit iterations	converged fits [%]	# prefit and fit iterations	converged fits [%]
Forward	1+5	96.3	1+3.3	99.6
Match	1+5	96.4	1+3.2	99.6
Downstream	1+6	96.8	1+3.6	99.5

6.8.3 Outlier removal

A fitted track can contain hits that are not compatible with the track model. Such hits increase the errors on the track parameters of nearby states, reducing the track quality in that region. Therefore the track fit improves by removing the non-compatible or outlier hits from the tracks. Outliers are defined as those hits which lie at least 3σ outside of the track [58], which corresponds to hits representing a χ^2 contribution larger than nine.

At the end of the prefit and regular fit iterations, outlier removal iterations are performed. During an outlier removal iteration, from all hits with a χ^2 contribution exceeding nine, the one with the highest χ^2 contribution is deleted from the list of hits. Subsequently, a fit iteration is performed to update the state vectors and covariance matrices of all states on the track. The other hits that previously qualified as an outlier may have their χ^2 contribution reduced to below nine by this outlier removal iteration.

Figure 6.7 shows the fraction of all tracks as a function of the number of outliers that they contain, split by pattern recognition strategy. The trend for the track fractions is to decrease rapidly with the number of outliers, indicating compatibility between the hits and the track model. Velo tracks on average contain the least amount of outliers, which is ascribed them having a lower field integral and shorter extrapolation distance than other types of tracks, making them the least sensitive to the inherent errors of the approximations made in the multiple scattering and energy loss models of the track fit. Downstream tracks have the most outliers, which is not due to the purity of the hits as shown in table 5.8.

Figure 6.8 shows the fraction of all hits that are formed by outliers, as a function of the number of outliers that are present on the tracks. These fractions increase with the number of outliers and all of them reach values exceeding 25% over the inspected range. A balance is sought between improving the track quality by removing outliers and preventing an unjustifiably large fraction of a track's hits to be removed. Removing a maximum of 15% of a track's hits is chosen to be allowed and is implemented in the track fit as a fixed number of outlier removal iterations.

The fixed numbers are listed per pattern recognition strategy in the first column

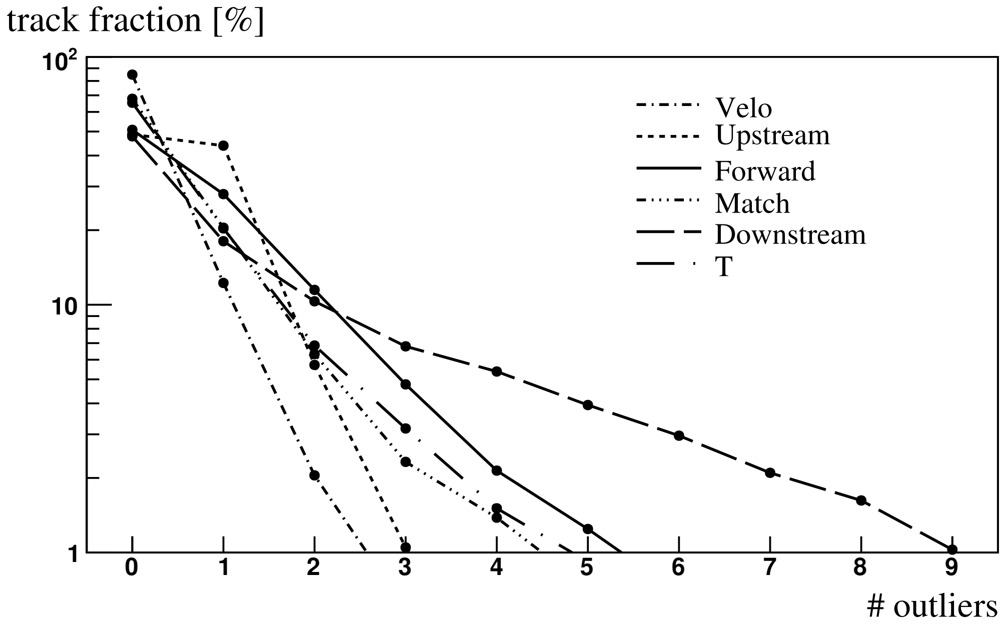

Figure 6.7: *The percentage of tracks, shown per pattern recognition strategy, as a function of the number of outlier hits that they contain.*

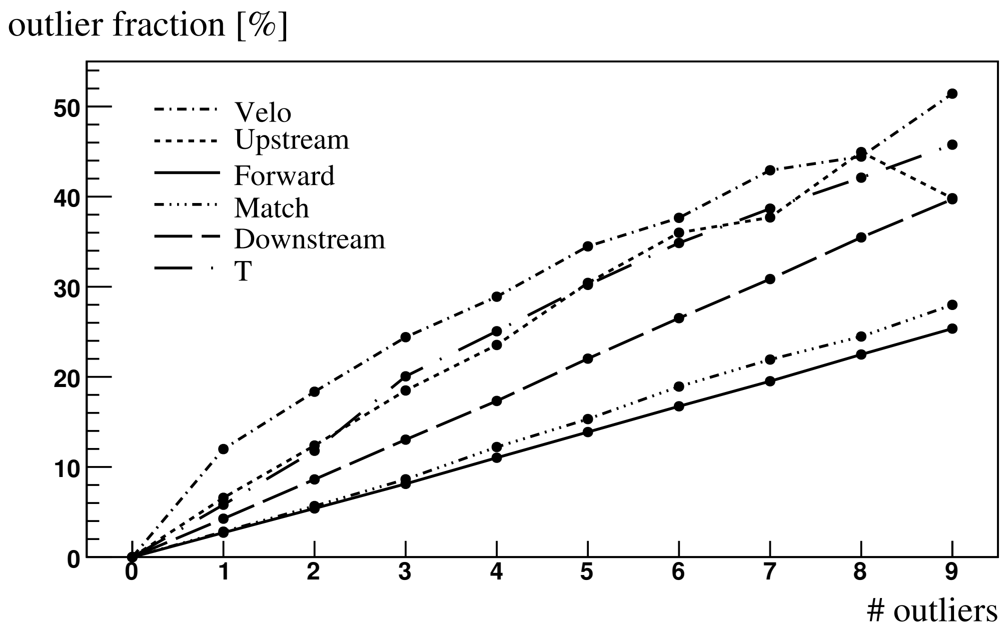

Figure 6.8: *The percentage of all hits of a track that are outliers, shown per PR strategy, as a function of the total number of outliers that a track contains.*

of table 6.6. Forward Long tracks allow for five outliers to be removed, but since the Forward and Match strategies find the same track type and their tracks are compared during the clone-killing stage, see section 7.1, both are allowed to remove only four as dictated by the Match Long tracks. These outlier removal iterations remove almost all outliers from the Velo, Upstream and Long tracks, as shown in the second column of table 6.6. T and especially Downstream tracks retain a number of outliers, which leaves room for improvement.

Table 6.6: *The number of outlier removal iterations and the fraction of tracks for which these iterations remove all of their outliers, split by pattern recognition strategy. The uncertainty on these numbers is smaller than the last presented digit.*

PR strategy	# iterations	track fraction [%]
Velo	1	97.1
Upstream	2	98.2
Forward	4	97.1
Match	4	98.3
Downstream	3	83.0
T	2	92.5

6.8.4 Ionisation energy calibration

At this point, a fitted track is stable with respect to its $\chi^2/\mathrm{n_{DOF}}$ value, its fraction of correct L/R signs, and its hit content. This allows for a calibration of the energy-loss model, which is an approximation to what Geant4 simulates, as described in section 4.5 and subsection 6.3.7. The spectrometer measures the momentum of a track around the magnet region. The momentum value at the vertex is used to determine the masses of the resonances in physics analyses of the events. This momentum is determined by extrapolating the nearest state of a track to the z-coordinate of the vertex. During this extrapolation step, the track encounters material, for example the beam-pipe. The fit as a whole extrapolates to more locations than the one mentioned in this example, encountering various material layers. Traversed material is treated as a thick scatterer in which ionisation occurs. The loss of energy due to ionisation is compensated for during the upstream extrapolation to the vertex. Therefore the extrapolation results in an increase of the momentum of a track from the most upstream state to the vertex.

If the energy-loss is incorrectly compensated for, this shows as a bias in the momentum's pull distribution. The momentum pull is the difference between the track's momentum and the Monte-Carlo momentum, divided by the error on the track's momentum, as obtained from the state covariance matrix. In order to achieve a zero mean, the c_{ion} parameter of equation (6.23) is tuned. In figure 6.9, the mean value of the momentum's pull distribution is shown as a function of the value of the ionisation energy constant. This plot is composed of all tracks that originate from the VELO. As expected from equation 6.24, there is a linear relationship between the mean and c_{ion}. A straight-line fit passes the zero-mean axis at a value for c_{ion} of 364.9 ± 0.5 MeV mm^2 mole^{-1}. The tuned value of c_{ion} is used in the fit when determining the performance as detailed in chapter 7.

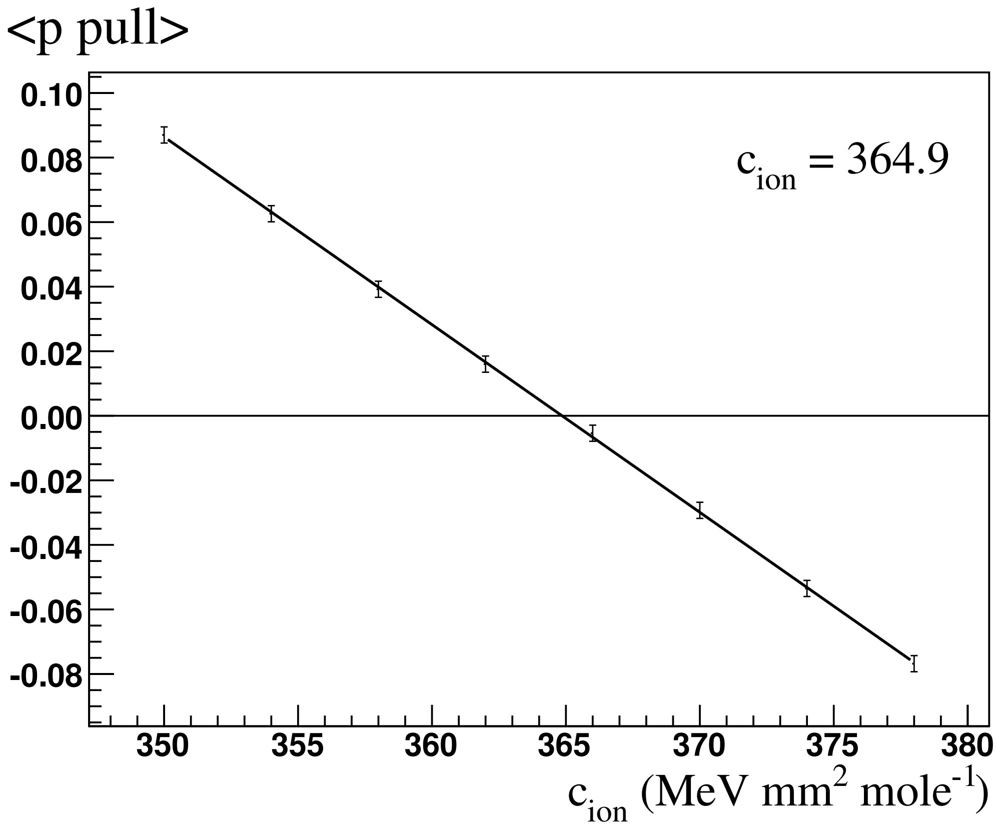

Figure 6.9: *The mean of the track momentum's pull distribution as a function of the ionisation energy parameter* c_{ion}.

Chapter 7

Performance

The performance of the track reconstruction is evaluated in three parts. First, the clone rates, the number of tracks, and the track χ^2 probability distributions are discussed in subsection 7.1. Second, the number of hits, the hit residual pull widths, and the hit efficiencies and purities are assessed in subsection 7.2. Third, the track parameter pulls and resolutions at three locations in the detector as well as per track sub-detector are listed. Additionally, the transverse momentum, momentum and pseudorapidity dependence of the resolutions and pulls at the vertex are inspected in subsection 7.3. A comparison between Long tracks and equivalent tracks that have been identified using the Monte-Carlo information as described in subsection 5.3.7, named Ideal Long tracks, is made in the course of this chapter.

7.1 Clone removal and track properties

Two properties of the reconstructed tracks are inspected in this section. Clones are excluded from inspection to which end they are identified and removed from the collection of tracks. Subsequently, the number of remaining tracks per event is determined per track type. These form the collection of tracks which is made available by the track reconstruction for use in physics analyses. The quality of the fitted tracks is represented per track type by a χ^2 probability distribution and its mean. These are determined and shown at the end of this section.

- **Clone tracks**

  Tracks are reconstructed from the hits which have been assigned to them, as described in sections 5.2 and 5.3. As introduced in subsection 5.4.2, it is possible for two tracks to both contain hits corresponding to a single MC particle. This occurs more often when the pattern recognition algorithms are run in concurrent mode, compared to filtered mode, as the former allows each strategy to use all of the hits. For the studies presented in this thesis, pattern recognition is performed in filtered mode, as described in section 5.3.

  A fitted track that shares at least 70% of its hits in the VELO and T-stations with another track is considered to be a clone. Hits in the TT are not considered. This definition differs from the one in subsection 5.4.2 in that the comparison is no longer performed through the associated MC particle, but rather directly between the hits of the tracks. One track of each pair of clones is removed at the end of the track reconstruction process. In case they contain a different number of hits, the one with fewer hits will be removed. Otherwise the one with the higher χ^2/n_{DOF} is considered to be the clone. A study of clones and clone-fractions can be found in [127].

The clones that are removed by the clone killing procedure amount to the percentages that are listed in table 7.1. As clone killing takes ghost tracks into account, and does not use the Monte-Carlo information, the numbers are different from those listed in table 5.3. The clone killing choses which track of a clone pair is labeled to be the clone, thereby eliminating the double counting which is present in table 5.3. This is most clear in the lower percentages of Forward and Match clones. Those percentages also show that mostly the Match track of a Forward-Match clone pair is chosen to be the clone, which is consistent with their lower average number of hits, see table 5.6.

Table 7.1: *The event-averaged and track-averaged percentages of clone tracks, split by pattern recognition strategy. The uncertainty on these numbers is smaller than the last presented digit.*

strategy	EA clones [%]	TA clones [%]
Velo PR	0.0	0.0
Upstream PR	2.0	1.8
Forward PR	26.5	25.6
Match PR	60.1	59.1
Downstream PR	20.2	16.9
T PR	1.8	1.4

- **Number of tracks**

  The track reconstruction results in a final track sample with on average 85.2 ± 0.05 tracks per event. This number is split by track type and listed in the table of figure 7.1. Due to the removal of clone tracks, the average is decreased by 19.5 ± 0.05 tracks compared to the 104.8 ± 0.05 tracks that are found by the pattern recognition strategies in section 5.4. This difference is mainly formed by Long tracks from the overlap of the Forward and Match Long track collections, which have been removed by the clone killing procedure. Without this overlap, the Long tracks from the Forward and Match strategies can be integrally referred to as the Long tracks. The average number of Ideal Long tracks in an event are added to the table, see subsection 5.3.7 for their definition. There are fewer Ideal Long tracks found than Long tracks, as the latter collection in addition contains ghost tracks.

  The distribution of the number of tracks in an event is shown for each track type in the plot of figure 7.1. It shows the Long and Ideal Long track distribu-

track type	# tracks
Velo	31.3
Upstream	7.2
Long	25.4
Downstream	7.8
T	13.5
Ideal Long	23.0

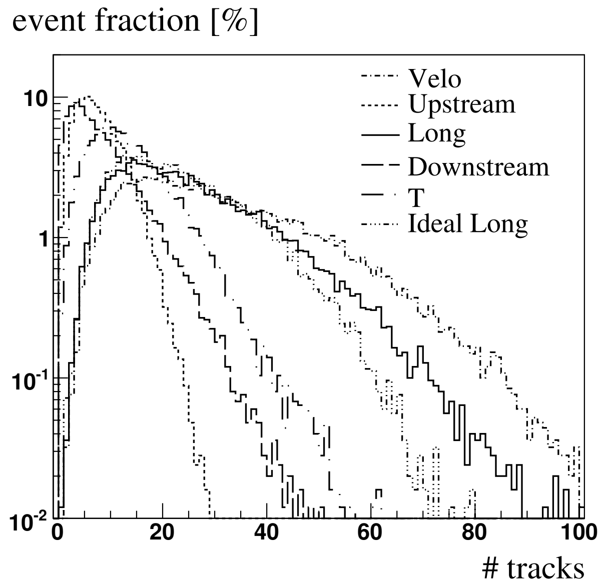

Figure 7.1: *Average number of tracks per event (**left**) and distribution of the number of tracks per event (**right**), split by track type. The uncertainty on these numbers is smaller than the last presented digit.*

tions to be similar, with the difference in their tails made visible by the choice of a logarithmic scale for the vertical axis.

- **χ^2 probability**

  For each type of fitted track, the χ^2 probability is determined and shown in the table and plot of figure 7.2. The theoretical optimum of the mean of a χ^2 probability distribution is 0.5. The means for all but the Upstream track collection are below this optimum. These lower values are ascribed to tracks with a large χ^2/n_{DOF}, occupying the peaks at the lower end of the probability range. The χ^2 probability distribution is supposed to be uniform if the paths of the particles are properly described by the track model. Tracks from poor fits result in the peaks near zero. An increasing number of tracks per bin towards the upper end of the probability range, as seen for Upstream tracks, is due to a reduction in the χ^2/n_{DOF} by removing outliers. The remainder is approximately uniform, indicating that the majority of the tracks are properly reconstructed. Long and Ideal Long tracks result in near identical distributions. This indicates that the hit content and L/R sign assignment leave little room for improvement.

7.2 Hit properties

The average hit content of tracks is changed during the outlier removal iterations and by the clone killing procedure, which removes the track with fewer hits from

track type	$<\chi^2$ prob.$>$
Velo	0.41
Upstream	0.53
Long	0.43
Downstream	0.40
T	0.33
Ideal Long	0.42

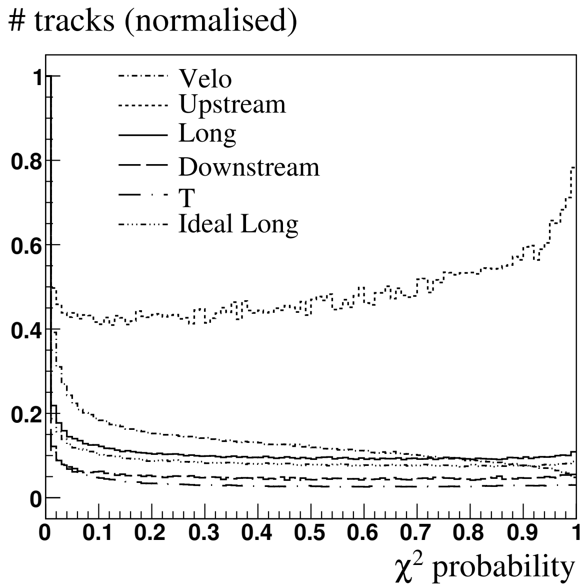

Figure 7.2: *Mean χ^2 probability of tracks (**left**) and χ^2 probability distributions of tracks (**right**), split by track type. The uncertainty on these numbers is smaller than the last presented digit.*

a pair of clones. In table 5.6, the number of hits is shown at the end of the pattern recognition phase. Table 7.2 lists the numbers found for fitted tracks, which are all lower than their corresponding values before fitting. This difference is predominantly due to outlier removal. Ideal Long tracks have been added to the table, overall showing higher numbers than found for Long tracks, as they are assigned the complete set of hits belonging to a particle.

Table 7.2: *The track-averaged number of the different types of hits and their total are listed per track type. The uncertainty on these numbers is smaller than the last presented digit.*

track type	total	Velo R	Velo ϕ	TT	IT	OT
Velo	8.3	4.3	4.0	···	···	···
Upstream	14.8	5.6	5.4	3.8	···	···
Long	36.0	6.6	6.3	3.4	2.5	17.3
Downstream	22.8	···	···	3.4	1.1	18.3
T	23.4	···	···	···	4.9	10.2
Ideal Long	37.4	6.6	6.4	3.6	2.3	18.4

Distributions of the number of hits per track are shown for all track types in the plots of figure 7.3. A preference for an even number of hits is apparent for Velo tracks. This is due to the pairing of R and ϕ sensors in the VELO, which predominantly both register a hit when a particle traverses their module. The odd number of hits are mainly formed by tracks which have the allowed maximum of

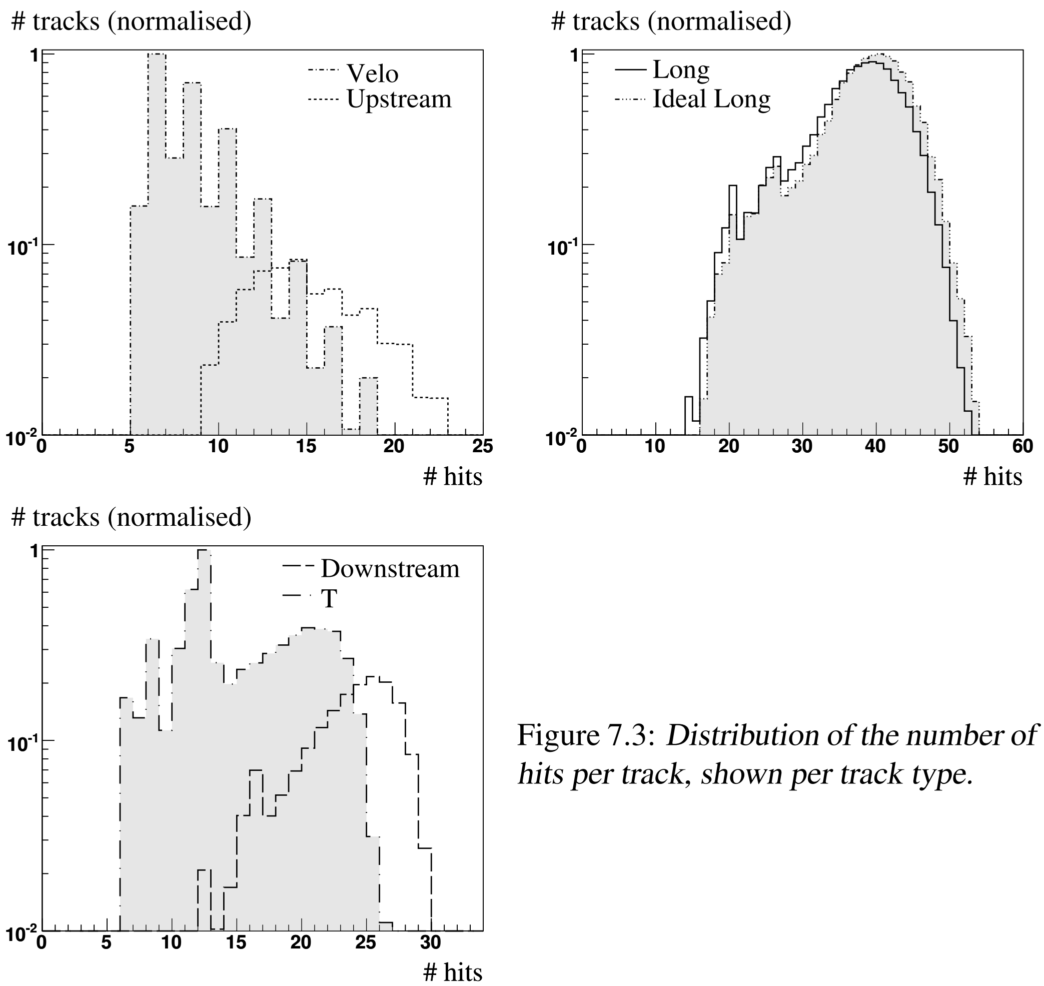

Figure 7.3: *Distribution of the number of hits per track, shown per track type.*

one outlier removed. The distributions for Long and Ideal Long tracks reach their maxima around 40 hits, which corresponds to tracks passing through the OT. In addition there are peaks at 20 and 26 hits, corresponding to tracks that pass through the IT and through both IT and OT, respectively. The same structure is observed in the distributions for Downstream and T tracks.

Each hit is a one-dimensional measurement of the path of a particle and has an associated error, which is provided by the clustering algorithm of its tracking subdetector. This error signifies the expected difference between the hit and the true position of the particle, based on our knowledge of the detector's performance. Using the Monte-Carlo information, the true value of this distance can be determined as the true residual of the projected true state. Dividing this true residual by the hit error for a number of hits of the same type, results in a true residual pull distribution. This distribution is expected to be Gaussian and of unit width, in case the hit errors are correctly estimated.

The true residual pull distributions for Long tracks are shown in figure 7.4. Except for the distribution for OT hits, they are not Gaussian. Their deviation from the Gaussian shape are in the form of tails and clustering artifacts[1]. The latter is noticeable in the distribution for VELO ϕ hits, which features a double peak structure. This is due to charge threshold settings, which leads to the rejection of strips from a hit, which collected sufficient charge to bias the centre of charge upon exclusion. Incorrect hit errors affect the filtering of predicted states, resulting in incorrect filtered state vectors and filtered state covariance matrices. Here, incorrect refers to the fact that a filtered state is determined either too much or too little by the predicted state, depending on whether the hit error is overestimated or underestimated. As a track contains several hits, the effect of non-Gaussian hit errors is diluted. Its mean influence on a track depends on the RMS of the true residual pull distribution.

The width of a true residual pull distribution is determined as the RMS over a range from minus three to three. In table 7.3 the widths are listed for Long tracks, separated by hit type. These widths are smaller than one, which means that the hit errors are overestimated.

Table 7.3: *The RMS values of the true residual pull distributions, determined per hit type. The uncertainty on these numbers is smaller than the last presented digit.*

track type	Velo R	Velo ϕ	TT	IT	OT
Long	0.93	0.95	0.97	0.84	0.95

A residual pull can also be determined by using the averaged state of a fitted track, rather than the true state. Such a residual pull is a measure for the compatibility between the hit error and the residual of the averaged state and the hit, requiring as prerequisite a correctly estimated hit error. As the residual pulls can be determined from real data, they are inspected here using the ideal, aligned, and misaligned geometries of subsection 5.4.5.

Figure 7.5 shows the residual pull distributions of fitted Long tracks for each of the five hit types, and for each of the three geometries. Their Gaussian widths are stated in table 7.4 and in case of the ideal geometry, all but those of the TT are near the optimum of one. As desired, the results of the aligned geometry are close to those of the ideal geometry. In case of a misaligned detector, the Gaussian widths increase significantly. This can be used to signal misalignments in the detector, in which case the alignment procedure should be used to align the detector.

The hit finding efficiencies are reduced from their values before the fit by the outlier removal iterations. The efficiencies for fitted tracks are listed in table 7.5 and can be compared to the values before fitting as shown in table 5.7. As the tracks from the Forward and Match strategies have been merged, their efficiencies are not one-to-one comparable to the efficiencies of the fitted Long tracks.

In case most of the removed outliers are incorrect hits, the hit purity increases from the values of table 5.8. This is the case for Velo, Long and T tracks, as seen

[1]Post DC06, the hit error estimation of VELO, TT and IT has been improved by implementing more realistic error models and tuning those models, resulting is proper true residual pull distributions.

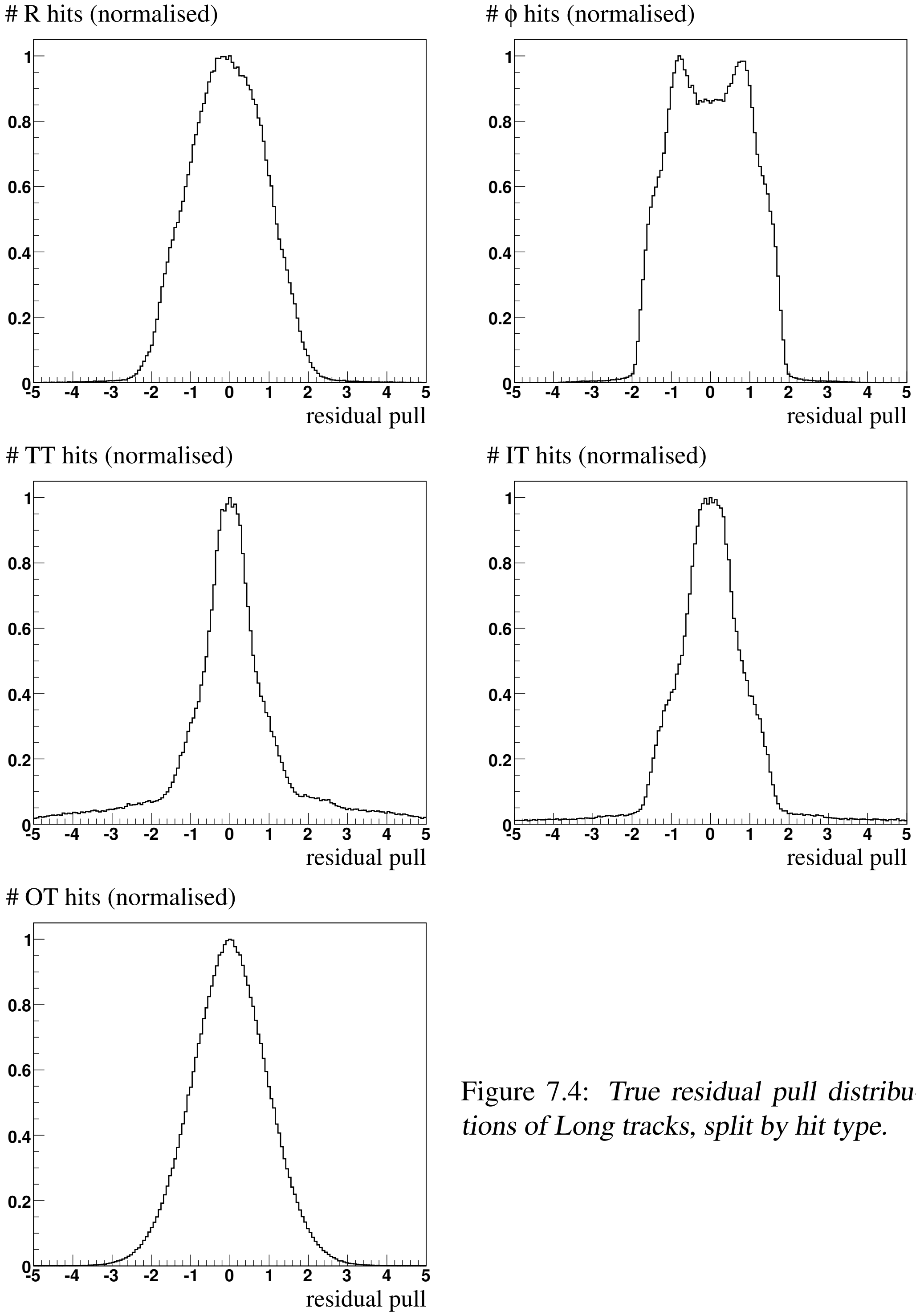

Figure 7.4: *True residual pull distributions of Long tracks, split by hit type.*

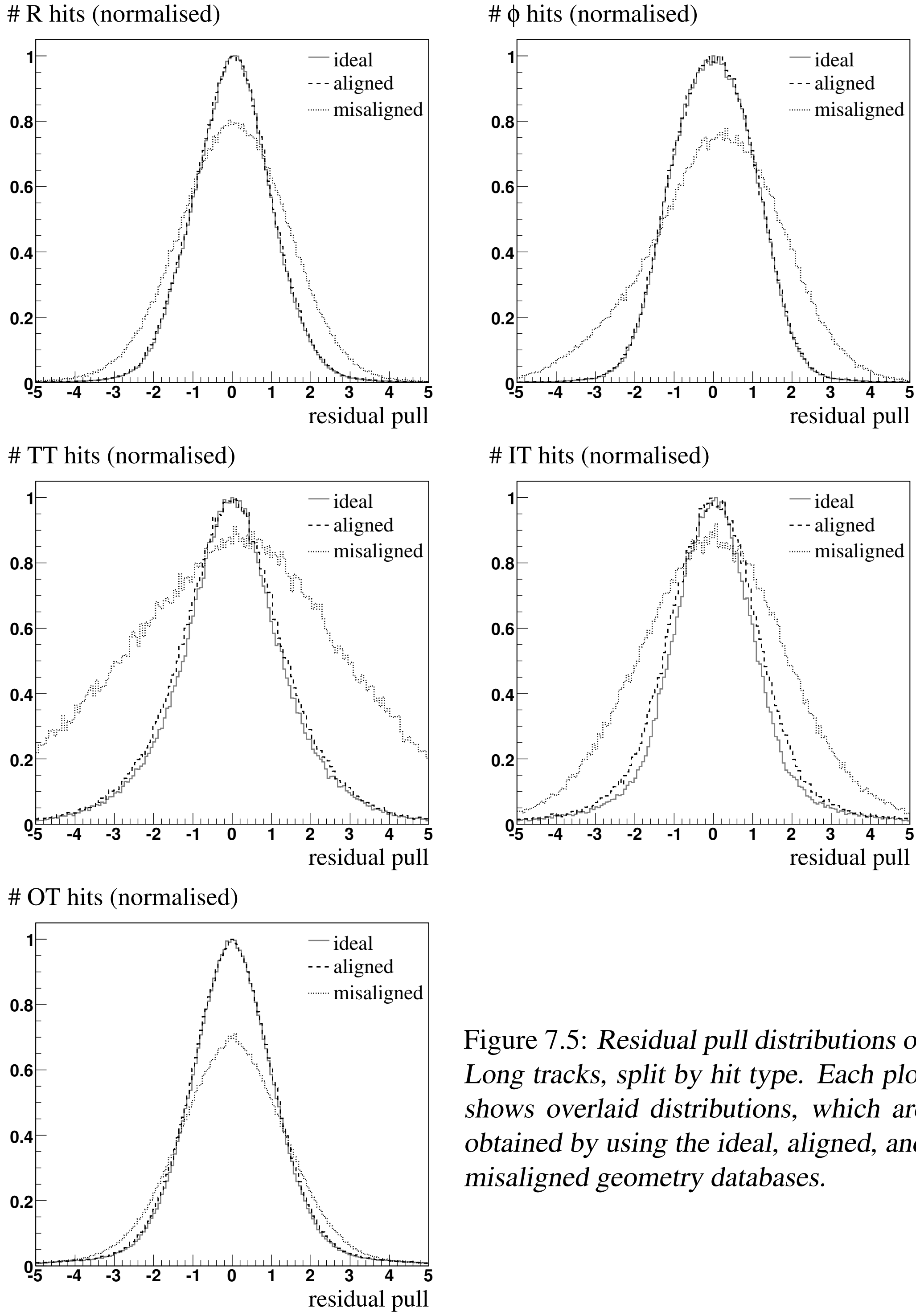

Figure 7.5: *Residual pull distributions of Long tracks, split by hit type. Each plot shows overlaid distributions, which are obtained by using the ideal, aligned, and misaligned geometry databases.*

Table 7.4: *The width of fits with a Gaussian function to the residual pull distributions of Long tracks, determined for the ideal, aligned, and misaligned geometries, and split by hit type. The uncertainty on these numbers is smaller than the last presented digit.*

geometry	Velo R	Velo ϕ	TT	IT	OT
ideal	0.99	1.03	1.37	1.09	1.09
aligned	1.01	1.04	1.43	1.23	1.12
misaligned	1.37	1.67	2.95	1.89	1.40

Table 7.5: *Track-averaged hit efficiency for each track type, shown for all hits together and for each hit type separately. The uncertainty on these numbers is smaller than the last presented digit.*

track type	total ϵ [%]	VELO ϵ [%]	TT ϵ [%]	IT ϵ [%]	OT ϵ [%]
Velo	84.5	84.5	$\cdots$	$\cdots$	$\cdots$
Upstream	91.1	87.8	94.5	$\cdots$	$\cdots$
Long	91.9	95.3	86.7	93.7	93.1
Downstream	84.7	$\cdots$	87.9	76.4	82.9
T	76.0	$\cdots$	$\cdots$	81.3	71.4

from table 7.6. However, the Upstream and Downstream hit purities are slightly lower than before the fit.

7.3 Resolutions and pulls

An averaged state vector of a fitted track contains the optimal estimates of the track parameters. The difference between each estimate and the true value, as obtained from the Monte-Carlo information, is referred to as the residual δx. The distribution of the residual of a track parameter is inspected in the determination of the

Table 7.6: *Track-averaged hit purity for each track type, shown for all hits together and for each hit type separately. The uncertainty on these numbers is smaller than the last presented digit.*

track type	total ρ [%]	VELO ρ [%]	TT ρ [%]	IT ρ [%]	OT ρ [%]
Velo	99.0	99.0	$\cdots$	$\cdots$	$\cdots$
Upstream	98.9	99.4	98.4	$\cdots$	$\cdots$
Long	99.3	99.5	99.1	99.8	99.0
Downstream	96.7	$\cdots$	94.4	99.8	98.6
T	97.6	$\cdots$	$\cdots$	99.2	96.3

track fit performance. In figure 7.6, the residual distributions at the primary vertex are shown. They are shaped as a central Gaussian, combined with considerable tails. A functional description of the observed distributions is found in the sum of two Gaussian functions. The surface-weighted mean of the widths of the two Gaussian functions is chosen to represent the width of the residual distributions. This width is called the resolution of the track parameter, and is used as a measure of the performance of the track fit.

The track parameter resolutions are determined at the vertex and at the first hit. Their values are listed in table 7.7, where they are split by track type. All of the coordinate resolutions are worse at the vertex than at the first hit. During the extrapolation of the state at the first hit to the vertex, the slope residuals translate into deteriorating coordinate resolutions. As Velo tracks have the worst slope resolutions at the first hit, they have the worst coordinate resolutions at the vertex. The slope resolutions deteriorate during extrapolation because of multiple scattering in the VELO foil and the beam pipe. Long tracks have a momentum resolution of $0.37 \pm 0.005\%$ at both the first hit and the vertex, showing that the energy loss correction of subsection 6.3.7 does not deteriorate the momentum resolution. Upstream tracks have a poor momentum resolution, as hits on both sides of the magnet are required for proper momentum estimation. Velo tracks have no momentum resolution determined, as their momentum is assigned pro forma, as described in subsection 5.3.1. Ideal Long tracks have marginally better track parameter resolutions than Long tracks, which is ascribed to their higher hit purity. Overall, the resolutions are good and sufficient for the purposes of physics analyses, as discussed in the last chapter.

Table 7.7: *The track parameter resolutions at the vertex and at the first hit, listed for the relevant track types. The uncertainty on these numbers is smaller than the last presented digit.*

location	track type	x [μm]	y [μm]	t_x [10^{-4}]	t_y [10^{-4}]	p [%]
Vertex	Velo	58.8	57.6	10.3	10.1	···
	Upstream	55.3	55.9	8.13	8.18	17.3
	Long	39.1	39.0	3.52	3.53	0.37
	Ideal Long	37.9	37.6	3.61	3.61	0.35
First hit	Velo	13.1	13.0	6.57	6.45	···
	Upstream	9.2	9.7	5.74	5.77	17.3
	Long	7.9	7.7	2.48	2.45	0.37
	Ideal Long	8.0	7.7	2.56	2.52	0.35

For the Long and Ideal Long tracks, the track parameter resolutions have also been determined as averages over the states of each of the four tracking sub-detectors. The resulting resolutions are stated in table 7.8. In the VELO, the coordinate resolutions are about the same as at the first hit. The slopes however are better, as the average VELO hit has two neighbours to constrain the state at its position, whereas

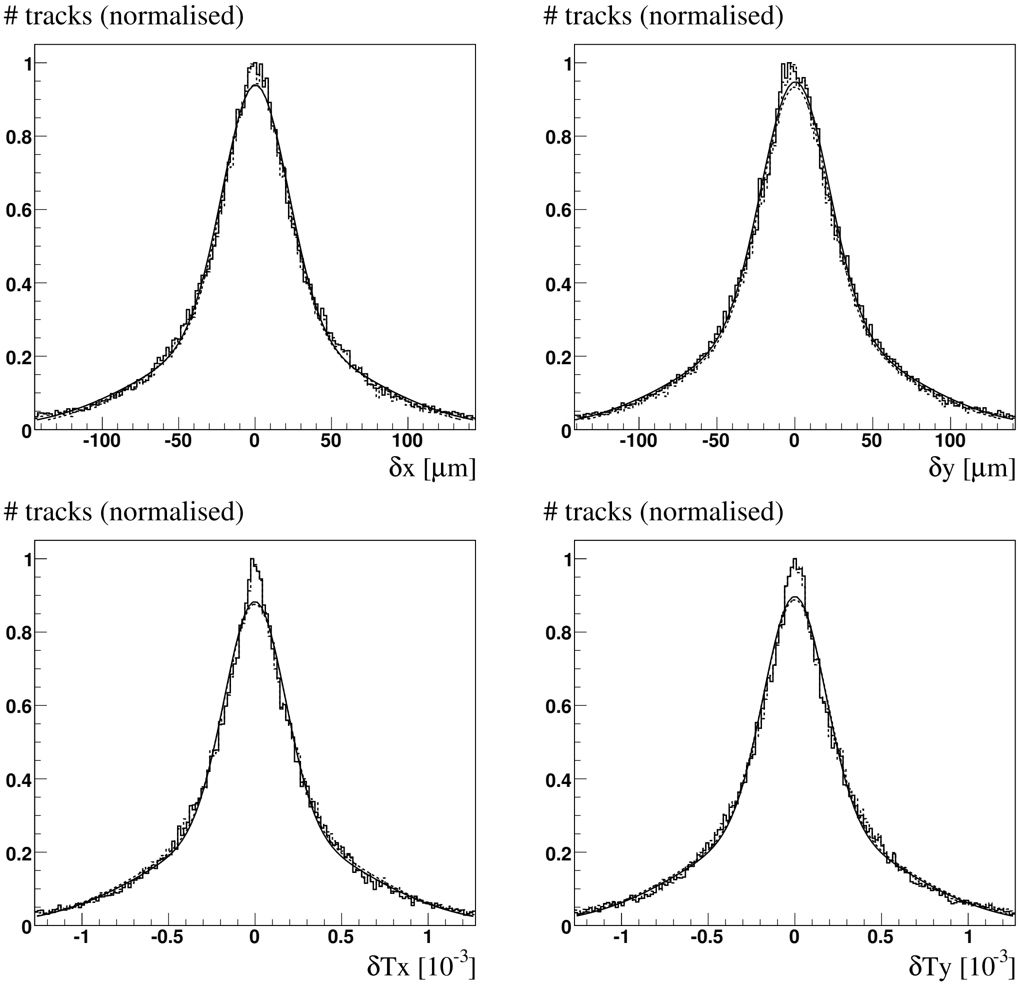

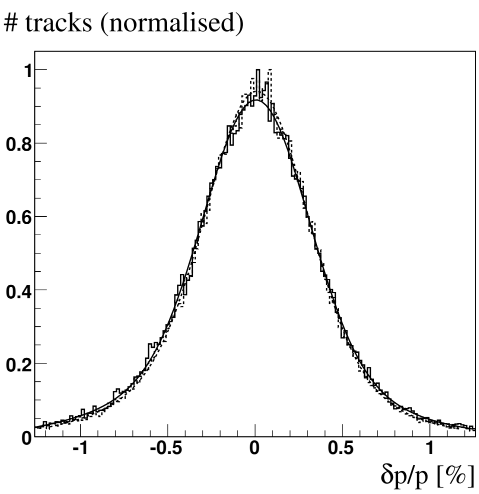

Figure 7.6: *Fitted residual distributions of the track parameters of Long (solid) and Ideal Long (dashed) tracks at the vertex. The pairs of distributions and pairs of fits show considerable overlap.*

the first hit only has one neighbour. Though the TT and IT use the same silicon sensors, the coordinate and slope resolutions at the latter are better than at the former. This is due to the smaller number of TT hits than T-station hits on a Long track. At the TT, the mean 3.4 hits must compensate for the inherent inaccuracies of the long extrapolation through the magnetic field of the T-station part of the track, and of the extrapolation from the VELO. It does this well enough to enable the fit to achieve a good momentum resolution, as is the function of the TT [43]. As the VELO uses an $R\phi$ geometry, it does not feature the resolution difference between x and y which is apparent for the other tracking sub-detectors, which have an x-u-v-x configuration. Those use a $\pm 5°$ stereo angle between their detection layers, allowing for a determination of the y coordinate and slope albeit at a lower accuracy than obtained for the x coordinate and slope. The expected difference in x and y-coordinate resolutions is a factor of $1/\sin(5°) = 11.5$, which is close to the difference in table 7.8. The OT drift-tubes have a larger resolution than the silicon sensors of the IT, resulting in larger coordinate and slope resolutions. Comparing the results for Long tracks with those for Ideal Long tracks shows a negligible difference, proving that the hit content of Long tracks is sufficient to obtain the full fit performance in terms of resolutions.

Table 7.8: *Average track parameter resolutions for the states of different sub-detectors for Long and Ideal Long tracks. The uncertainty on these numbers is smaller than the last presented digit.*

sub-detector	x [μm]	y [μm]	t_x [10^{-4}]	t_y [10^{-4}]	p [%]
VELO	8.01	8.00	1.31	1.32	0.39
TT	26.4	298.	1.70	2.23	0.35
IT	13.8	180.	0.75	1.59	0.39
OT	80.0	856.	2.57	5.42	0.36
Ideal VELO	8.05	8.00	1.36	1.36	0.37
Ideal TT	26.8	304.	1.77	2.30	0.34
Ideal IT	13.8	178.	0.75	1.57	0.37
Ideal OT	76.9	814.	2.67	5.70	0.34

The dependence of the coordinate and slope resolutions at the vertex on one over the transverse momentum allow verification of the propagation methods, and is shown in figure 7.7. These quantities increase as a function of one over the transverse momentum, which is modelled in [128]. The final two plots show the dependency of the momentum resolution on the momentum and on the pseudorapidity. A minimum in the momentum resolution distribution as a function of momentum is located around 3 GeV. The effects of multiple scattering result in an increased momentum resolution below 3 GeV. The curvature of particles in the magnetic field decreases with increasing momentum. Combined with the constant coordinate resolution of the tracking sub-detectors, this leads to an increasing momentum resolution above 3 GeV. The momentum resolution increases with pseudorapidity, as the coordinate resolutions increase. Towards the edges of the acceptance, a track traverses fewer sensors, resulting in fewer constraints on the track parameters and increased resolution.

A comparison can be made between the residual δx and the value which the track fit estimates the residual has, as quantified by the smoothed track parameter covariance matrix element σ_x. This is done by dividing the two quantities and plotting the resulting distribution, which is referred to as the pull distribution. Through the central limit theorem, this is expected to be a Gaussian distribution. In case the estimated track parameter error is a sampling from the same probability distribution as the actual error is, the pull is Gaussian and has unit width.

In figure 7.8 the pull distributions of the five track parameters at the vertex are shown for Long and Ideal Long tracks. These distributions are fitted with a Gaussian function using a range from minus three to three. Each distribution features non-Gaussian tails, predominantly outside of the fitted range. These are ascribed to non-linear components of multiple scattering and the approximation made by linearising the projection functions.

The widths of the pull distributions are determined at the vertex and at the first hit. In table 7.9, the widths of the track parameter pulls are listed. The coordinate pulls at the first hit are good, being close to the optimal value of one. The slope pulls however are too wide. Improving the slope resolutions should therefore remedy this. As seen for the coordinate resolutions at the vertex, the increased slope resolutions similarly result in underestimated coordinate errors, resulting in too wide coordinate pulls at the vertex. The Ideal Long tracks have a few percent better pulls than the Long tracks, which is ascribed to their higher hit purity. The momentum pull of all tracks is about 25% too wide. Both Long and Ideal Long tracks display this behaviour, eliminating the hit content as a cause. Post DC06 the settings for the treatment of charged particle interactions with material by Geant4 have been identified as the main cause for the deviation from one of the momentum pull width. This is a preliminary conclusion and requires further study.

Table 7.9: *Gaussian widths of the track parameter pull distributions at the vertex and the first hit, listed per track type. The uncertainty on these numbers is smaller than the last presented digit.*

location	track type	x	y	t_x	t_y	p
Vertex	Velo	1.18	1.17	1.19	1.17	···
	Upstream	1.12	1.13	1.12	1.12	1.24
	Long	1.08	1.09	1.10	1.11	1.26
	Ideal Long	1.07	1.08	1.09	1.10	1.24
First hit	Velo	0.99	1.00	1.17	1.16	···
	Upstream	0.95	0.98	1.18	1.18	1.23
	Long	0.96	0.99	1.12	1.13	1.25
	Ideal Long	0.95	0.98	1.12	1.12	1.24

The widths of the pull distributions, averaged over all hits of a tracking sub-

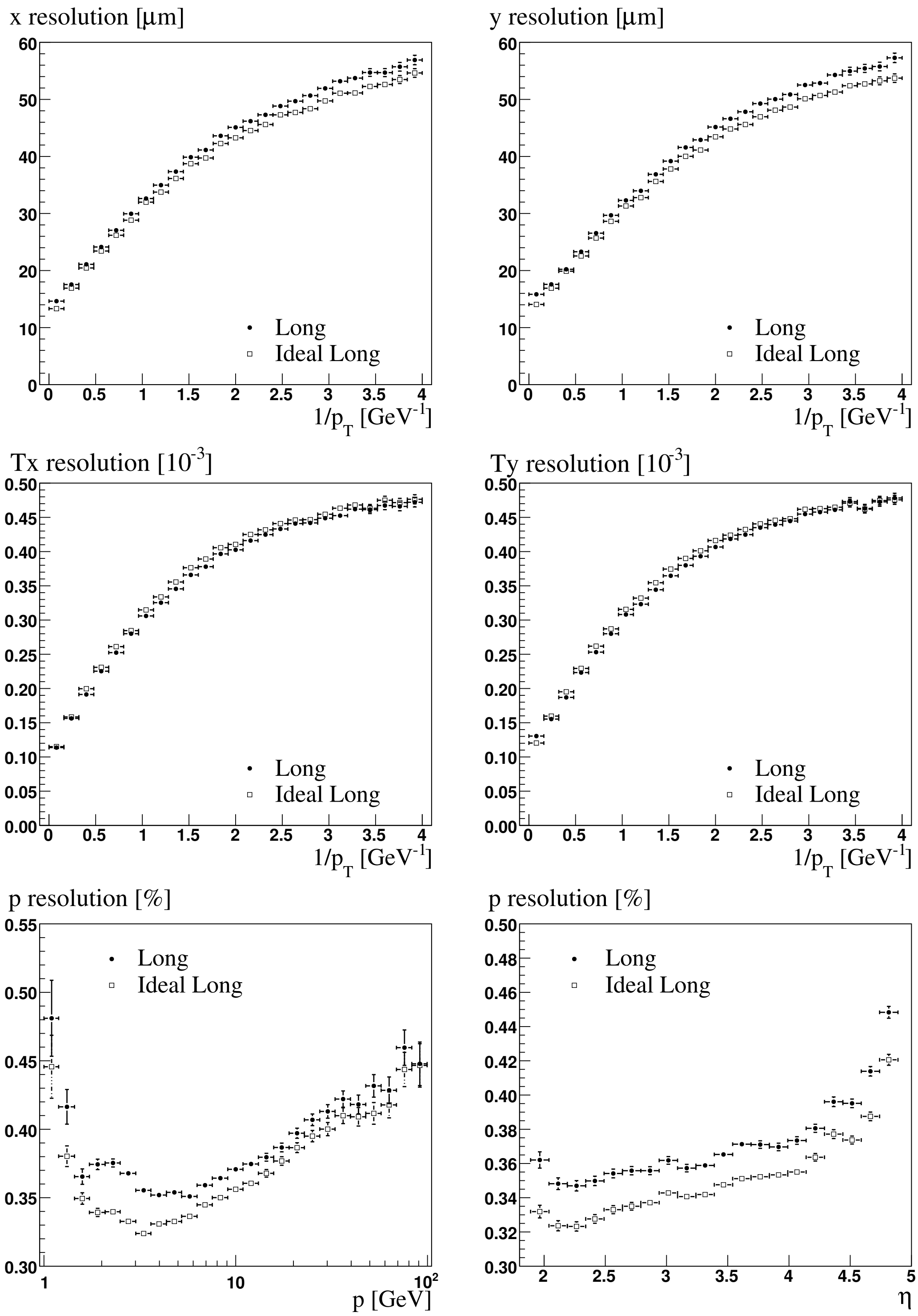

Figure 7.7: *Long and Ideal Long track parameter resolutions at the vertex, as a function of one over the transverse momentum, the momentum and the pseudorapidity.*

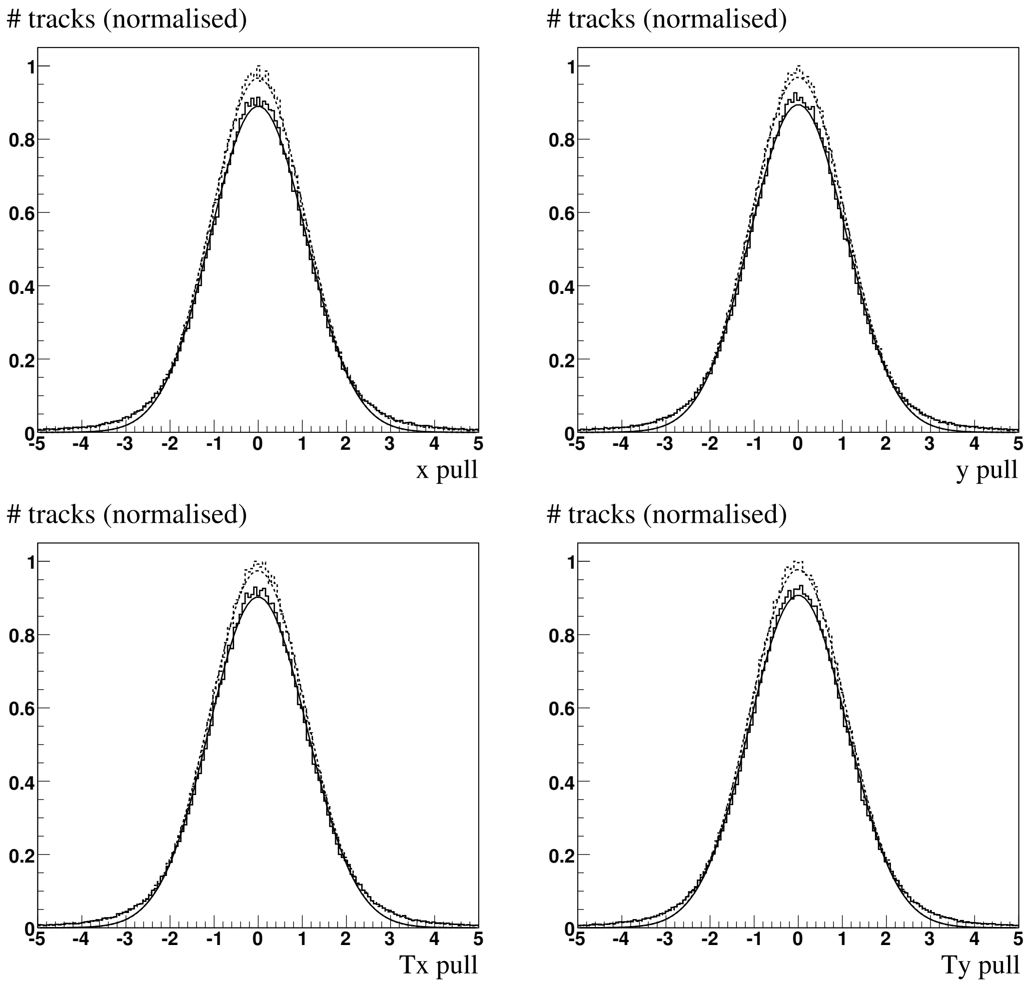

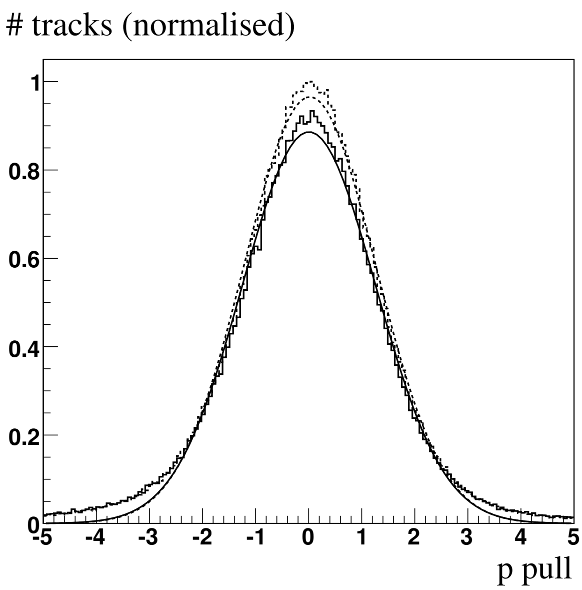

Figure 7.8: *Pull distributions of the track parameters of Long (solid) and Ideal Long (dashed) tracks at the vertex, fitted by Gaussian functions.*

detector, are listed for Long and Ideal Long tracks in table 7.10. Both track types have identical widths to within 1% for the VELO, TT and IT. The OT pulls differ a bit more on account of the fraction of incorrect L/R sign assignments of the Long track OT hits. The observed underestimation of the TT and OT coordinate and slope pulls is directly linked to the resolutions as seen in table 7.7. The error estimation of the track fit therefore is accurate to within 10%, except for the momentum.

Table 7.10: *Average Gaussian widths of the track parameter pull distributions for the different sub-detectors for Long and Ideal Long tracks. The uncertainty on these numbers is smaller than the last presented digit.*

sub-detector	x pull	y pull	t_x pull	t_y pull	p pull
VELO	1.01	1.04	1.07	1.07	1.25
TT	1.18	1.29	1.22	1.15	1.19
IT	0.93	1.02	1.16	1.22	1.21
OT	1.16	1.20	1.21	1.25	1.23
Ideal VELO	1.01	1.04	1.08	1.08	1.23
Ideal TT	1.18	1.29	1.21	1.13	1.17
Ideal IT	0.93	1.02	1.17	1.22	1.22
Ideal OT	1.10	1.13	1.19	1.22	1.20

The dependence of the coordinate and slope pull distribution widths on one over the transverse momentum is shown in figure 7.9. The width increases slightly for the coordinate pulls because of the VELO hit resolution decreasing with increasing slopes [54]. It remains about flat for the slope pulls. In the last two plots of that figure, the momentum pull width is shown as a function of momentum and pseudorapidity. Below five GeV the width decreases with momentum, after which is reaches a plateau. This shows that at low momenta, the errors on the momentum parameter are underestimated. As a function of pseudorapidity, the momentum pull width is seen to increase close to the edges of the acceptance, as fewer VELO hits are present on those tracks. Otherwise the distribution is about uniform with a peak at $\eta = 4.38$, which is due to multiple scattering when travelling a significant distance through the beam-pipe cone, see figure 4.5.

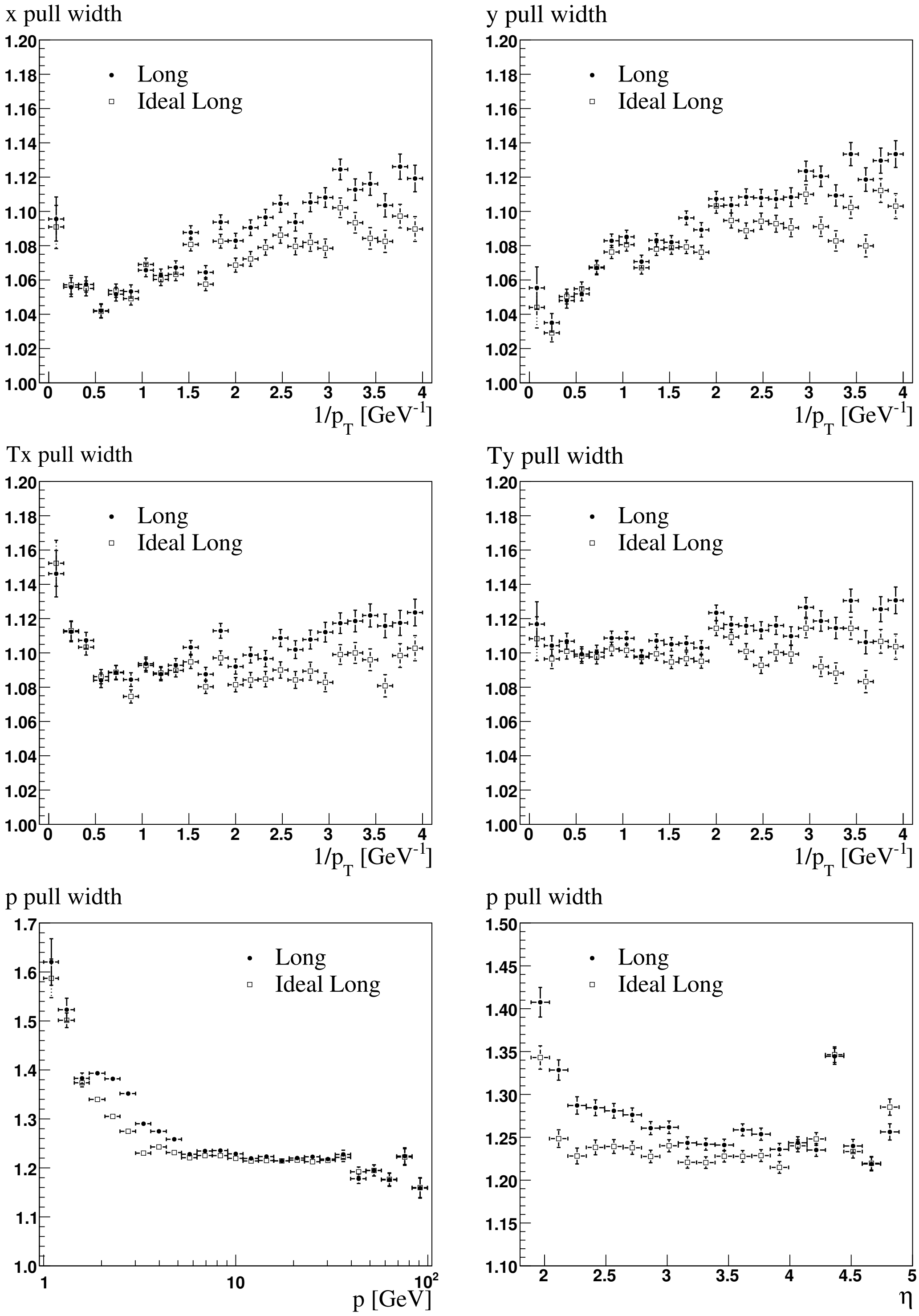

Figure 7.9: *Long and Ideal Long track parameter pull widths at the vertex, as a function of one over the transverse momentum, the momentum and the pseudorapidity.*

Chapter 8

Outlook

Reconstructed tracks provide position, direction, momentum and charge information as input to physics analyses of specific events. This is complemented by the energy and identity of a particle, as provided by the calorimeter system, RICH detectors, and muon chambers. As an example, the importance of accurate track reconstruction is illustrated in this outlook by inspecting the reconstructed invariant masses of the B_s^0 and D_s^- particles in $B_s^0 \to D_s^-\pi^+$ decays as well as the proper-time resolution of the reconstructed B_s^0 in these events.

Events containing a $B_s^0 \to D_s^-\pi^+$ decay are selected by running the default DC06 selection procedure for this channel [78]. As described in [110], the same procedure is used for events containing the $B_s^0 \to D_s^{\mp}K^{\pm}$ decay. These decays have a similar topology as shown in figure 8.1, specifying the decay products of the D_s^- as $K^-K^+\pi^-$.

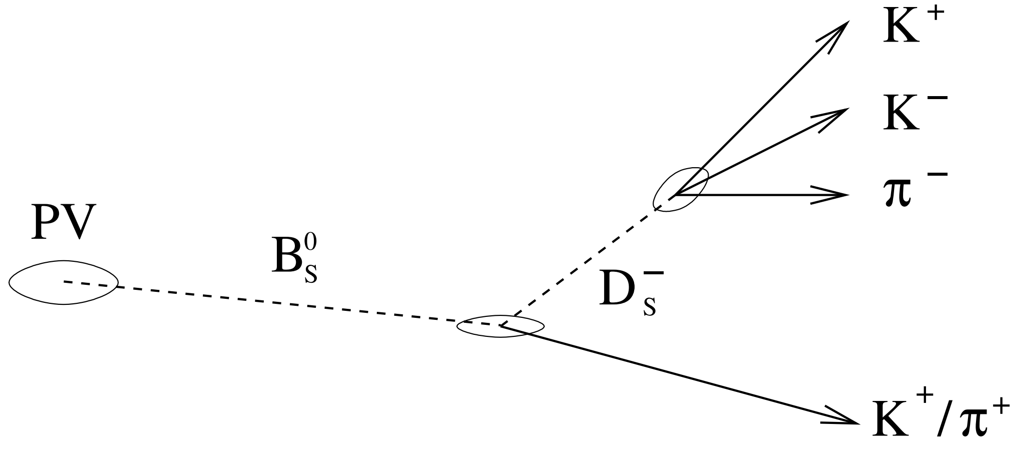

Figure 8.1: *Decay topology of $B_s^0 \to D_s^-\pi^+$ and $B_s^0 \to D_s^-K^+$ [58].*

8.1 Mass resolution

A D_s^- decaying into three particles is called a 3-prong decay. The four-vectors of the $K^-K^+\pi^-$ particles can be combined to calculate the invariant mass of the D_s^- as:

$$m_{D_s}^2 = m_1^2 + m_2^2 + m_3^2 + 2\,(E_1E_2 - p_1p_2\cos\theta_{12}) + \\ 2\,(E_1E_3 - p_1p_3\cos\theta_{13}) + 2\,(E_2E_3 - p_2p_3\cos\theta_{23}) \quad [\mathrm{MeV}^2]\,, \quad (8.1)$$

where $m_{1,2,3}$, $E_{1,2,3}$, and $p_{1,2,3}$ are the masses, energies, and momenta of the final state particles $K^-K^+\pi^-$ and $\theta_{\alpha\beta}$ are the angles between these particles.

This procedure results in the reconstructed invariant mass distribution shown in the first plot of figure 8.2. A sum of two Gaussian distributions is fitted to this distribution, with a weighted mean width, signifying the mass resolution, of 6.25±0.09 MeV. In the other two plots, the effects of using the true momentum or true slopes of the three tracks describing the decay products of the D_s^- on the reconstructed mass are shown. Using the true momentum reduces the mass resolution to 4.43±0.06 MeV, whereas using the true slopes results in a mass resolution of 3.85±0.05 MeV. These numbers illustrate that the momentum measurement across the magnet and the slope measurement in the VELO contribute in an approximately equal way to the mass measurement of the D_s^-. Applying a mass window cut on the D_s^- is a method to reject background in the analyses of $B_s^0 \to D_s^-\pi^+(K^+)$ events [58]. Improving the estimation of the momentum and slopes of tracks by the reconstruction, results in a reduced combinatorial background for D_s^- particles, given a $n\sigma$ wide window.

The invariant mass distribution of the reconstructed B_s^0 particles is shown in the first plot of figure 8.3. It is fitted by a double Gaussian, which results in a width of 17.45±0.27 MeV. In the second plot, the resolution is observed to improve to 7.48±0.11 MeV by using the MC momenta of the final state particles. Using the MC slopes in the determination of the invariant mass of the B_s^0 results in a resolution of 15.47±0.23 MeV. The momentum resolution becomes more important as the mass of the decaying particle increases, whereas the slope resolution becomes more important as the angle between the decay products decreases. For this decay channel, the mass of the B_s^0 causes the mass resolution to be dominated by the momentum resolution, while the slopes are the more influential of the two inspected parameters for the D_s^- mass resolution.

The pull distribution of the B_s^0 mass is shown in the left plot of figure 8.4. It is fitted by a Gaussian function with a width of 1.36±0.02, indicating that the errors are underestimated. This is consistent with the observed momentum pull width, see section 7.3, which is the dominant input as seen in figure 8.3. The event-by-event distribution of the errors is shown in the right plot of figure 8.4, in which the event errors are seen to vary with a range from 7 to 25 MeV, having a mean of 12.4±0.1 MeV.

$B_s^0 \to D_s^-K^+$ signal selection can suffer from $B_s^0 \to D_s^-\pi^+$ background decays in case of misidentification of the pion of the $B_s^0 \to D_s^-\pi^+$, confusing the decay for $B_s^0 \to D_s^-K^+$. In that scenario, the background can be reduced by cutting on the invariant mass of the B_s^0. Using the incorrect hypotheses of the pion being a

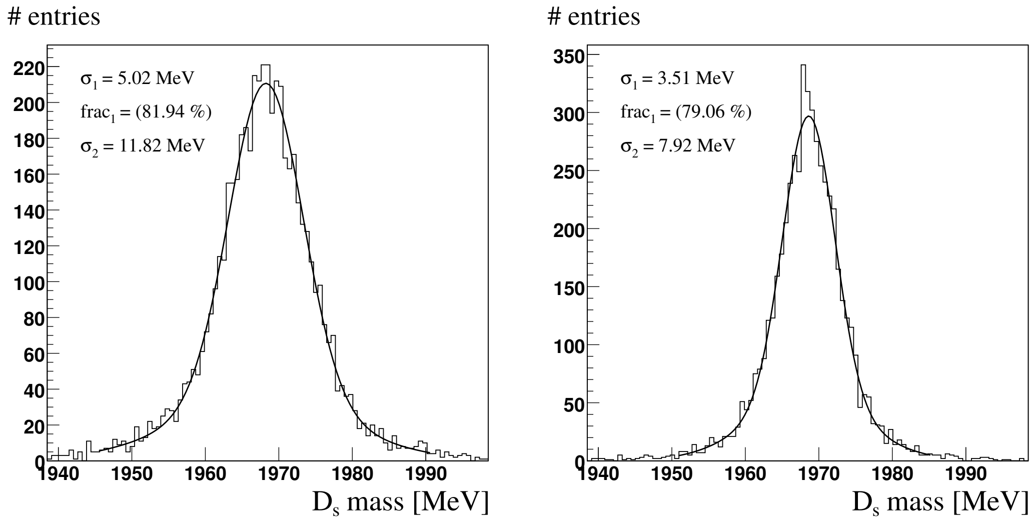

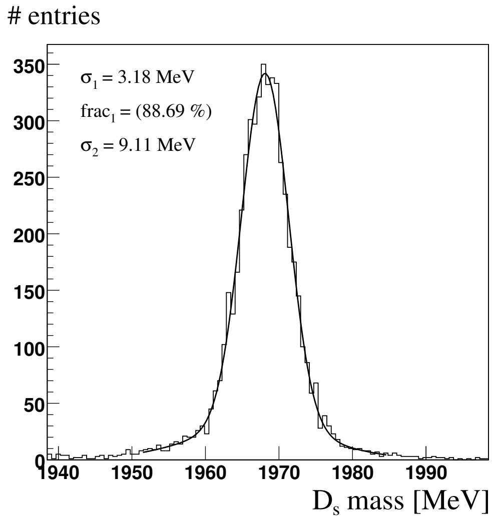

Figure 8.2: *Invariant mass distributions of the D_s^-, using the reconstructed momenta and slopes (**top left**), the MC momenta and reconstructed slopes (**top right**), and the reconstructed momenta and MC slopes (**bottom left**).*

kaon, results in the invariant mass distribution as shown, together with the invariant mass of the $B_s^0 \to D_s^- K^+$ decay, in plot 8.5. The mass peaks resulting from that analysis are located at 5370 MeV and 5409 MeV respectively. This offers a mass difference of 39 MeV, which is equivalent to over 2σ at a mass resolution of 17.45 MeV. Improving the B_s^0 mass resolution allows for a narrower mass window to be applied in the rejection of background in this scenario.

The momentum resolution is also the dominant factor for $B_{d,s}^0 \to h^+ h'^-$ decays, as seen in figure 6.2 of [129]. For these decays, the mass resolution is 23.33±0.78 MeV, decreasing to 6.93±0.21 MeV when using the true momenta, and when using the true slopes, the momentum resolution becomes 20.64±0.86 MeV.

Another example of the need for a good momentum resolution is given by the selection of $B_s^0 \to K^- \pi^+$ signal in the presence of $\overline{B}_d^0 \to K^- \pi^+$ background by means of a mass window [129]. In the plots of figure 8.6 the background is seen to become indistinguishable from the signal as the momentum resolution is increased to a value of 1%, whereas the nominal momentum resolution of 0.37% offers resolving power for these mass peaks.

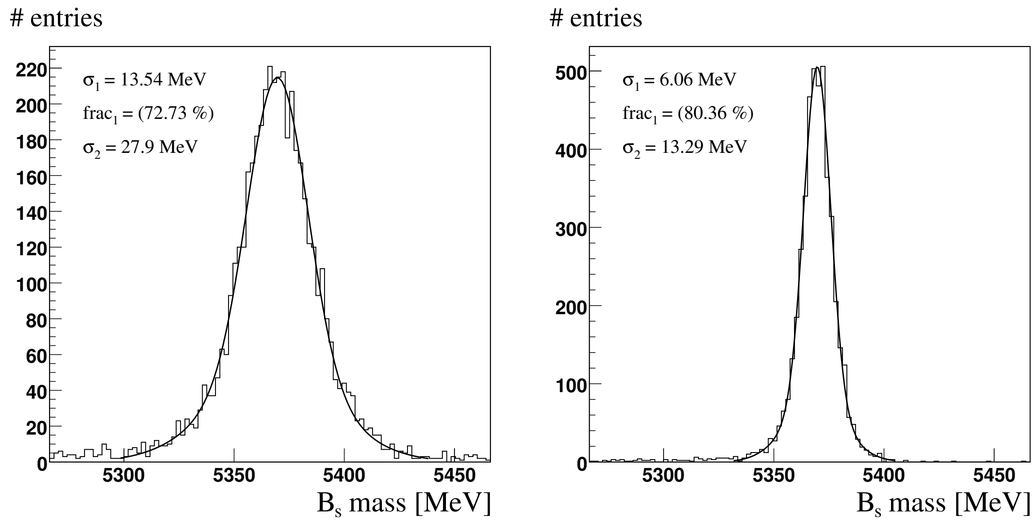

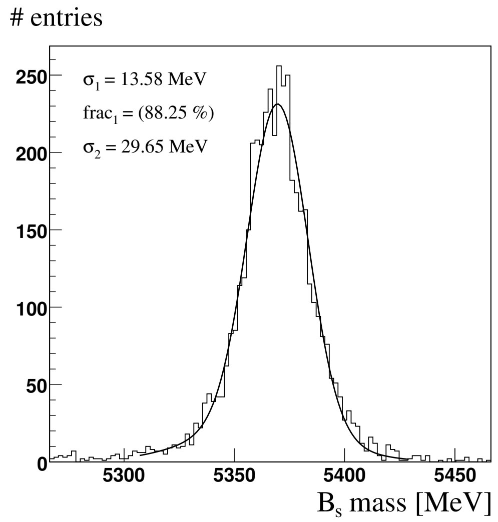

Figure 8.3: Invariant mass distributions of the B_s^0, using the reconstructed momenta and slopes (**top left**), the MC momenta and reconstructed slopes (**top right**), and the reconstructed momenta and MC slopes (**bottom left**).

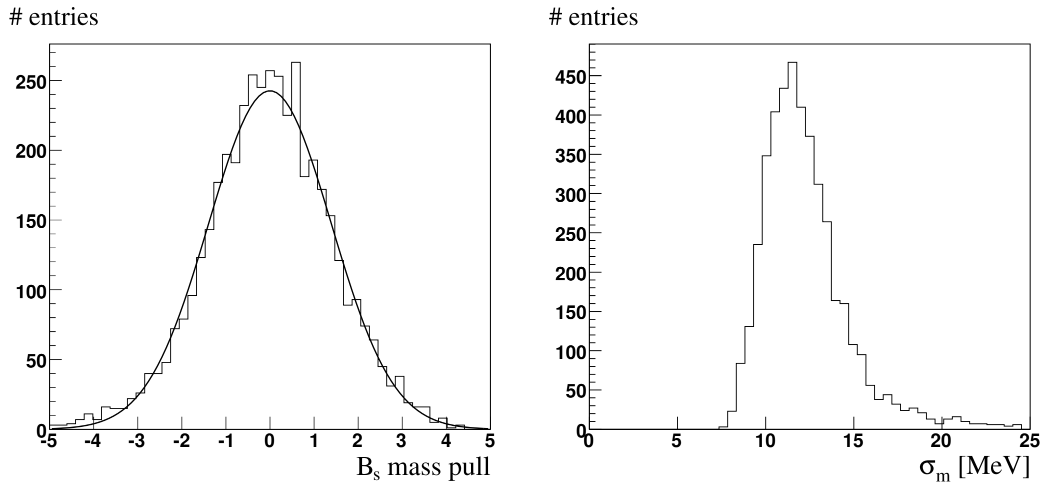

Figure 8.4: B_s^0 invariant mass pull distribution (**left**) and error distribution (**right**).

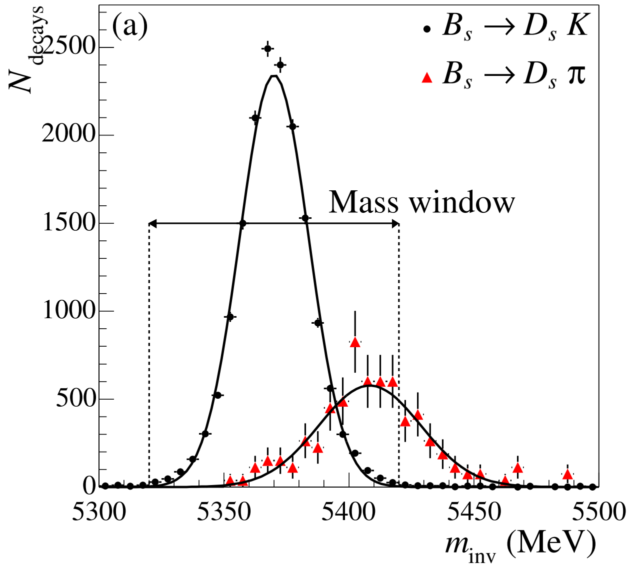

Figure 8.5: Invariant mass distribution for the B_s in $B_s^0 \to D_s^- K^+$ events with $B_s^0 \to D_s^- \pi^+$ background [58].

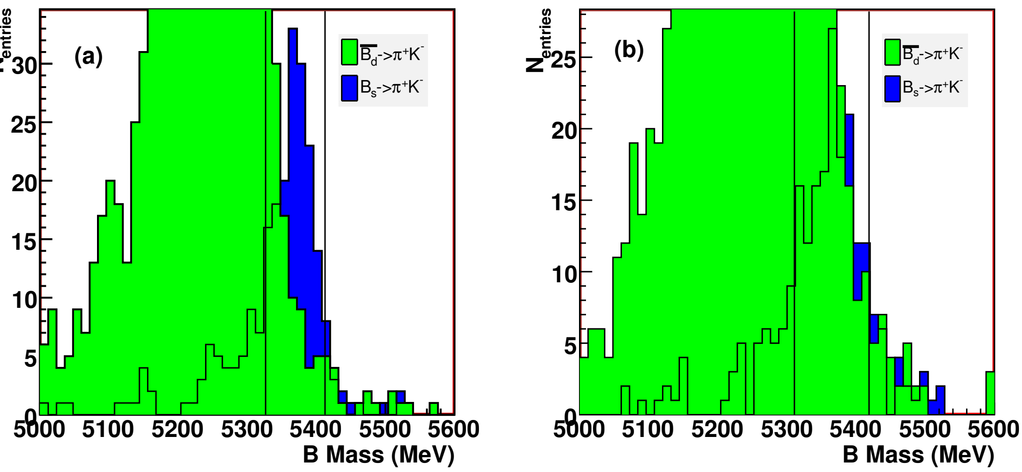

Figure 8.6: Invariant mass distributions of $B_s^0 \to K^- \pi^+$ signal and $\overline{B}_d^0 \to K^- \pi^+$ background at nominal momentum resolution of 0.4% (**left**) and at a 1% momentum resolution (**right**) [129].

8.2 Proper-time resolution

The performance of the track reconstruction also determines the accuracy of the reconstructed proper time of the B_s^0. The proper time t is given by:

$$t = m\frac{\vec{p}\cdot\vec{d}}{|\vec{p}|^2} \quad [\text{ps}]\,, \tag{8.2}$$

where m is the reconstructed mass, $\vec{d}$ is the reconstructed flight distance vector, and $\vec{p}$ is the reconstructed momentum vector of the B_s^0.

To understand the relative contributions of the momentum and distance measurements of the B_s^0, the plots of figure 8.7 show the proper-time resolution with and without the use of the true momentum or true flight distance. The resolution of the reconstructed proper time is 42.1±0.6 fs, which is compatible with the predicted average of 40 fs of subsection 3.3.2. This value remains unchanged (42.4±0.6 fs) by using the MC momenta of the final state particles. An improvement to a value of 2.8±0.1 fs is achieved by using the MC decay distance. This shows the resolution to be dominated by the quality of the reconstructed secondary vertex. This is determined using the slopes of the tracks which describe the decay products.

The proper-time pull distribution is shown in the left plot of figure 8.8. It is fitted by a Gaussian distribution with a width of 1.12±0.01. This indicates that the errors on the proper times are underestimated by 11%, which is consistent with the widths of the track slope pulls. The proper-time error distribution is shown in the right plot of figure 8.8. In the range from 0 to 100 fs, this distribution has a mean of 41 ± 0.5 fs.

The proper-time resolution σ_t is important for measurements of the time-dependent CP asymmetry in the B_s^0 system. For the $B_s^0 \to J/\psi\phi$ decay channel, this asymmetry is given by equation (2.42). Observation of the amplitude of this asymmetry is limited by the efficiency with which the initial flavour of the B_s^0 is tagged, and by the proper-time resolution. This leads to an observed asymmetry for the B_s^0 of [43]:

$$[\mathcal{A}_{CP}(t)]_{\text{observed}} = \left(1 - 2\omega_{\text{tag}}\right) e^{-(\Delta M_s \sigma_t)/2}\mathcal{A}_{CP}(t)\,, \tag{8.3}$$

where ω_{tag} is the wrong-tag probability. This asymmetry is predicted to be around 0.04 for $B_s^0 \to J/\psi\phi$ decays. In order to limit the dilution by the proper-time resolution, it needs to meet: $\sigma_t << 1/\Delta M_s$. Given the value of ΔM_s from section 2.3 of 17.77 ps^{-1}, the proper-time resolution needs to be well below 56.27 fs. Using the average reconstructed proper-time resolution of 42.1 fs, the dilution of the time-dependent CP asymmetry by the proper-time resolution is a factor of 0.76.

The dilution due to the proper-time resolution can be determined by inspecting $B_s^0 \to D_s^-\pi^+$ decays, which have been tagged using MC information. The decay rate of the B_s^0 in the $B_s^0 \to D_s^-\pi^+$ decays is defined by the first formula in equation (2.28), and is plotted in figure 8.9. The reconstructed and MC decay rates differ in amplitude by a factor of 0.78±0.06, which is close to the predicted value of 0.76. Fitting the decay rate allows to identify the value of ΔM_s with an error of 0.008 ps, and the value of ω_{tag} to within 0.03 [33].

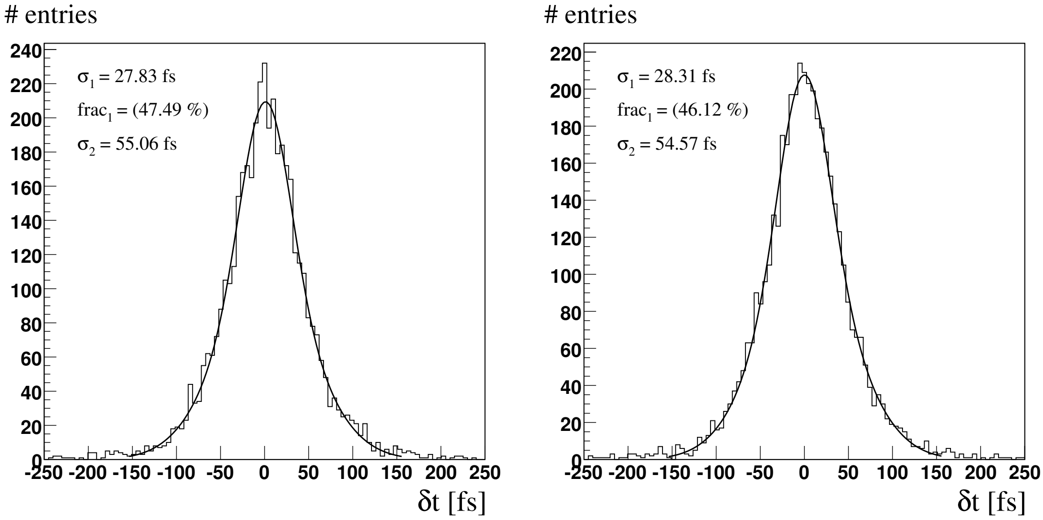

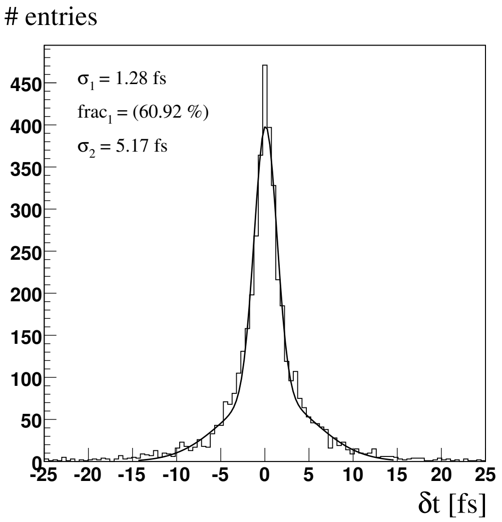

Figure 8.7: Proper-time residual distributions of the B_s^0, using the reconstructed momentum and decay distance (**top left**), the MC momentum and reconstructed decay distance (**top right**), and the reconstructed momentum and MC decay distance (**bottom left**).

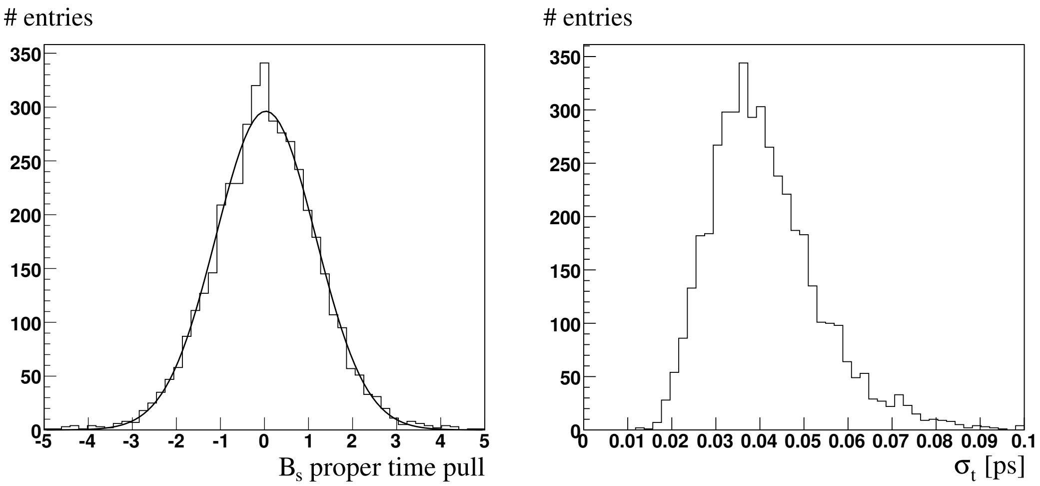

Figure 8.8: Proper-time pull distribution (**left**) and error distribution (**right**).

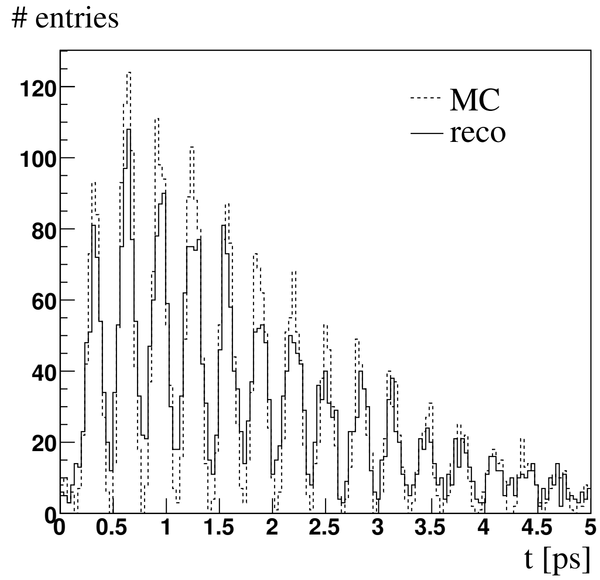

Figure 8.9: Decay rate for $B_s^0 \to D_s^- \pi^+$, superimposed om the MC decay rate.

8.3 Conclusion

The track reconstruction software is designed to efficiently identify which hits are created by individual particles. Identification of these groups of hits is performed per track type by dedicated track finding strategies. Depending on the mode of operation, concurrent or filtered, this approach can lead to multiple tracks being found for a given particle. After fitting the tracks, the optimal track per particle is made available for physics analysis on the reconstructed event.

The track model used in the fit is a description of the path of a particle through the detector. It takes into account the effects of traversing the inhomogeneous magnetic field and the various layers of material. The geometry of the detector and the track fit are independent due to the use of trajectories. This enables the track reconstruction to also be executed using data obtained by a misaligned detector. A Kalman filter is used to fit the hits to the track model. This filter is tuned with respect to the correct determination of L/R signs for OT hits, to the removal of outlier hits and to the ionisation energy parameter c_{ion}.

On average 85.2 tracks per events are reconstructed in generic B events. An average of 11.1% of the Long tracks are ghosts. Long tracks have an average hit efficiency of 91.9% at a purity of 99.3%. This results in accurate estimations of the track parameters. At the vertex, Long tracks have a typical coordinate resolution of 39 μm, a slope resolution of $3.5 \cdot 10^{-4}$, and a momentum resolution of 0.37%. Each of these values is within 5% of the corresponding values found for Ideal Long tracks which have their hit content determined through the use of MC truth information. The errors on the track parameters are somewhat underestimated, resulting in coordinate and slope pulls with widths around 1.1 and a momentum pull of 1.26 at the vertex. This issue is being addressed by improving on the estimation of hit errors and a study of the settings used in the treatment of material effects by Geant4.

High precision estimation of the track parameters is beneficial to the analysis of events. As an example, their impact on the resolution of the reconstructed invariant masses of the B_s^0 and D_s^- in $B_s^0 \to D_s^-\pi^+$ decays is shown. The momentum and slopes directly influence the mass resolution, reducing it from 17.45 MeV to 7.48 MeV (using the MC momenta) and 15.47 MeV (using the MC slopes) respectively. A small mass resolution is beneficial in the suppression of background by means of mass windows by distinguishing individual mass peaks in an invariant mass spectrum. In addition, the track parameter resolution impacts the proper-time resolution. A small proper-time resolution is important for the determination of the time-dependent *CP* asymmetry in the B_s^0 system. The reconstructed resolution of 42.1 fs leads to a dilution factor of the amplitude of 0.76, which is close to the observed factor of 0.78±0.06. The performance of the reconstruction allows for the extraction of the parameters ΔM_s, $\Delta\Gamma_s$ and ϕ_s from the $B_s^0 \to D_s^-\pi^+$, $B_s^0 \to J/\psi\phi$ and $B_s^0 \to J/\psi\eta$ decay channels. An improvement of the knowledge of the parameter γ is expected by studying the $B_s^0 \to D_s^{\mp}K^{\pm}$, $B^0 \to D^0K^{*0}$, $B^{\pm} \to D^0K^{\pm}$, $B^0 \to \pi^+\pi^-$ and $B_s^0 \to K^+K^-$ decay channels.

Bibliography

[1] G.C. Branco, L. Lavoura and J.P. Silva, *CP Violation*, Oxford University Press, 1999.

[2] R. Fleischer, *Flavour Physics and CP Violation: Expecting the LHC*, hep-ph/0802.2882 (2008).

[3] P.W. Higgs, *Broken symmetries, massless particles and gauge fields*, Phys. Lett. **12** (1964), no. 2, 132–133.

[4] C. Amsler *et al.* (Particle Data Group), *The Review of Particle Physics*, Phys. Lett. B **667** (2008), no. 1.

[5] F. Englert and R. Brout, *Broken Symmetry and the Mass of Gauge Vector Mesons*, Phys. Rev. Lett. **13** (1964), no. 9, 321–323.

[6] N. Cabibbo, *Unitary Symmetry and Leptonic Decays*, Phys. Rev. Lett. **10** (1963), no. 12, 531–533.

[7] M. Kobayashi and T. Maskawa, *CP-Violation in the Renormalizable Theory of Weak Interaction*, Prog. Theor. Phys. **49** (1973), no. 2, 652–657.

[8] C.S. Wu *et al.*, *Experimental Test of Parity Conservation in Beta Decay*, Phys. Rev. **105** (1957), no. 4, 1413–1415.

[9] J.H. Christenson *et al.*, *Evidence for the* 2π *Decay of the* K_2^0 *Meson*, Phys. Rev. Lett. **13** (1964), no. 4, 138–140.

[10] B. Aubert *et al.* (BABAR Collaboration), *Observation of CP Violation in the* B^0 *Meson System*, Phys. Rev. Lett. **87** (2001), no. 9, 091801.

[11] K. Abe *et al.* (Belle Collaboration), *Observation of Large CP Violation in the Neutral B Meson System*, Phys. Rev. Lett. **87** (2001), no. 9, 091802.

[12] S.L. Glashow, J. Iliopoulos and L. Maiani, *Weak Interactions with Lepton-Hadron Symmetry*, Phys. Rev. D **2** (1970), no. 7, 1285–1292.

[13] C. Jarlskog, *Commutator of the Quark Mass Matrices in the Standard Electroweak Model and a Measure of Maximal CP Nonconservation*, Phys. Rev. Lett. **55** (1985), no. 10, 1039–1042.

[14] L. Wolfenstein, *Parametrization of the Kobayashi-Maskawa Matrix*, Phys. Rev. Lett. **51** (1983), no. 21, 1945–1947.

[15] N. Cabibbo, *Unitary Symmetry and Leptonic Decays*, Phys. Rev. Lett. **10** (1963), no. 12, 531–533.

[16] R. Aleksan, B. Kayser and D. London, *Determining the Quark Mixing Matrix from CP-violating Asymmetries*, Phys. Rev. Lett. **73** (1994), no. 1, 18–20.

[17] J. Charles *et al.* (CKMfitter Group), *CP violation and the CKM matrix: assessing the impact of the asymmetric B factories*, Eur. Phys. J. C **41** (2005 (updated to 2009 preliminary results)), 1–131.

[18] C. Jarlskog and R. Stora, *Unitarity polygons and CP violation areas and phases in the standard electroweak model*, Phys. Lett. B **208** (1988), no. 2, 268–274.

[19] B. Aubert *et al.* (BABAR Collaboration), *Measurement of the CP Asymmetry Amplitude* $\sin 2\beta$ *with B Mesons*, Phys. Rev. Lett. **89** (2002), no. 20.

[20] K. Abe *et al.* (BELLE Collaboration), *Measurement of CP-violation parameter* $\sin(2\phi_1)$ *with 152 million B anti-B pairs*, hep-ex/0308036 (2003).

[21] K. Chadwick *et al.* (CLEO Collaboration), *Decay of b-Flavored Hadrons to Single-Muon and Dimuon Final States*, Phys. Rev. Lett. **46** (1981), no. 2, 88–91.

[22] L. J. Spencer *et al.* (CUSB Collaboration), *Measurement of B-Meson Semileptonic Decay*, Phys. Rev. Lett. **47** (1981), no. 11, 771–774.

[23] E. Fernandez *et al.* (MAC Collaboration), *Lifetime of Particles Containing b Quarks*, Phys. Rev. Lett. **51** (1983), no. 12, 1022–1025.

[24] N. S. Lockyer *et al.* (MARK II Collaboration), *Measurement of the Lifetime of Bottom Hadrons*, Phys. Rev. Lett. **51** (1983), no. 15, 1316–1319.

[25] H. Albrecht *et al.* (ARGUS Collaboration), *Observation of B0 - anti-B0 Mixing*, Phys. Lett. B **192** (1987), 245.

[26] A. Abulencia *et al.* (CDF Collaboration), *Observation of* $B_s^0-\bar{B}_s^0$ *Oscillations*, Phys. Rev. Lett. (2006), no. 24, 242003.

[27] V. M. Abazov *et al.* (D0 Collaboration), *Direct Limits on the* B_s^0 *Oscillation Frequency*, Phys. Rev. Lett. **97** (2006), no. 2, 021802.

[28] E. Barberio *et al.* (Heavy Flavor Averaging Group), *Averages of b-hadron and c-hadron Properties at the End of 2007*, hep-ex/0808.1297v1 (2008).

[29] V.M. Abazov *et al.* (D0 Collaboration), *Lifetime Difference and CP-Violating Phase in the* B_s^0 *System*, Phys. Rev. Lett. **98** (2007), 121801.

[30] T. Aaltonen *et al.* (CDF Collaboration), *Measurement of Lifetime and Decay-Width Difference in $B_s^0 \to J/\psi\phi$ Decays*, Phys. Rev. Lett. **100** (2008), 121803.

[31] B. Aubert *et al.* (BABAR Collaboration), *Direct CP Violating Asymmetry in $B \to K^+\pi^-$ Decays*, Phys. Rev. Lett. **93** (2004), no. 13, 131801.

[32] K. Abe *et al.* (BELLE Collaboration), *Observation of Large CP Violation and Evidence for Direct CP Violation in $B \to \pi^+\pi-$ Decays*, Phys. Rev. Lett. **93** (2004), no. 2, 021601.

[33] J. Borel, *The analog readout of the LHCb vertex detector and study of the measurement of the B_s oscillation frequency*, EPFL, 2009.

[34] $\gamma + \phi_s$ sensitivity studies from combined $B_s^0 \to D_s^-\pi^+$ and $B_s^0 \to D_s^{\mp}K^{\pm}$ samples at LHCb, *S. Cohen, M. Merk and E. Rodrigues*, CERN/LHCC 2007-041 (2007).

[35] L. Fernandez, *Sensitivity to the $B_s - \overline{B}_s$ mixing phase at LHCb*, CERN/LHCC 2006-047 (2006).

[36] R. Fleisher, *New strategies to extract β and γ from $B_d^0 \to \pi^+\pi^-$ and $B_s^0 \to K^+K^-$*, Phys. Lett. B (1999), no. 459.

[37] K. Akiba and M. Gandelman, *Estimate of LHCb's sensitivity to the CKM angle γ using $B_d^0 \to D^0K^{*0}$ decays*, CERN/LHCC 2007-050 (2007).

[38] A. Carbone *et al.*, *Charmless charged two-body B decays at LHCb*, CERN/LHCC 2007-059 (2007).

[39] The LHC Study Group, *The Large Hadron Collider Conceptual Design*, Tech. report, CERN, 1995, CERN/LHCC 1995-005.

[40] LHCb Collaboration, *A Dedicated LHC Collider Beauty Experiment for Precision Measurements of CP-Violation*, Letter of Intent, CERN, August 1995, CERN/LHCC 95-5.

[41] L. Evans and P. Bryant, *LHC Machine*, JINST **3** (2008), no. S08001.

[42] O.S. Brüning *et al.*, *The LHC design report v.1 : the LHC Main Ring*, Tech. Report CERN-2004-003-V-1, CERN, 2004.

[43] LHCb Collaboration, *A Large Hadron Collider Beauty Experiment for Precision Measurements of CP-Violation and Rare Decays*, Technical Proposal, CERN, Februari 1998, CERN/LHCC 1998-004.

[44] CMS Collaboration, *Technical Proposal*, Tech. report, CERN, 1994, CERN/LHCC 1994-038.

[45] S. Chatrchyan *et al.* (CMS Collaboration), *The CMS Experiment at the CERN LHC*, JINST **3** (2008), no. S08004.

[46] ATLAS Collaboration, *Technical Proposal for a General-Purpose pp Experiment at the Large Hadron Collider at CERN*, Technical Proposal, CERN, 1994, CERN/LHCC 1994-043.

[47] G. Aad *et al.* (ATLAS Collaboration), *The ATLAS Experiment at the CERN Large Hadron Collider*, JINST **3** (2008), no. S08003.

[48] ALICE Collaboration, *A Large Ion Collider Experiment*, Technical Proposal, CERN, 1995, CERN/LHCC 1995-071.

[49] K. Aamodt *et al.* (ALICE Collaboration), *The ALICE Experiment at the CERN LHC*, JINST **3** (2008), no. S08002.

[50] LHCf Collaboration, *Technical Design Report*, Tech. report, CERN, 2006, CERN/LHCC 2006-004.

[51] O. Adriani *et al.* (LHCf Collaboration), *The LHCf Detector at the CERN Large Hadron Collider*, JINST **3** (2008), no. S08006.

[52] TOTEM Collaboration, *Technical Proposal*, Tech. report, CERN, 1999, CERN/LHCC 1999-007.

[53] G. Anelli *et al.* (TOTEM Collaboration), *The TOTEM Experiment at the CERN Large Hadron Collider*, JINST **3** (2008), no. S08007.

[54] A. Augusto Alves Jr *et al.* (LHCb Collaboration), *The LHCb Detector at the LHC*, JINST **3** (2008), no. S08005.

[55] LHCb Collaboration, *Reoptimized Detector Design and Performance*, TDR 9, CERN, September 2003, CERN/LHCC 2003-030.

[56] LHCb Collaboration, *Magnet*, TDR 1, CERN, Januari 2000, CERN/LHCC 2000-007.

[57] LHCb Collaboration, *VELO*, TDR 5, CERN, May 2001, CERN/LHCC 2001-011.

[58] J. van Tilburg, *Track simulation and reconstruction in LHCb*, Vrije Universiteit, 2005.

[59] LHCb Collaboration, *Outer Tracker*, TDR 6, CERN, September 2001, CERN/LHCC 2001-024.

[60] LHCb Collaboration, *RICH*, TDR 3, CERN, September 2000, CERN/LHCC 2000-037.

[61] F.C.D. Metlica *et al.*, *The LCHb detector and triggers*, Nuclear Physics B (2007), no. 167, 173–176.

[62] K. Kleinknecht, *Detectors for Particle Radiation*, 2 ed., Cambridge University Press, 1998.

[63] LHCb Collaboration, *Calorimeters*, TDR 2, CERN, September 2000, CERN/LHCC 2000-036.

[64] R. Djeliadine, O. Iouchtchenko and V.F. Obraztsov, *LHCb hadron trigger and HCAL cell size and length optimisation*, LHCb-1999-035 (1999).

[65] LHCb Collaboration, *Muon System*, TDR 4, CERN, May 2001, CERN/LHCC 2001-010.

[66] R Santacesaria G Martellotti and A Satta, *Particle rates in the lhcb muon detector*, LHCb 2005-075 (2005).

[67] LHCb Collaboration, *Second Addendum to the Muon System Technical Design Report*, CERN/LHCC 2005-012 (2005).

[68] LHCb Collaboration, *Trigger System*, TDR 10, CERN, September 2003, CERN/LHCC 2003-031.

[69] E. Aslanides *et al.*, *The level-0 muon trigger for the LHCb experiment*, Nucl. Instrum. Meth. A **579** (2007), no. 3.

[70] R.H. Hierck, *Optimisation of the LHCb detector*, Ph.D. thesis, Nikhef, 2003.

[71] G. Barrand *et al.*, *GAUDI - A software architecture and framework for building LHCb data processing applications*, Comput. Phys. Commun. (2001), no. 140, 45.

[72] I. Belyaev *et al.*, *Simulation application for the LHCb experiment*, physics/0306035 (2003).

[73] T. Sjöstrand, L. Lönnblad, and S. Mrenna, *PYTHIA 6.4 - Physics and Manual*, hep-ph/0603175 (2006).

[74] D.J. Lange, *The EvtGen particle decay simulation package*, Nucl. Instr. and Methods A (2001), no. 462.

[75] S.Agostinelli *et al.* (GEANT4 Collaboration), *Geant4: A simulation toolkit*, Nucl. Instrum. Meth. A (2003), no. 506.

[76] *The BOOLE Project*, http://lhcb-release-area.web.cern.ch/LHCb-release-area/DOC/boole/.

[77] *The BRUNEL Project*, http://lhcb-release-area.web.cern.ch/LHCb-release-area/DOC/brunel/.

[78] *The DAVINCI Project*, http://lhcb-release-area.web.cern.ch/LHCb-release-area/DOC/davinci/.

[79] *The BENDER Project*, http://lhcb-release-area.web.cern.ch/LHCb-release-area/DOC/bender/.

[80] *LoKi*, http://lhcb-comp.web.cern.ch/lhcb-comp/Analysis/Loki/.

[81] *The PANORAMIX Project*, http://lhcb-release-area.web.cern.ch/LHCb-release-area/DOC/panoramix/.

[82] F. Bergsma, *Calibration of Hall sensors in three dimensions*, 13th Int. Magnetic Measurement Workshop (2003).

[83] M. Losasso *et al.*, *Tests and Field Map of LHCb Dipole Magnet*, IEEE Transactions on Applied Superconductivity **16** (2006), no. 2, 1700–1703.

[84] A. Hicheur and G. Conti, *Parameterization of the LHCb Magnetic Field Map*, CERN/LHCC LHCb 2007-093 (2007).

[85] Geant4 Collaboration, *Physics Reference Manual*, http://geant4.web.cern.ch/geant4/support/userdocuments.shtml.

[86] H.W. Lewis, *Multiple Scattering in an Infinite Medium*, Phys. Rev. **78** (1950), 526–529.

[87] G.Z. Molière, , Z. Naturforsch. **3a** (1948), 78.

[88] S. Goudsmit and J.L. Saunderson, , Phys. Rev. **57** (1940), 24.

[89] J.M. Fernández-Varea *et al.*, *On the theory and simulation of multiple elastic scattering of electrons*, NIM **B73** (1993), 447–473.

[90] V.L. Highland, *Some practical remarks on multiple scattering*, NIM **129** (1975), 497–499.

[91] G.R. Lynch and O.I. Dahl, *Approximations to multiple Coulomb scattering*, NIM **B58** (1991), 6–10.

[92] G. Shen *et al.*, , Phys. Rev. D **20** (1979).

[93] J.M. Fernandez-Varea *et al.*, *On the theory and simulation of multiple elastic scattering of electrons*, NIM B (1993), no. 73, 447–473.

[94] H. Bethe and W. Heitler, *On the Stopping of Fast Particles and on the Creation of Positive Electrons*, Proceedings of the Royal Society of London. Series A **146** (1934), 83–112.

[95] Y. Tsai, *Pair production and bremsstrahlung of charged leptons*, Rev. Mod. Phys. **46** (1974), 815–851.

[96] H. Davies, H.A. Bethe and L.C. Maximon, , Phys. Rev. **93** (1954).

[97] R. Hierck *et al.*, *Particle Interactions in the LHCb detector*, CERN/LHCC LHCb 2001-090 (2001).

[98] M. Needham, T. Ruf, *Estimation of the material budget of the LHCb detector*, CERN/LHCC LHCb 2007-025 (2007).

[99] E. Rodrigues, *Tracking Definitions*, CERN/LHCC LHCb 2007-006 (2007).

[100] D. Hutchcroft, *VELO Pattern Recognition*, CERN/LHCC LHCb 2007-013 (2007).

[101] R. Forty and M. Needham, *Standalone Track Reconstruction in the T-stations*, CERN/LHCC LHCb 2007-022 (2007).

[102] R. Forty and M. Needham, *Updated Performance of the T-Seeding*, CERN/LHCC LHCb 2007-023 (2007).

[103] O. Callot and S. Hansmann-Menzemer, *The Forward Tracking: Algorithm and Performance Studies*, CERN/LHCC LHCb 2007-015 (2007).

[104] P.V.C. Hough, *Machine Analysis of Bubble Chamber Pictures*, Proc. int. Conf. High Energy Accelerators and Instruments (1959).

[105] M. Needham and J. van Tilburg, *Performance of the track matching*, CERN/LHCC LHCb 2007-020 (2007).

[106] M. Needham, *Performance of the track matching*, CERN/LHCC LHCb 2007-129 (2007).

[107] W.H. Press *et al.*, *Numerical Recipes 3rd Edition: The Art of Scientific Computing*, Cambridge University Press, 2007.

[108] O. Callot, M. Kucharczyk and M. Witek, *VELO-TT track reconstruction*, CERN/LHCC LHCb 2007-010 (2007).

[109] O. Callot, *Downstream Pattern Recognition*, CERN/LHCC LHCb 2007-026 (2007).

[110] J. Borel *et al.*, *The $B_s \to D_s^- \pi^+$ and $B_s \to D_s^- \pi^+$ selections*, CERN/LHCC LHCb 2007-017 (2007).

[111] prof. dr. M.H.M. Merk, *Private communication.*

[112] dr. H.G. Raven, *Private communication.*

[113] J. Amoraal, *PhD thesis under preparation*.

[114] M. Gersabeck, E. Rodrigues, and J. Nardulli, *Impact of misalignments on the analysis of B decays*, CERN/LHCC LHCb 2008-012 (2008).

[115] R.E. Kalman, *A New Approach to Linear Filtering and Prediction Problems*, ASME Journal of Basic Engineering **D82** (1960), 35–45.

[116] R. Früwirth, *Application of Kalman Filtering to Track and Vertex Fitting*, NIM A **262** (1987), 444–450.

[117] R.K. Bock *et al.*, *Data analysis techniques for high-energy physics experiments*, Cambridge University Press, 1990.

[118] C. Runge, , Math. Ann. **46** (1895), no. 167.

[119] M.W. Kutta, , Z. für Math. u. Phys. **46** (1901), no. 435.

[120] A. Ralston and H.S. Wilf, *Mathematical Methods for Digital Computers*, New York: Wiley, 1960.

[121] J.R. Cash and A.H. Karp, *A variable order Runge-Kutta method for initial value problems with rapidly varying right-hand sides*, ACM Trans. Math. Softw. **16** (1990), no. 3, 201–222.

[122] S. Gorbunov and I. Kisel, *Analytic formula for track extrapolation in non-homogeneous magnetic field*, NIM A **559** (2006), 148–152.

[123] R. Mankel, *Application of the Kalman Filter Technique in the HERA-B Track Reconstruction*, HERA-B public note (1995).

[124] dr. A. Pellegrino, *Private communication.*

[125] D.N. Brown, W.A. Charles and D.A. Douglas, *The BaBar Track Fitting Algorithm*, Proceedings of CHEP 2000 (2000).

[126] E. Bos *et al.*, *The Trajectory Model for Track Fitting and Alignment*, CERN/LHCC LHCb 2007-008 (2007).

[127] E. Rodrigues, *Dealing with Clones in the Tracking*, CERN/LHCC LHCb 2006-057 (2006).

[128] Characterisation and commissioning of the LHCb VELO detector, *A. Papadelis*, Vrije Universiteit, 2009.

[129] J. Nardulli, *Reconstruction of two-body B decays in LHCb*, Vrije Universiteit, 2007.

Summary

Particle physicists study the elementary particles and their interactions. The electromagnetic, weak and strong forces act between the various leptons and quarks, depending on their electric charge, weak isospin, and colour charge, by means of mediating gauge bosons. In the Standard Model, the electroweak interactions are treated by the GSW model and the strong force is described by QCD. In some weak decays, charge conjugation and parity are violated, as well as their combined operation. *CP* violation is one of the Sakharov conditions for a matter-antimatter imbalance, which is observed in the universe.

CP violation is embedded in the flavour structure of weak charged-current interactions. Those interactions convert up-type quark mass eigenstates into a superposition of down-type quark electroweak eigenstates, and vice versa, as prescribed by the CKM matrix. In the Wolfenstein parameterisation, this matrix is described by three rotation angles and one complex phase, the latter being the source of *CP* violation. Neutral *B* mesons can oscillate to and from their antiparticle state, which is referred to as mixing. This occurs in weak neutral interactions, where the mass eigenstates are linear combinations of the weak eigenstates. A difference between mass and weak eigenstates leads to a different transition probability from meson to anti-meson then from anti-meson to meson, being *CP* violation in mixing. *CP* violation in decay occurs when the decay amplitudes of *CP*-conjugate states are unequal. A third form of *CP* violation is found in the interference between mixing and decay amplitudes.

The LHC will offer proton-proton collisions for tests of the Standard Model and searches for additional physics at a centre-of-mass energy of 14 TeV and a design luminosity of $10^{34}\mathrm{cm}^{-2}\mathrm{s}^{-1}$. LHCb specialises in heavy-flavour physics, including the search for new physics in *CP* violation, and rare decays of beauty and charm hadrons. It is the intention of LHCb to make detailed measurements of $B_s^0 - \overline{B}_s^0$ mixing, using channels like $B_s^0 \to D_s^- \pi^+$, $B_s^0 \to J/\psi\phi$ and $B_s^0 \to J/\psi\eta$, in order to precisely determine the parameters ΔM_s, $\Delta\Gamma_s$ and ϕ_s. LHCb aims to improve the knowledge of the angle γ, while at the same time searching for signs of new physics. An approach of combining measurements of γ from tree-level only *B* decays, such as $B_s^0 \to D_s^\mp K^\pm$, $B^0 \to D^0 K^{*0}$ and $B^\pm \to D^0 K^\pm$, with those including box or penguin contributions, like $B^0 \to \pi^+\pi^-$ and $B_s^0 \to K^+K^-$, is adopted. A difference between these measurements of γ may be due to new physics, present as virtual particles in the loop diagrams. From this perspective, the $B_s^0 \to D_s^\mp K^\pm$, $B_s^0 \to J/\psi\phi$ and $B_{(s)}^0 \to h^+h'^-$ decays are to be inspected.

The decay products of interest are predominantly present in two identical cones

around the beam-line, leading to a single-arm spectrometer design. LHCb has a silicon tracking detector or VELO to determine primary and secondary vertices. An integrated magnetic field of 4 Tm is used to bend charged particles, whose paths are further recorded by the TT, IT, and OT tracking sub-detectors. This allows for the momentum and charge of a particle to be determined. Particle identification and energy determination are facilitated by two RICH detectors, the electromagnetic and hadronic calorimeters and the muon system.

Both in the design of the detector and in the development of the software for the LHCb experiment, Monte Carlo simulation software is used. It offers a preview of what actual data can look like, and of the detector performance in various scenarios. This allows for fine tuning of reconstruction software and provides insight into the physics potential of LHCb.

The path of a charged particle through the LHCb detector is reconstructed from the hits that it causes in the position sensitive tracking sub-detectors. It is the purpose of the pattern recognition algorithms to determine which groups of hits belong to individual particles. The pattern recognition logic first determines the upstream or downstream starting points in the VELO or the T stations. These seeds are subsequently complemented by hits from the other tracking sub-detectors. In general, the pattern recognition algorithms aim to efficiently identify tracks, while examining as few combinations of hits as possible. To this end, they use cuts which have been tuned on Monte Carlo data.

Hits are fitted to a track model using a least-squares method, formulated as a Kalman filter. The track model is composed of extrapolation equations which account for the magnetic field, to which corrections for multiple scattering and energy loss are applied. The fit uses geometry information to identify the location of hits and material layers. Trajectories form an abstraction layer between the detector geometry description and the track reconstruction software. It eliminates the need to reformulate reconstruction equations upon a change in the geometry description. The Kalman filter is formulated with an averaging step in stead of a smoother step, making it more efficient and numerically stable. The fit procedure results in optimal estimates of the track parameters at discrete locations.

The track reconstruction produces in a final track sample of 85.2±0.05 tracks. Of these 25.4±0.05 are Long tracks, which are the main track type used for physics analyses. Long tracks contain on average 36.0±0.05 hits of the various tracking sub-detectors. The width of residual pull distributions of these hits is sensitive to misalignments and therefore offers an indication of detector alignment. Long track hit finding efficiency is 91.9±0.05% after outlier removal iterations, at a purity of 99.3±0.05%. At the reconstructed vertex, a Long track has a momentum resolution of 0.37±0.005% and a position resolution of 39.0±0.05μm. The coordinate and slope pulls are 10% too wide and the momentum pull is 25% too wide at the vertex, which leaves room for improvement. This issue is being addressed by improving on the estimation of hit errors and a study of the settings used in the treatment of material effects by Geant4.

Reconstructed tracks provide position, direction, momentum and charge information as input to physics analyses. The accuracy of the estimated slopes and momenta at a decay vertex influences the mass resolution of the mother particle. In case of $B_s^0 \to D_s^- \pi^+$ decays, the B_s^0 mass resolution of 17.45±0.27 MeV is dominated by the momentum resolution, whereas the 6.25±0.09 MeV mass resolution of the D_s^- is dominated by the slope resolution. Misidentifying a pion as a kaon in a $B_s^0 \to D_s^- \pi^+$ decay results in background for a $B_s^0 \to D_s^\mp K^\pm$ analysis. The track reconstruction offers a 2σ mass difference between the respective B_s^0 mass peaks for rejection of this background.

The proper-time resolution of the B_s^0 in $B_s^0 \to D_s^- \pi^+$ decays is 42.1±0.6 fs. A small proper-time resolution is important for measurements of the time-dependent CP asymmetry in the B_s^0 system. It dilutes the asymmetry measurement by a factor of 0.78±0.06 for $B_s^0 \to D_s^- \pi^+$ decays. Fitting the decay rate allows to identify the value of ΔM_s with an error of 0.008 ps, and the value of $\omega_{\rm tag}$ to within 0.03.

Reconstructie van geladen deeltjes in het LHCb experiment

Deeltjesfysici bestuderen de elementaire deeltjes en hun interacties. De elektromagnetische, zwakke en sterke krachten werken tussen de verschillende leptonen en quarks, afhankelijk van hun elektrische lading, zwakke isospin en kleur lading, middels ijkbosonen. In het Standaard Model worden de elektromagnetische interacties door het GSW model behandeld en wordt de sterke kracht beschreven door QCD. In sommige zwakke interacties worden ladingsconjugatie en pariteit geschonden, zowel als hun gecombineerde werking. *CP* schending is één van de Sakharov voorwaarden voor een materie-antimaterie onbalans, zoals geobserveerd is in het universum.

CP schending zit ingebed in de smaakstructuur van de zwakke geladen-stroom interacties. Die interacties converteren omhoog-type quark massa-eigentoestanden in een superpositie van omlaag-type quark elektrozwakke-eigentoestanden, en andersom, zoals voorgeschreven door de CKM matrix. In de Wolfenstein parameterisatie wordt deze matrix beschreven door drie rotatie hoeken en één imaginaire fase, waarvan de laatste de bron van *CP* schending is. Neutrale *B* mesonen kunnen van en naar hun antideeltjestoestand oscilleren, waar naar gerefereerd wordt als mixen. Dit gebeurt in zwakke neutrale interacties, waar de massa-eigentoestanden lineaire combinaties van zwakke-eigentoestanden zijn. Een verschil tussen massa- en zwakke-eigentoestanden leidt tot een verschillende overgangswaarschijnlijkheid van meson naar antimeson dan van antimeson naar meson, wat *CP* schending in mixen is. *CP* schending in verval vindt plaats zodra de vervalsamplitude van *CP*-geconjugeerde toestanden ongelijk zijn. Een derde vorm van *CP* schending wordt gevonden in de interferentie tussen de amplitudes van mixen en verval.

De LHC zal proton-proton botsingen verzorgen voor tests van het Standaard Model en voor zoektochten naar extra fysica bij een energie van 14 TeV in het massazwaartepunt en bij een ontwerpluminositeit van $10^{34}\mathrm{cm}^{-2}\mathrm{s}^{-1}$. LHCb specialiseert zich in zware-smaak fysica, waaronder de zoektocht naar nieuwe fysica in *CP* schending en naar zeldzame vervallen van *beauty* en *charm* hadronen. Het is de intentie van LHCb om gedetailleerde metingen te doen van $B^0_s - \overline{B}^0_s$ mixen, waarbij kanalen zoals $B^0_s \to D^-_s\pi^+$, $B^0_s \to J/\psi\phi$ en $B^0_s \to J/\psi\eta$ gebruikt zullen worden om de parameters ΔM_s, $\Delta\Gamma_s$ en ϕ_s precies te bepalen. LHCb richt zich er op om de kennis van de hoek γ te verbeteren, tegelijkertijd met het zoeken naar tekenen van nieuwe fysica. Een aanpak waarbij metingen van γ van enkel boomniveau *B* vervallen, zoals $B^0_s \to D^\mp_s K^\pm$, $B^0 \to D^0 K^{*0}$ en $B^\pm \to D^0 K^\pm$, gecombineerd worden met metingen van vervalskanalen die vierkant of pinguïn bijdragen hebben, zoals $B^0 \to \pi^+\pi^-$ en $B^0_s \to K^+K^-$, wordt aangenomen. Een verschil tussen deze metingen van γ kan veroorzaakt worden door nieuwe fysica, die dan aanwezig is in de vorm van virtuele deeltjes in kringdiagrammen. Vanuit dit perspectief zullen de $B_s^0 \to D_s^{\mp} K^{\pm}$, $B_s^0 \to J/\psi\phi$ en $B_{(s)}^0 \to h^+ h'^-$ vervallen worden geïnspecteerd.

De relevante vervalsproducten zijn hoofdzakelijk aanwezig in twee identieke kegels rond de bundelpijp, wat aanleiding geeft tot een spectrometerontwerp met één arm. LHCb heeft een silicium sporendetector of VELO om de primaire en secundaire vertices te vinden. Een geïntegreerd magneetveld van 4 Tm wordt gebruikt om geladen deeltjes af te buigen, wiens paden verder geregistreerd worden door de TT, IT en OT sporendetectoren. Dit maakt het mogelijk om het impuls en de lading van een deeltje te bepalen. Deeltjesidentificatie en energiebepaling worden verzorgd door twee RICH detectoren, door de elektromagnetische en de hadronische calorimeters en door het muonsysteem.

Zowel tijdens het ontwerp van de detector als in de ontwikkeling van de software voor het LHCb experiment, is Monte Carlo software gebruikt. Het biedt een voorbeschouwing van hoe echte data er uit kan zien en van de prestatie van de detector in verschillende scenarios. Dit maakt fijnafstelling van reconstructiesoftware mogelijk en geeft inzicht in het fysicapotentieel van LHCb.

Het pad van een geladen deeltje door de LHCb detetor wordt gereconstrueerd uit de signalen die het veroorzaakt in de positiegevoelige sporendetectoren. Het is de functie van de patroonherkenningsalgoritmes om te bepalen welke groepen van signalen bij individuele deeltjes horen. De logica van de patroonherkenning bepaalt eerst de stroomopwaartse en stroomneerwaartse beginpunten in de VELO en in de T stations. Deze zaden worden vervolgens gecomplementeerd met signalen uit de andere sporendetectoren. In het algemeen streeft de patroonherkenning er naar om sporen efficiënt te identificeren en daarbij zo weinig mogelijk combinaties van signalen te inspecteren. Hiervoor worden sneden gebruikt die geijkt zijn met behulp van Monte Carlo data.

Metingen worden gefit aan een spoormodel met behulp van een kleinste-kwadraten methode, geformuleerd als een Kalman filter. Het spoormodel is opgebouwd uit extrapolatievergelijkingen welke het magnetisch veld verdisconteren en waarop correcties voor meervoudige verstrooiing en energieverlies worden toegepast. De fit gebruikt geometrie-informatie om de positie van metingen en materiaallagen te identificeren. Trajectories vormen een abstractielaag tussen de beschrijving van de detectorgeometrie en de spoorreconstructiesoftware. Het elimineert de noodzaak om de reconstructievergelijkingen te herformuleren zodra de geometriebeschrijving verandert. Het Kalman filter is geformuleerd met een middelingsstap in plaats van met een gladstrijkstap, waardoor het efficiënter en numeriek stabieler is. De fitprocedure resulteert in optimale schattingen van de spoorparameters op discrete posities.

De spoorreconstructie produceert een uiteindelijke verzameling van 85.2±0.05 sporen. Hiervan zijn 25.4±0.05 Lange sporen, welke het belangrijkste type sporen voor fysica-analyses zijn. Lange sporen bevatten gemiddeld 36.0±0.05 metingen van de verschillende sporendetectoren. De breedte van residu *pull* distributies van deze metingen is gevoelig voor verschuivingen in de detector en bieden daardoor een indicatie van de detectoruitlijning. De efficiëntie waarmee metingen van Lange sporen gevonden worden is 91.9±0.05% na buitenliggerverwijdering, bij een puurheid van 99.3 ± 0.05%. Bij de gereconstrueerde vertex is de impulsresolutie van een Lang spoor 0.37±0.005% en de positieresolutie 39.0±0.05µm. De coördinaat en helling *pulls* zijn 10% te breed en de impuls *pull* is 25% te breed ter hoogte van de vertex, wat ruimte voor verbetering open laat. Deze kwestie wordt aangepakt door de schatting van de meetfouten te verbeteren en door de in Geant4 gebruikte instellingen voor de inachtneming van materiaaleffecten te bestuderen.

Gereconstrueerde sporen leveren informatie over positie, richting, impuls en lading als invoer voor fysica-analyses. De nauwkeurigheid van de geschatte hellingen en impulsen ter hoogte van de vervalsvertex beïnvloed de massaresolutie van het moederdeeltje. In het geval van $B_s^0 \to D_s^- \pi^+$ vervallen wordt de B_s^0 massaresolutie van 17.45±0.27 MeV gedomineerd door de impulsresolutie, terwijl de massaresolutie van 6.25±0.09 MeV van het D_s^- gedomineerd wordt door de resolutie van de hellingen. Het verkeerd identificeren van een pion als een kaon in een $B_s^0 \to D_s^- \pi^+$ verval resulteert in achtergrond voor een $B_s^0 \to D_s^\mp K^\pm$ analyse. De spoorreconstructie biedt een 2σ massaverschil tussen de respectievelijke B_s^0 massapieken ten behoeve van verwerping van deze achtergrond.

De eigentijdresolutie van het B_s^0 deeltje in $B_s^0 \to D_s^- \pi^+$ vervallen is 42.1±0.6 fs. Een kleine eigentijdresolutie is belangrijk voor metingen van de tijdsafhankelijke *CP* asymmetrie in het B_s^0 systeem. Het verwatert de asymmetrie meting met een factor van 0.78±0.06 voor $B_s^0 \to D_s^- \pi^+$ vervallen. Het fitten van de vervalstijd maakt het mogelijk om de waarde van ΔM_s met een fout van 0.008 ps te bepalen, en de waarde van $\omega_{\rm tag}$ tot binnen 0.03 te identificeren.

Acknowledgements

This quest to become a PhD in high-energy particle physics began when prof.dr. van den Brand accepted me as a member of his bfys group at Nikhef. Marcel Merk became my promotor and as such has provided me with invaluable insights and support. As my copromotor, Gerhard Raven has proven to be a treasure trove of information and eager to share it with everyone. My daily supervisor Eduardo Rodrigues has been immensely helpful regarding all aspects of research, as well as being an awesome person. Many more people at Nikhef and at CERN have contributed to the successful completion of my PhD work. I thank you all for what you have done for me.

My best friends Gideon Koekoek, Zdenko van Kesteren, and Lukas Baars are responsible for great times, filled with everything from deep conversations to hilarious nonsense. They offer such a broad perspective on the world and manage to make a joke of it all, which I think is quite a feat. Throughout the years, the Nikhef and CERN crews have kept up an endless stream of parties, outings, and beer to fill them with good days. I am very grateful for this and can only wish for much more of the same.

Zoals altijd hebben mijn ouders Dolf en Joke en broer Marco mij gesteund en een luisterend oor geboden, zelfs al die keren dat ik het over onbegrijpelijke zaken had. Bedankt daarvoor!